Robust control of an induction machine

van Uden, Robert

Award date:
1995

EINDHOVEN UNIVERSITY OF TECHNOLOGY
DEPARTMENT OF ELECTRICAL ENGINEERING
Measurement and Control Section

ROBUST CONTROL OF AN INDUCTION MACHINE

Robert van Uden

M. Sc. Thesis
carried out from January 1995 to August 1995
commissioned by Prof. Dr. Ir. P.P.J. van den Bosch
under supervision of Ir. R.J. Gorter
date August 14, 1995.

Abstract

The influence of an error between the parameters in an indirect field oriented controller and an induction machine on the static and dynamic behaviour have been analyzed by means of simulations. A nonlinear model is derived which describes both the steady state behaviour and dynamical behaviour when there exists a parameter mismatch between the parameters in the indirect field oriented controller and the induction machine. This error model is used to design a robust controller which makes use of H_∞ theory. The controller is developed in such a fashion that the closed loop remains stable and reduces the influence of the load torque on the angular velocity of the rotor axis, despite the presence of plant perturbations. The main objective of the design procedure is to attenuate the influence of the load torque on the angular velocity of the rotor axis. A fast tracking system was not a major design objective. Simulations have been carried out.

Another topic that has been studied is the control of the current in the stator windings by using a voltage converter. A method is outlined which makes it possible to control the current in the stator windings of an induction machine by manipulating the stator voltage. A robust controller is designed which guarantees robust stability and robust performance.

Contents

Chapter 1

Problem statement

1.1 The induction machine

An induction machine or asynchronous machine converts electrical energy to mechanical energy. The electrical energy can be supplied by a converter and enters the induction machine in the stator windings. The electrical power can be expressed by means of the inner product of the electrical current and voltage. The mechanical power can be expressed by means of the inner product of the electromagnetic torque and the angular velocity of the rotor axis. The conversion from electrical power to mechanical power takes place via the mutual flux of the stator windings and rotor windings. An electromagnetic torque T_e can only be produced when the angular velocity ω_m of the rotor axis differs from the angular velocity ω_0 of the stator field. This difference in angular velocity, called $\omega_{slip} = \omega_0 - \omega_m$ induces a voltage in the rotor windings with a corresponding current. The vector product of the rotor current and the rotating field produces an electromagnetic torque.

The induction machine can be considered as a white box IM which has been depicted in figure 1.1. The orthogonal stator current components $I_{\alpha s}$ and $I_{\beta s}$ produce a magnetizing current I_m and an electromagnetic torque T_e. The electromagnetic torque causes an acceleration or deceleration of the rotor axis when T_e is greater or smaller than the load torque T_l. The variables J and D denote respectively the inertia and damping coefficient.

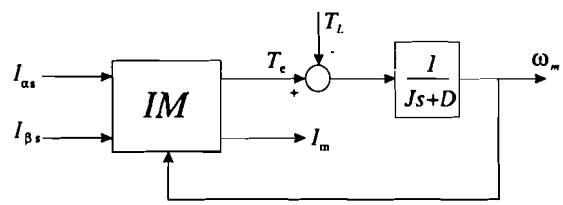

Figure 1.1: Block diagram of an induction machine

The physical laws that constitute the behaviour of the induction motor will be derived in chapter 2.

1.2 The indirect field oriented controller

The objective of the indirect field oriented controller (indirect FOC) is to control the electromagnetic torque T_e and the magnetizing current I_m of the induction motor. The physical laws that describe the behaviour of the induction machine can also be used to control the induction machine. These physical laws can be used to construct a so called indirect field oriented controller that utilizes a feed forward scheme to control the induction machine. This technique is based on a coordinate transformation from stator coordinates to field coordinates. The stator coordinate system is a reference frame that is attached to the world. The field coordinate frame is a frame that coincides with the rotor flux vector. A linear expression for the the electromagnetic torque can be obtained when the magnetizing current is kept at a constant value. It is therefore desirable to control the magnetizing current. The theoretic background of this controller will be given in chapter 2.

The indirect flux oriented controller can also be looked upon as a white box that has been depicted in figure 1.2. T_{e*} is the desired electromagnetic torque in the induction motor. I_{m*} is the desired magnetizing current in the induction motor. Also the angular velocity of the rotor axis is needed to compute the corresponding stator current components $I_{\alpha s}$ and $I_{\beta s}$. The main

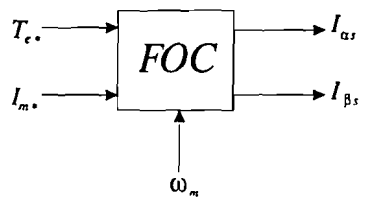

Figure 1.2: Block diagram of an indirect field oriented controller.

advantage of indirect field oriented control lies in the fact that the controller only requires the rotor speed which can be measured by means of a tacho generator. As opposed to direct field oriented control which requires the value of the flux which can either be obtained by means of Hall sensors in the stator or observers that calculate the flux values from stator measurements.

1.3 The control scheme

The physical properties of the induction motor can be described by means of a set of nonlinear differential equations which can be characterized by four parameters i.e. the rotor resistance, magnetizing inductance, stator resistance and the leakage inductance. It is known that especially the rotor resistance and the magnetizing inductance deviate from their nominal values due to temperature influences and magnetic saturation. This deviation confuses the applicability of an indirect field oriented controller. The indirect FOC inhabits the inverse model of an IM. This means that a concatenation of the indirect FOC, characterized by parameter set Θ^* and an IM, characterized by parameter set Θ yields a linear transfer function if the parameters of the indirect FOC are estimated correctly. Thus when the parameters in Θ^* equals the parameters in Θ. This scheme is depicted in figure 1.3. The contents of both block FOC and IM can be described by nonlinear differential equations. Concatination of both blocks results in a linear transfer function that is depicted in figure 1.4. It will be possible to control the electromagnetic torque immediately by adjusting the desired torque at the T_{e*} port. The magnetizing current can

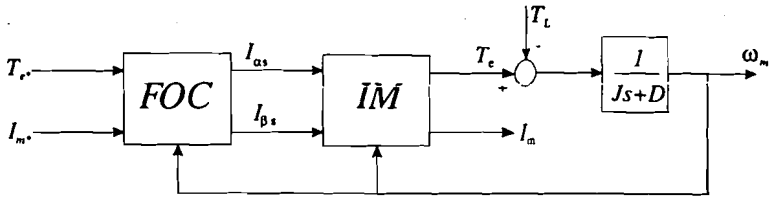

Figure 1.3: IM represents the induction machine and FOC represents the indirect field oriented controller.

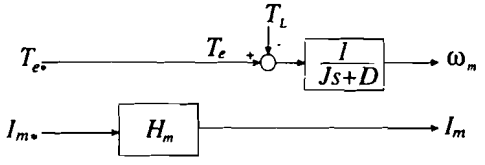

Figure 1.4: Ideal transfer function after concatenation of the induction machine and the indirect field oriented controller if $\Theta^* = \Theta$.

be adjusted by means of reference input I_{m*}. The desired value will not be reached immediately, due to the fact that the reference I_{m*} is linked with the ideal I_m via a first order network H_m. This model will be derived in chapter 3.

However, this representation of the controlled induction motor requires some very strict conditions. The first conditions is correct knowledge of the motor parameters. This condition can in practice never be met due to the fact that these parameters deviate from their nominal values caused by temperature influences and magnetic saturation. The second condition is the absence of converter delay. The converter is supposed to react instantaneously on its reference input. It is not possible in practice to eliminate the influence from the converter delay. An approach will be outlined in chapter 5 which gives us the possibility to incorporate a voltage converter in the control scheme. The reference port of a voltage converter is manipulated in such a fashion that the current in the stator windings tracks its reference value.

Lets consider the behaviour of the induction machine when the parameter set (Θ^*) in the indirect FOC does not equal the parameter set Θ in the induction machine, which will always be the case in practice. The simplified transfer function from figure 1.4 will not be obtained but this transfer function will be corrupted with nonlinear transfer functions. These nonlinear transfer functions can also be represented as uncertainties from a linear model. This leads to the block diagram of figure 1.5. The study will result in a transfer function of the robust controller K. Our first aim will be to describe the structure and bounds of block Δ. Secondly, we will develop a controller that stabilizes the induction machine for every possible perturbation. Thirdly, the controller K will have to be developed in such a fashion that conditions will be met such as good tracking properties and prevention of converter overflow, in the face of perturbations, defined in Δ.

The control scheme can also be reconstructed to the general block scheme that has been depicted in figure 1.6. The block diagram contains three blocks. Block $P(s)$ represents the ideal linear process when no parameter perturbations exist. These perturbations will be modelled in block Δ. The third block is the controller K that has to be developped. The control input u

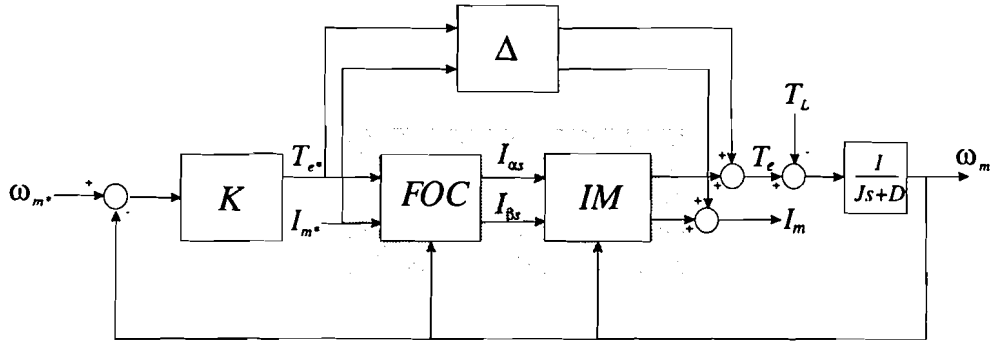

Figure 1.5: Control scheme of the concatenated indirect field oriented controller and the induction motor.

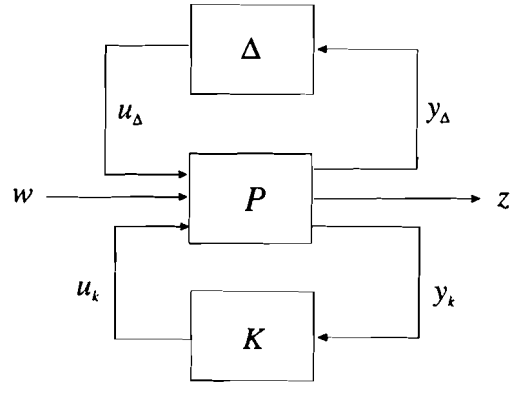

Figure 1.6: General control scheme.

of P is the output of the controller and drives the input of the indirect field oriented controller-induction motor combination. The exogenous input vector w contains the setpoint values of the induction motor which is the rotor speed, set by ω_{m*}. The output vector y_k contains the measured values from the induction motor that are fed back to the controller K. Vector z contains the variables we wish to regulate such as the error signal from the reference input value ω_{m*} and the actual rotor speed ω_m and the stator voltage U_s. Chapter 4 will elaborate on the contents of the three blocks in figure 1.6.

Chapter 2

Field oriented control

The physical laws that describe the behaviour of the induction will be derived in this chapter. First, we will derive a model that can only be used to analyse the behaviour of the induction motor with a locked rotor. After that we will extend the obtained model with a so called Ideal Rotating Transformer (IRTF) that enables us to describe the relationship between the stator circuit and the rotor circuit. Transformations between the various coordinate systems such as stator, rotor and field coordinate system will be explained. The physical laws expressed in field coordinates will eventually lead to the indirect field oriented controller. Concatenation of both the indirect FOC and the IM will result in a linear relation between the inputs of the indirect FOC and the outputs of the motor, provided that the parameters of the IM have been identified correctly. We will not go into the situation of incorrect identified motor parameters in this chapter. This will be done in chapter 3.

2.1 The multi phase induction machine

An induction machine can be described by means of the electromagnetic laws that describe the interaction of rotor and stator variables. These electromagnetic laws can be combined in such a fashion that a model is obtained that describes the behaviour of the induction motor by means of a two phase electrical model [13]. This is represented in figure 2.1. Two reference frames can be distinguished in figure 2.1: a stator frame and a rotor frame. The rotor frame is rotated relative to the stator frame by angle θ_m. The induction motor is supplied by two voltage sources $U_{s\alpha}$ and $U_{s\beta}$ that constitute together a rotating space vector $U_s^S = U_{s\alpha} + jU_{s\beta}$. All voltages and currents are complex variables. Superscript $()^S$ and subscript (α, β) indicate that the space vector is described in stator coordinates. A quantity can also be expressed in rotor coordinates which will be indicated by means of superscript $()^R$ and the subscripts (a, b).

2.1.1 The locked rotor model

Energy transfer takes place by means of the flux in the air gap between the stator and the rotor. The stator flux is produced by the stator current and contains two components: $\Psi_s = \Psi_m + \Psi_{\sigma s}$. Flux component $\Psi_{\sigma s}$ is the leakage flux which is not linked with the rotor. The part of the stator flux that does reach the rotor is denoted by Ψ_m. The same can be said about the rotor flux which can be expressed as $\Psi_r = \Psi_m - \Psi_{\sigma r}$ where $\Psi_{\sigma r}$ represents the rotor flux that is not linked

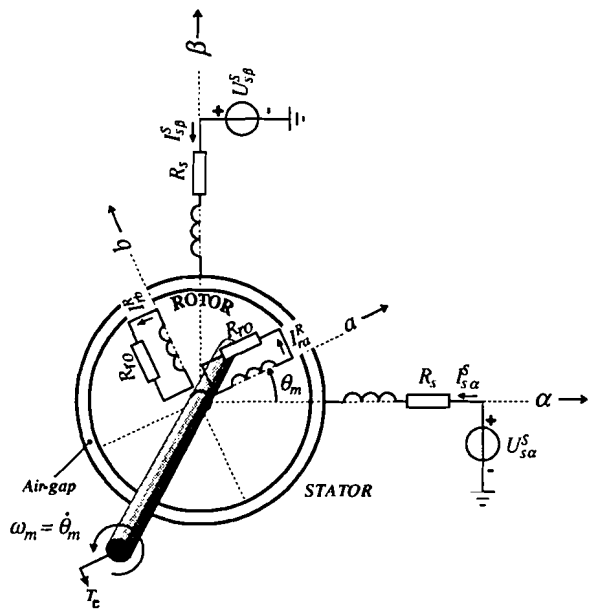

Figure 2.1: General orthogonal 2 phase equivalent machine representation.

with the stator. The stator flux and the rotor flux can be expressed as

$$\Psi_s = \Psi_m + \Psi_{\sigma s} = L_{mag} I_m + L_{\sigma s} I_s \tag{2.1}$$

$$\Psi_r = \Psi_m + \Psi_{\sigma r} = L_{mag} I_m - L_{\sigma r} I_r \tag{2.2}$$

The total stator current is defined as $I_s = I_m + I_r$. This leads together with the equations 2.1 and 2.2 to the phase locked rotor model that is depicted in figure 2.2.

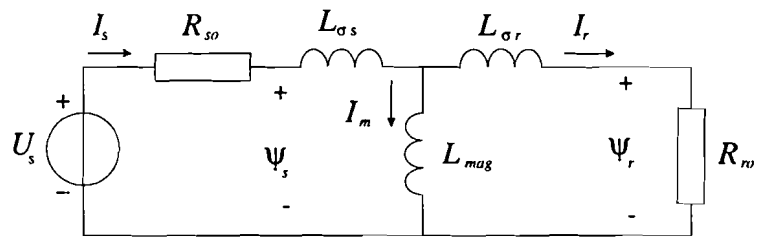

Figure 2.2: phase locked rotor model.

Inductance $L_{\sigma s}$ and $L_{\sigma r}$ represent the leakage inductance and L_{mag} represents the mutual inductance. The rotor resistance R_{ro} represents the active losses in the rotor circuit and stator resistance R_{so} represents the active losses in the stator windings.

It is possible to simplify the model depicted in figure 2.2 by applying Thevenin's theorem [13]. A resulting leakage inductance L_σ can be computed that replaces both the stator leakage inductance and the rotor leakage inductance. The parameter transformations are conducted by means of the following formulas

$$k_1 = \frac{L_{mag}}{L_{mag} + L_{\sigma r}} \tag{2.3}$$

$$L_\sigma = L_{\sigma s} + \frac{L_{mag} L_{\sigma r}}{L_{mag} + L_{\sigma r}} \tag{2.4}$$

$$L_m = k_1^2 (L_{mag} + L_{\sigma r}) \tag{2.5}$$

$$R_r = k_1^2 R_{r0} \tag{2.6}$$

$$R_s = R_{s0} \tag{2.7}$$

The model presented in figure 2.2 can than be obtained. This model is only valid for a locked

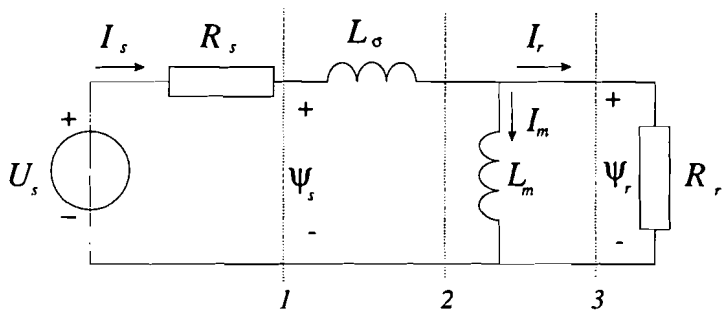

Figure 2.3: Simplified locked rotor model.

rotor situation. Therefore the model can not applied to analyse transients. A model is needed that incorporates a stator section, a rotor section and a mechanical section. This is done in the Ideal Rotating Transformer (*IRTF*).

2.1.2 The dynamic induction motor model

The *IRTF* provides us with the opportunity to represent a quantity in stator coordinates or rotor coordinates [6]. The angle between the coordinate systems is the mechanical axis angle θ_m. The *IRTF* has graphically been depicted in figure 2.4. If I^S is input then Ψ^R must be input

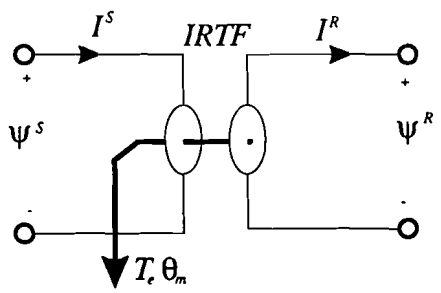

Figure 2.4: IRTF

on the rotor side to maintain computational causality. The flux vector and the current vector on stator and rotor side are related by the following expressions

$$I^S = I^R e^{j\theta_m} \tag{2.8}$$

$$\Psi^R = \Psi^S e^{-j\theta_m} \tag{2.9}$$

It should be noted that the magnitude of the current and flux does not change, there is only a rotation performed over angle θ_m. This rotation can also be expressed as follows

$$I^S = A_{rot}(\theta_m)I^R \tag{2.10}$$

$$\Psi^R = A_{rot}(-\theta_m)\Psi^S \tag{2.11}$$

Expanding equation 2.10 yields

$$I_r^S = \begin{pmatrix} I_{r\alpha} \\ I_{r\beta} \end{pmatrix} = \begin{bmatrix} \cos\theta_m & \sin\theta_m \\ -\sin\theta_m & \cos\theta_m \end{bmatrix} \begin{pmatrix} I_{ra} \\ I_{rb} \end{pmatrix} \tag{2.12}$$

The amplitude of both flux Ψ^S and Ψ^R remains constant on the stator and rotor side. The current on the rotor side and stator side have the same amplitude. Also the phase angle between current and flux remains constant on the stator side and the rotor side. This can be explained by the *IRTF* property that no energy loss nor energy storage occurs in the *IRTF*. This also means that the *IRTF* can be inserted in three different locations in figure 2.3. Insertion of the *IRTF* at position 2 yields the following model.

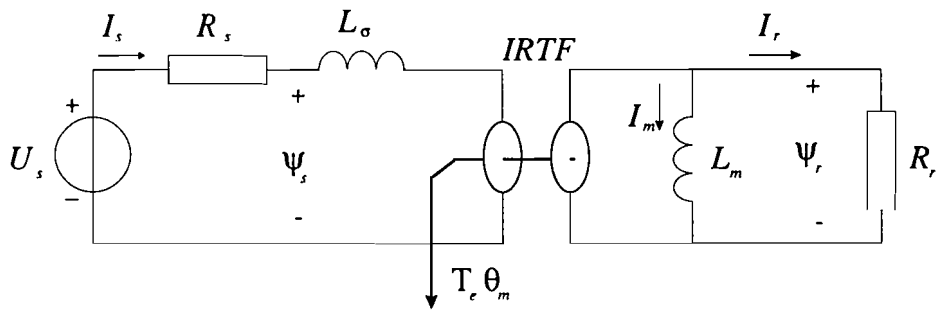

Figure 2.5: Dynamical induction machine model.

This model can be translated in a simulation model [13] that enables us to simulate the dynamic behaviour of the induction motor. This model will be used for the simulations that will be carried out later on in this report.

The relation between the stator voltage on the stator side and rotor side has not been mentioned sofar. The voltage can be computed by expanding

$$U^R = \frac{d\Psi^R}{dt} \tag{2.13}$$

Substitution of equation 2.9 yields the following expression for the relation between the voltage in stator coordinates and rotor coordinates

$$U^R = \frac{d}{dt}(\Psi^S e^{-j\theta_m}) \tag{2.14}$$

$$= U^S e^{-j\theta_m} - j\Psi^S \frac{d\theta_m}{dt} e^{-j\theta_m} \tag{2.15}$$

We can expand equation 2.15 when we assume that the rotor axis rotates with a constant angular velocity ω_m. This also means that the voltage at the stator side is periodic with frequency ω_0 and has a constant amplitude $\hat{U}_s^S$

$$U_s^S = \hat{U}_s e^{j\omega_0 t} \tag{2.16}$$

Substitution of equation 2.16 in equation 2.15 yields

$$\begin{aligned} U^R &= \frac{\omega_0 - \omega_m}{\omega_0} U^S e^{-j\omega_m t} \\ &= \frac{\omega_0 - \omega_m}{\omega_0} \hat{U}_s e^{j(\omega_0 - \omega_m)t} \\ &= \frac{\omega_{slip}}{\omega_0} \hat{U}_s e^{j\omega_{slip} t} \end{aligned} \tag{2.17}$$

It can be seen that the amplitude of the voltage on the rotor side depends on the rotor speed. Also the angular velocity of the rotor voltage depends on the rotor velocity. We can also use this result to derive an alternative model of the stator circuit in the induction machine by transforming the rotor voltage to the stator circuit. Thus

$$\begin{aligned} U_r^S &= \frac{\omega_0}{\omega_0 - \omega_m} U_r^R e^{j\omega_m t} \\ &= \frac{\omega_0}{\omega_0 - \omega_m} I_r^R R_r e^{j\omega_m t} \\ &= \frac{R_r}{slip} I_r^S \end{aligned} \tag{2.18}$$

and *slip* is defined as $slip = \frac{\omega_0 - \omega_m}{\omega_0}$. The alternative model has been depicted in figure 2.6

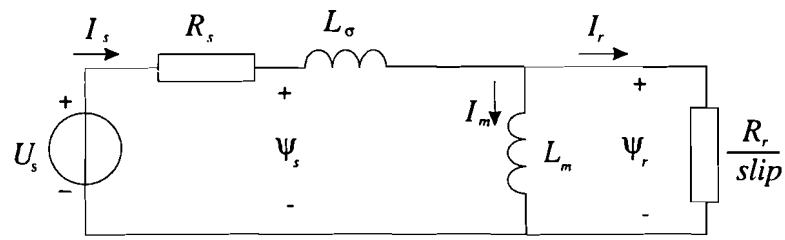

Figure 2.6: Alternative dynamical induction machine model.

2.1.3 Computation of the electric torque

The torque is a function of the current, the flux and the angle between these two quantities and is

$$T_e = -I^S \times \Psi^S = -I^R \times \Psi^R \tag{2.19}$$

or equivalently

$$T_e = -\mathrm{Im}[\bar{I}^S \Psi^S] = -\mathrm{Im}[\bar{I}^R \Psi^R] \tag{2.20}$$

$$T_e = -\Psi_{s\alpha} I_{s\beta} + \Psi_{s\beta} I_{s\alpha} = -\Psi_{ra} I_{rb} + \Psi_{rb} I_{ra} \tag{2.21}$$

The transition from equation 2.19 to equation 2.20 in steady state has been proved in [6]. The stator current in the rotor section can in the steady state (constant ω_m) be represented by

$$I_s^R = \hat{I} e^{j(\omega_{slip} t + \xi_0)} \tag{2.22}$$

This results in a rotor voltage

$$U_r^R = \frac{j\omega_{slip} L_m R_r}{R_r + j\omega_{slip} L_m} \hat{I} e^{j(\omega_{slip} t + \xi_0)} \tag{2.23}$$

The flux can be obtained by integration of the voltage U_r^R

$$\Psi_r^R = \int_0^t U_r^R d\tau = \frac{L_m R_r}{R_r + j\omega_{slip} L_m} \hat{I} e^{j(\omega_{slip} t + \xi_0)} \tag{2.24}$$

Substitution of the obtained expressions for Ψ_r^R and I_r^R in $T_e = -\mathrm{Im}[\overline{I}_r^R \Psi_r^R]$ yields

$$T_e = -\mathrm{Im}\left[\frac{\hat{I}^2 R_r L_m}{R_r + j\omega_{slip} L_m}\right] \tag{2.25}$$

$$= \frac{\hat{I}^2 R_r L_m^2 \omega_{slip}}{R_r^2 + \omega_{slip}^2 L_m^2} \tag{2.26}$$

$$= \frac{\hat{I}^2}{R_r} \frac{\omega_{slip} L_m^2}{1 + \omega_{slip}^2 \left(\frac{L_m}{R_r}\right)^2} \tag{2.27}$$

The electromagnetic torque with fixed current amplitude has been plotted as a function of the slip frequency. This has been done in figure 2.7. Equating derivative $\frac{dT_e}{d\omega_{slip}}$ of equation 2.27 to

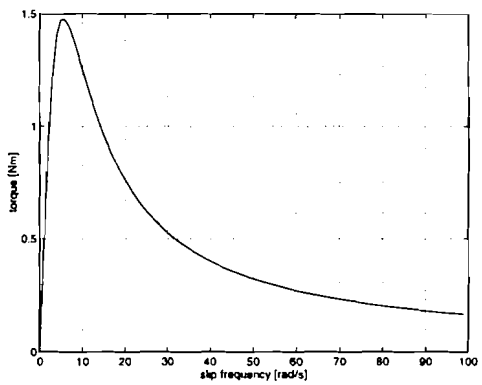

Figure 2.7: Torque slip frequency characteristic.

zero yields the maximum torque value $T_{e_{max}}$

$$T_{e_{max}} = \frac{\hat{I}^2 L_m}{2} \tag{2.28}$$

and the corresponding $\omega_{slip_{max}}$.

$$\omega_{slip_{max}} = \frac{R_r}{L_m} \tag{2.29}$$

The induction machine has a stable working point if $\omega_{slip} < \omega_{slip_{max}}$.

2.2 Field coordinates

2.2.1 Representation of the currents in an phasor diagram

A phasor diagram gives us insight in the behaviour of the currents in an induction machine. The stator and rotor frames become apparent. The angular relationship between the stator current

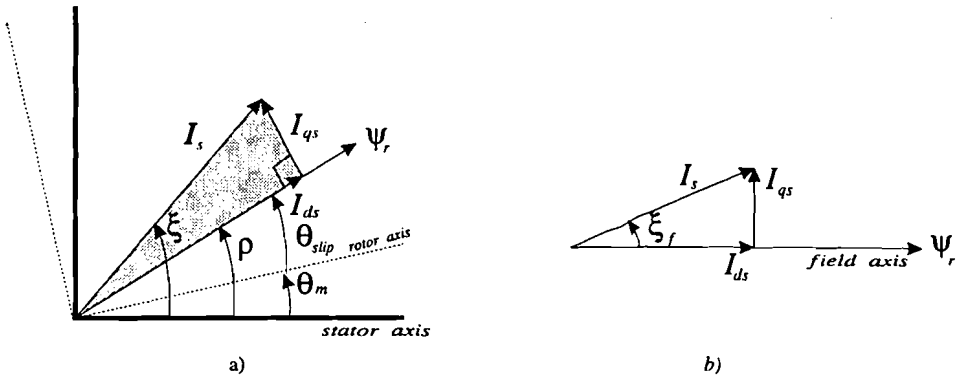

Figure 2.8: Phasor diagram of the stator current in stator coordinates a) and field coordinates b)

vector, flux vector and rotor axis has been depicted in figure 2.8a for an induction machine which rotor axis rotates with an angular velocity ω_m. The stator currents are impressed in the induction motor in the stator windings and can be expressed as

$$I_{s\alpha} = \mathrm{Re}\,[I_s^S] \tag{2.30}$$
$$I_{s\beta} = \mathrm{Im}\,[I_s^S] \tag{2.31}$$

The field coordinate system rotates synchronously with the rotor flux. Thus it is possible to express the stator current with respect to field coordinate frame. The stator current vector in field coordinates is shown to consist of two orthogonal components and can be obtained by rotating I_s by angle $-\rho$. These components have been depicted in figure 2.8b and are defined as

$$I_{ds} = \mathrm{Re}\,[I_s^S e^{-j\rho}] \tag{2.32}$$
$$I_{qs} = \mathrm{Im}\,[I_s^S e^{-j\rho}] \tag{2.33}$$

The field coordinate system rotates synchronously with the rotor flux vector. It can be seen in figure 2.8 that I_{ds} is pointed in the direction of the magnetizing current and the other component I_{qs} perpendicular to it. In steady state condition I_{ds} and I_{qs} are constant apart from converter induced ripple. The stator current I_s^S and the magnetizing current $I_m^S = \frac{\Psi_r^S}{L_m}$ rotate with angular velocity $\omega_0 = \frac{d\xi}{dt}$ and $\omega_f = \frac{d\rho}{dt}$ respectively with respect to the stator frame. The stator current and magnetizing current can be expressed as $I_s^S = I_s e^{j\xi}$ and $I_m^S = I_m e^{j\rho}$. In which I_m, ρ, I_s and ξ are all scalar functions which are a function of time. The two current vectors I_s^S and I_m^S rotate synchronously under steady state conditions. This means that $\omega_0 = \omega_f$ in steady state. An elaboration on this will be made in section 2.2.2.

2.2.2 Coordinate transformations

In flux oriented control all vectors are described in field coordinates. This coordinate system is chosen in such a fashion that the rotor flux coincides with the real axis of the field coordinate frame. According to the *IRTF* model in figure 2.5 the following expression holds in each coordinate system:

$$I_m = I_s - I_r \tag{2.34}$$

The magnetizing current, stator current and the rotor current can be subdivided in a real and an imaginary part

$$I_m^F = I_{dm} + jI_{qm} \tag{2.35}$$
$$I_s^F = I_{ds} + jI_{qs} \tag{2.36}$$
$$I_r^F = I_{dr} + jI_{qr} \tag{2.37}$$

The imaginary part of I_m^F equals zero by definition ($I_{qm} = 0$) due to the fact that magnetizing current vector I_m rotates synchronously with the flux vector. Substitution of equation 2.35, 2.36 and 2.37 in equation 2.34 and equating the real and the imaginary part yields

$$I_{qr} = I_{qs} \tag{2.38}$$
$$I_{dr} = I_{ds} - I_{dm} \tag{2.39}$$

Equation 2.39 can be simplified by substitution of $I_{dr} = 0$ in the steady state. This can be proved by transforming the rotor current to the field coordinate frame ($I_r^R = \frac{1}{R_r} j\omega_0 \Psi_r^R$). Rearranging the complex description of the stator, rotor and magnetizing current results in the following formulas

$$I_m^F = I_{dm} = I_{ds} \tag{2.40}$$
$$I_s^F = I_{ds} + jI_{qs} \tag{2.41}$$
$$I_r^F = jI_{qr} = jI_{qs} \tag{2.42}$$

It follows from equation 2.42 that the rotor current rotates perpendicular to the flux vector in steady state. These vectors have been depicted in figure 2.9a and b. A transformation of flux and

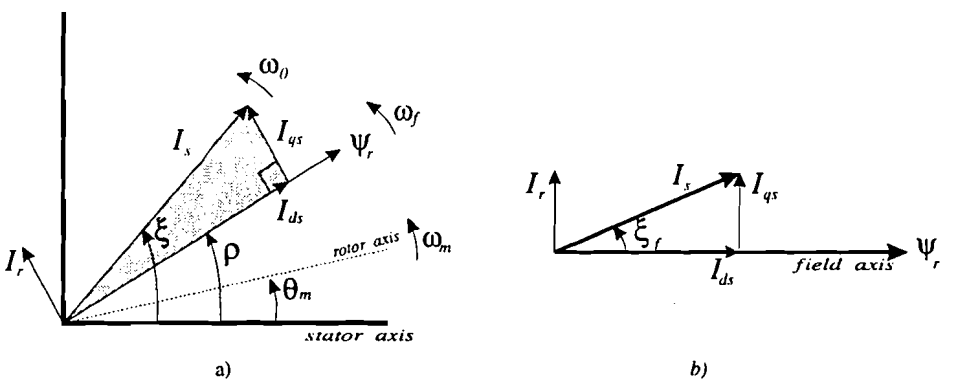

Figure 2.9: Phasor diagram in steady state.

current in stator coordinates to the field coordinates system can be established by multiplying an expression in stator coordinates with $e^{-j\rho}$. Likewise, a transformation from rotor to stator coordinates can be performed by multiplying a vector with $e^{j\theta_m}$. The various transformations have been depicted in figure 2.10. For example, the stator current can be transformed to field coordinates in the following fashion

$$I_s^R = I_s e^{j(\xi - \theta_m)} \tag{2.43}$$
$$I_s^S = I_s^R e^{-j\theta_m} = I_s e^{j\xi} \tag{2.44}$$
$$I_s^F = I_s^S e^{-j\rho} = I_s e^{j(\xi - \rho)} \tag{2.45}$$

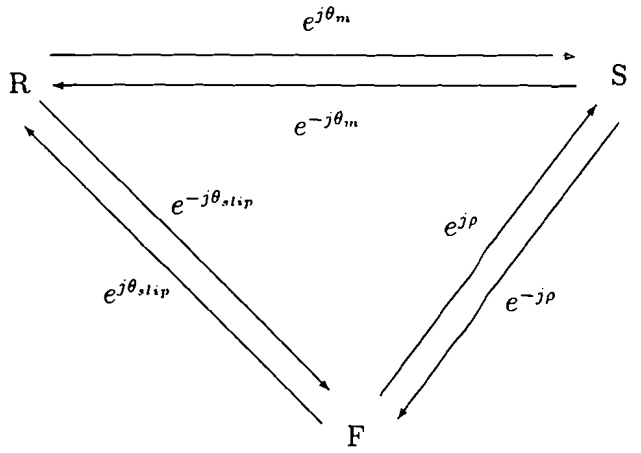

Figure 2.10: Transformation diagram between S, R and F coordinates.

The latter transformation results in a phase angle that is described by $\xi - \rho$. The magnitude from the rotor current does not change by transforming a vector from one coordinate frame to the other. Only the phase angle changes when a transformation from one system to the other is performed. The stator current angle ξ is impressed by the current converter and the angle ρ between the field coordinate system and the stator coordinate system is defined as follows

$$\rho(t) = \int_0^t \omega_f(\tau)d\tau + \rho_0 \tag{2.46}$$

and depends on the electrical transients. The machine rotates in the steady state with a constant mechanical speed and the angular velocity of the field vector equals the angular velocity of the stator current, therefore $\omega_f = \omega_0$.

2.3 Control of an IM in field coordinates

2.3.1 Transformation from stator coordinates to field coordinates

Application of Kirchoffs voltage law on the induction machine model from figure 2.5 yields the following expression

$$R_r I_r^R - L_m \frac{dI_m^R}{dt} = 0 \tag{2.47}$$

In order to obtain the complete model of the induction motor in field coordinates, I_m^R is now inserted into the rotor voltage equation.

$$R_r(I_s^R - I_m^R) - L_m \frac{dI_m^R}{dt} = 0$$

Substitution of $I_s^R = I_s^S e^{-j\theta_m}$ and $I_m^R = I_m^S e^{-j\theta_m}$ yields an expression in stator coordinates.

$$\tau_r \frac{dI_m^S}{dt} + I_m^S(1 - j\omega_m\tau_r) = I_s^S \tag{2.48}$$

with rotor time constant $\tau_r = \frac{L_m}{R_r}$. The next step involves a transformation from stator coordinates to field coordinates. This means that the magnetizing component is expressed with respect to the rotating flux vector Ψ_r^S. Substitution of $I_s^S = I_s^F e^{j\rho}$ and expanding the left hand expression results in

$$\begin{aligned} \tau_r \frac{dI_m^F}{dt} + j\tau_r\omega_f I_m^F + I_m^F(1 - j\omega_m\tau_r) &= I_s^S e^{-j\rho} \\ \tau_r \frac{dI_m^F}{dt} + j\tau_r\omega_{slip} I_m^F + I_m^F &= I_s^F \end{aligned} \tag{2.49}$$

In which $()^F$ indicates that the vectors are expressed in field coordinates. This equation may be split in a real and imaginary part by defining $I_m^F = I_m$ and $I_s^F = I_{ds} + jI_{qs}$,

$$\tau_r \frac{dI_m}{dt} + I_m = I_{ds} \tag{2.50}$$

$$\frac{d\rho}{dt} = \omega_m + \frac{I_{qs}}{\tau_r I_m} = \omega_m + \omega_{slip} \tag{2.51}$$

The torque equation (eqn. 2.19) also holds in field coordinates.

$$T_e = -I^S \times \Psi^S = -\mathrm{Im}[\overline{I}^S \Psi^S] = -\mathrm{Im}[\overline{I}^R \Psi^R] \tag{2.52}$$

Substitution yields

$$T_e = -\mathrm{Im}[\overline{I}_s^S \Psi_r^S] \tag{2.53}$$

$$= L_m \mathrm{Im}[I_s^S \overline{I}_m^S] \tag{2.54}$$

In which the overline indicates that a complex conjugation operation has to be performed. The magnetizing current in stator coordinates can be expressed as

$$I_m^S = I_m e^{j\rho} \tag{2.55}$$

By substitution it follows

$$T_e = L_m \mathrm{Im}[I_s^S I_m e^{-j\rho}] \tag{2.56}$$

$$= L_m I_m I_{qs} \tag{2.57}$$

This simple expression gives us a clue why the transformation from stator coordinates to field coordinates is the key to control of induction machines. The torque is proportional to the quadrature current component I_{qs} and the magnetizing current I_m. The electromagnetic torque can directly be manipulated by maintaining the magnetizing current on a constant level and vary I_{qs}. It is not possible to control the torque instantaneous when I_{qs} is kept constant and I_{ds} will be varied, because I_m tracks I_{ds} via a first order network described by equation 2.50.

The mechanical section can be represented by the following differential equation

$$J\frac{d\omega_m}{dt} + D\omega_m = T_e - T_l \tag{2.58}$$

in which variables J and D represent respectively the inertia and the damping and input T_l denotes the load torque.

We can conclude by stating that the induction motor can be modelled in field coordinates by means of the following equations.

$$I_s^F = I_{ds} + jI_{qs} = I_s^S e^{-j\rho} \tag{2.59}$$

$$\tau_r \frac{dI_m}{dt} + I_m = I_{ds} \tag{2.60}$$

$$\frac{d\rho}{dt} = \omega_m + \frac{I_{qs}}{\tau_r I_m} = \omega_m + \omega_{slip} \tag{2.61}$$

$$J\frac{d\omega_m}{dt} + D\omega_m = T_e - T_l \tag{2.62}$$

$$T_e = L_m I_m I_{qs} \tag{2.63}$$

These five linear and nonlinear equations can be used to construct the induction machine model that is depicted in figure 2.11 in which H_m is defined as

$$H_m = \frac{1}{\tau_r s + 1} \tag{2.64}$$

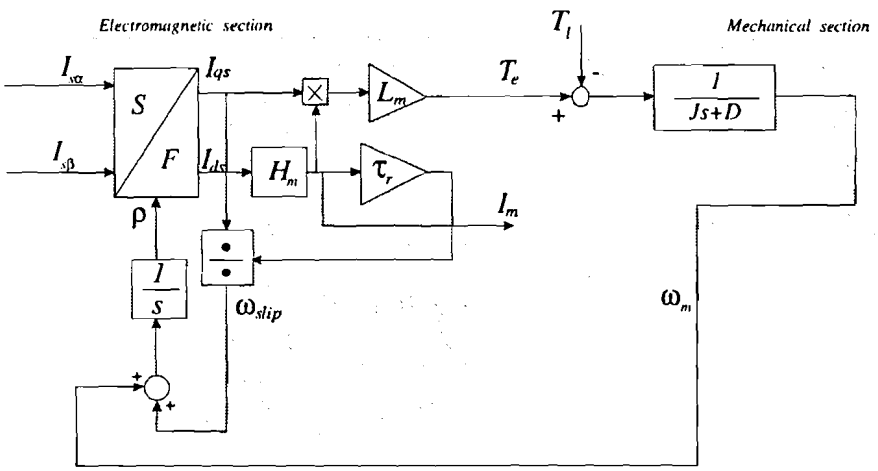

Figure 2.11: Model of the induction motor in field coordinates.

2.4 Field oriented control

Having derived the equations that can be used to model the induction motor it is now time to focus on block *FOC* in the general block scheme in figure 1.2 on page 5. Block *FOC* can be constructed by several methods. Field Oriented Control is one of the methods that can be applied. It uses equations 2.60, 2.61, 2.62 and 2.63 that have been derived in section 2.3. Two methods can be distinguished:

- Direct field oriented control
- Indirect field oriented control

Both methods will be explained in the next two subsection

2.4.1 Direct field oriented control

This block contains, as can be seen in figure 2.12, a torque controller and a flux controller, which are PI-controllers. This choice has been made in order to make the steady state error between the desired inputs (T_{e*} and I_{m*}) and outputs (T_e and I_m) zero. A D-action has been ommitted due to the fact that the noise component would have a considerable influence on the controller behaviour. The output of these controllers produce respectively I_{qs} and I_{ds}, which are inputted in the field to stator coordinate transformation block F/S.

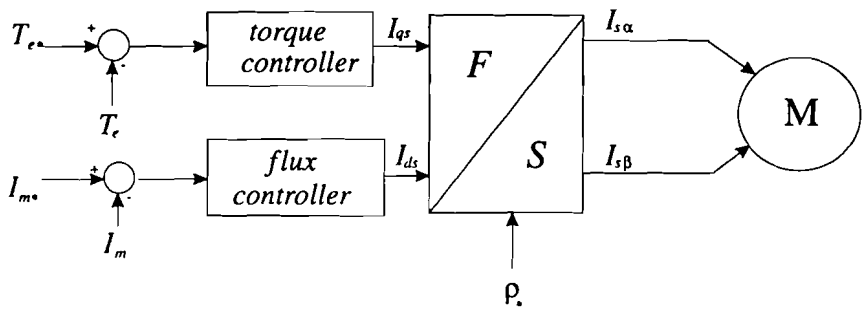

Figure 2.12: Direct field oriented control scheme

This control technique is based on the knowledge of the flux vector i.e. flux angle ρ_* and flux magnitude $\Psi_r \sim I_m$. There are a number of techniques that can be applied, among which the direct and the indirect method. An elaboration on these two techniques will be made in the following sections.

Direct measurement of the air gap flux From the previous chapters it becomes clear that up to date information on the magnitude and phase of the fundamental flux wave is of great importance since this is the basis of coordinate transformation. In order to obtain the flux signals one could attempt to measure the flux density in the air gap of the machine directly by placing suitably spaced Hall sensors on the face of the stator teeth. However apart from the fact that tiny Hall sensors are mechanically fragile sensors which would not stand up very well under the severe vibrations and thermal stress, there are large harmonics caused by the rotor slots, the frequency of which changes with speed. Furthermore, the accuracy of a torque signal computed from this signal is likely to be poor since torque is an integral surface related quantity which is difficult to estimate on the base of a few local field measurements. Another disadvantage of this scheme is that the motor would have to be fitted with these sensors, therefore it would no longer be a standard motor. [7]

Estimating the air gap flux In order to avoid active semiconductor elements a quite different approach can be applied. This approach is based on the model equations of the motor in flux coordinates as described section 2.3. These equations have been plotted block schematically on the righthand side of figure 2.13.

The stator current I_s and the speed ω_m serve as input functions with the motor being described by a single parameter τ_r. Before the stator current is expressed in field coordinates one transformation has to be performed from a stator coordinate frame to a field coordinate frame. This transformation requires knowledge of the flux angle ρ_*, which can be obtained

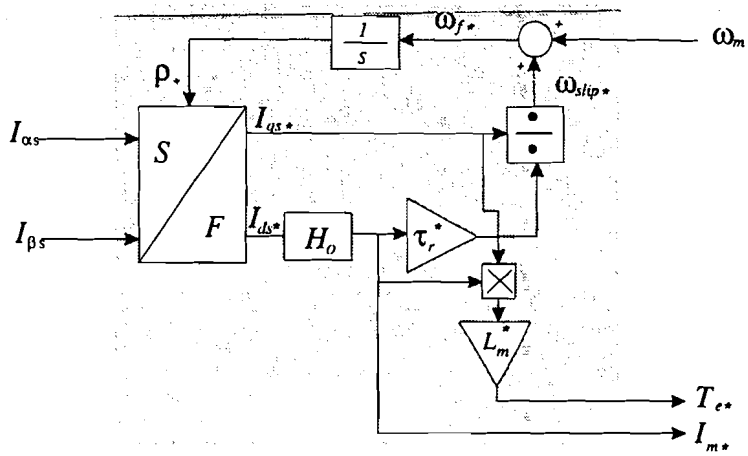

Figure 2.13: Block diagram of the observer

by integration of equation 2.51. The coordinate transformation block inhabits the following expression

$$\begin{pmatrix} I_{ds*} \\ I_{qs*} \end{pmatrix} = \begin{bmatrix} \cos\rho_* & \sin\rho_* \\ -\sin\rho_* & \cos\rho_* \end{bmatrix} \begin{pmatrix} I_{s\alpha} \\ I_{s\beta} \end{pmatrix} \tag{2.65}$$

It is obvious that a false angle ρ_* of the flux wave could lead to undesirable coupling between the d- and q axes and could eventually invalidate the idea of control in field coordinates. Proceeding to the right in figure 2.13 it is seen that equations 2.60 and 2.61 are schematically depicted. Block H_o symbolizes the transfer function

$$H_o = \frac{1}{\tau_r^* s + 1} \tag{2.66}$$

This expression has been derived by transferring equation 2.60 to the s-plane. Finally the electric torque can be obtained by evaluating

$$T_{e*} = L_m^* I_{m*} I_{qs*} \tag{2.67}$$

This expression is correct when ρ_* equals ρ.

2.4.2 Indirect field oriented control

It is learned in the previous section that direct field control requires the magnitude of the momentary electromagnetic torque and magnetizing current. These two values can not be measured easily, but can be estimated when the rotor speed and stator current have been measured. When indirect field oriented control is applied only the angular velocity of the rotor axis ω_m has to be known. Instead of applying a feedback control loop with a measured or observed rotor flux use can also be made of feed forward control. The indirect field oriented controller is essentially a nonlinear feed forward controller which has been depicted in figure 2.14. The model has been constructed by making use of equations 2.60 and 2.61. The F/P block symbolizes a field to polar coordinates transformation. The rotor flux angle ρ_* is obtained from

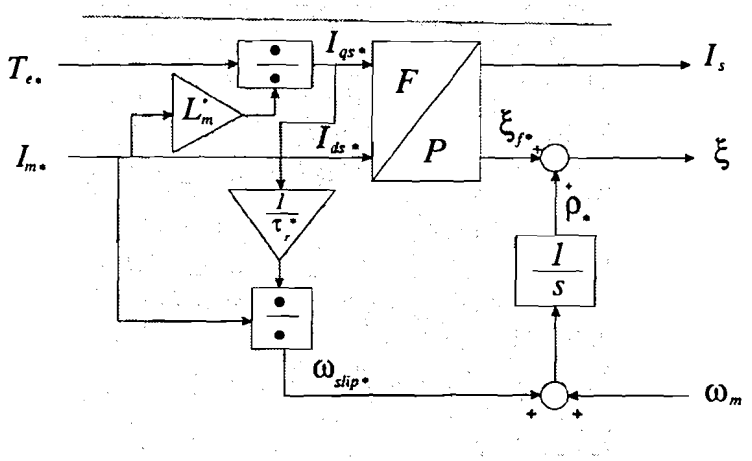

Figure 2.14: Indirect field oriented control

the angular velocity ω_m and the setpoint values T_{e*} and I_{m*} and can be expressed as

$$\rho_* = \theta_m + \theta_{slip*} \tag{2.68}$$

$$\rho_* = \int_0^t \omega_m(\tau)d\tau + \int_0^t \omega_{slip*}(\tau)d\tau \tag{2.69}$$

One other thing that can be seen in figure 2.14 is the equality

$$I_{ds*} = I_{m*} \tag{2.70}$$

It can be seen in figure 2.14 that the parameters R_r^* and L_m^* have an impact on the computation of the flux angle ρ_*. Therefore a deviation between (R_r^*, L_m^*) on the one hand and (R_r, L_m) on the other hand will result in a deviation between ρ_* and ρ.

These deviations are common practice in induction machines control, normally due to temperature and saturation effects.

Chapter 3

Analysis of parameter mismatches in an indirect FOC

3.1 Introduction

In the previous chapter we assumed that the parameters of the induction motor have been identified perfectly. Or in terms of figure 1.3 on page 6: the parameters from set Θ^* are the same as the parameters in set Θ. In this chapter we will analyse the behaviour of the electromagnetic torque, magnetizing current and slip frequency when there exists an error between the motor parameters and the indirect controller parameters. We argued in chapter 1 that a concatenation of an indirect FOC and an induction machine could be modelled by means of figure 1.4 when the parameters have been identified without any error. A parameter error will result in nonlinear coupling terms between the input set (T_{e*}, I_{m*}) and output set (T_e, I_m).

In section 3.2 we will first discuss the steady state behaviour of the concatenated indirect FOC and the induction machine by analysis of the control scheme. The influence from parameter deviation on the phasor diagram becomes apparent in this fashion. This approach gives us however no useful tools to describe the transient behaviour of the indirect controlled induction machine which are caused by parameters deviations between controller parameters and motor parameters. A different approach gives us the opportunity to separate the nonlinear coupling terms from the ideal transfer function of the concatenated indirect FOC and the induction machine. This will be done in section 3.3.

3.2 Steady state behaviour of an indirect controlled induction machine

The indirect field oriented control scheme which has been introduced in section 2.4.2 will be applied on an induction machine. For configurating the indirect field oriented controller we have two parameters at our disposal i.e. the rotor resistance R_r^* and the magnetizing inductance L_m^*. The asterix indicates that we are considering estimated values. We will show that it is more appropriate to use the parameters τ_r^* and L_m^* because they determine both the steady state properties and the the dynamical properties. The parameters that are used in the indirect field oriented controller will not be equal to the parameters in the induction machine in practice. A

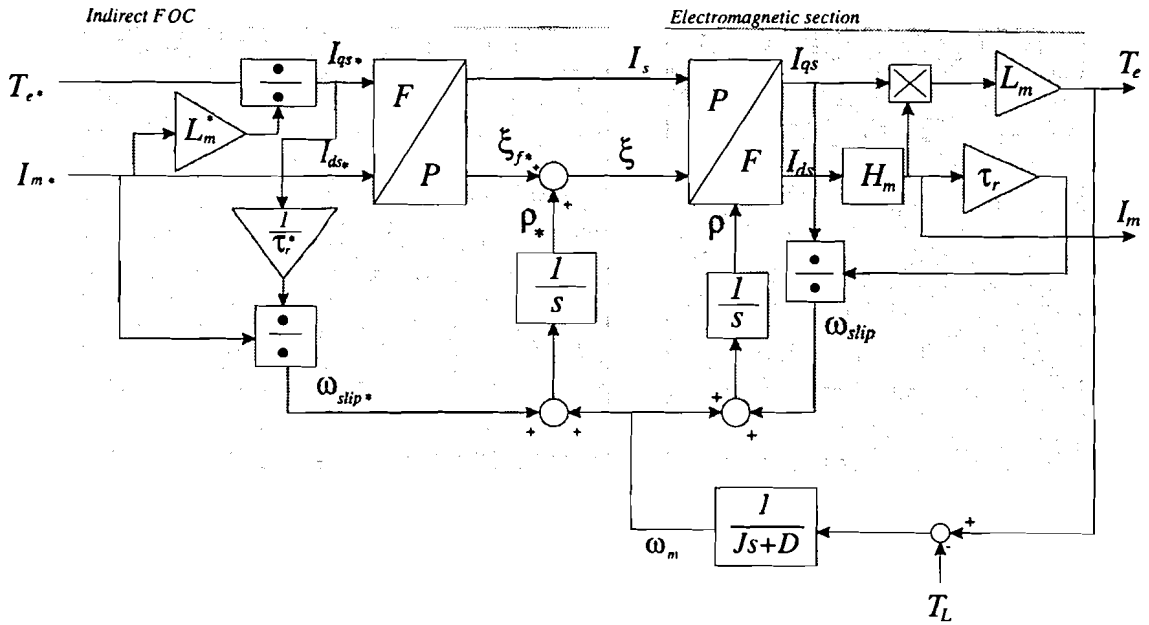

Figure 3.1: Concatenation of the indirect FOC and the induction machine.

distinction between indirect controller parameters and motor parameters will also result in a distinction between controller variables and motor variables. The variables have been summarized in table 3.1.

name	controller	machine
stator angle	ξ_*	ξ
slip angle	θ_{slip*}	θ_{slip}
torque angle	ξ_{f*}	ξ_f
direct component of I_s^F	I_{ds*}	I_{ds}
quadrature component of I_s^F	I_{qs*}	I_{qs}
magnetizing current	I_{m*}	I_m

Table 3.1

Our aim is now to obtain an expression that describes the relationship between motor variables and controller variables. In order to get that expression we will focus on the angles in the controller and in the motor. The angles have been depicted in figure 3.2. The stator current angle ξ can be expressed in two ways

- In machine variables : $\xi = \theta_m + \theta_{slip} + \xi_f$
- In controller variables : $\xi_* = \theta_{m*} + \theta_{slip*} + \xi_{f*}$

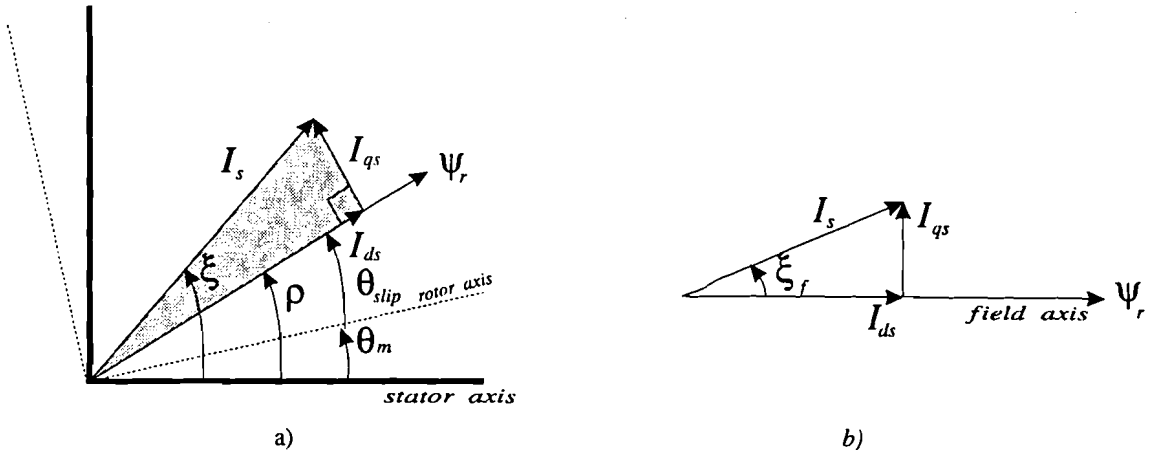

Figure 3.2: Phasor diagram

Both equations have two common variables i.e. stator current angle ξ and rotor axis angle θ_m when we assume that we can neglect the delay of the converter and the tacho generator. The stator current angle ξ is impressed in the stator windings by the converter and θ_m is the rotor axis angle. Therefore $\xi_* = \xi$ and $\theta_{m*} = \theta_m$. Expansion of these two equalities leads to the following equation

$$\theta_{slip} + \xi_f = \theta_{slip*} + \xi_{f*} \tag{3.1}$$

It becomes clear from this equation that the sum of the machine angle $\theta_{slip} + \xi_f$ equals the sum impressed by the indirect controller. There will however be an other distribution between both θ_{slip} and ξ_f on the one hand and θ_{slip*} and ξ_{f*} on the other hand when the machine parameters have not been identified properly. The only restriction is that the sum of both summations in equation 3.1 has to be equal. This can be seen in figure 3.3a, which shows an arbitrary phasor

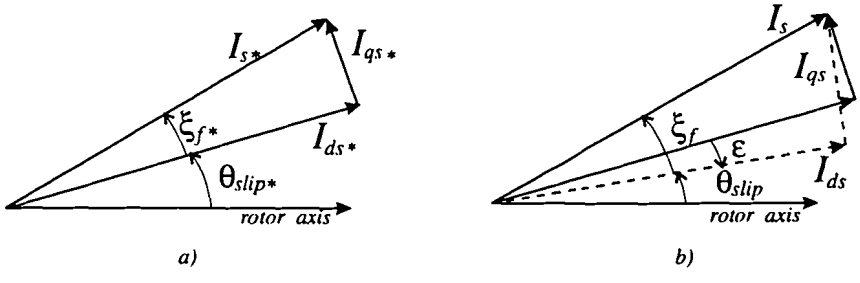

Figure 3.3: Phasor diagram of an indirect FOC a) and an IM b) in case of detuning

diagram of an indirect field oriented controller. There is a fixed distribution between the angles θ_{slip*} and ξ_{f*}. In the motor will be an other distribution between θ_{slip} and ξ_f. The dashed line in figure 3.3b represents the phasor diagram of the motor and the continuous line depicts the phasor diagram of the indirect field oriented controller. It can be seen that there is a small angle ϵ between both phasor diagrams.

The angles θ_{slip*} and θ_{slip} increase with angular velocity ω_{slip*} and ω_{slip} respectively in the steady state. As opposed to the angles ξ_{f*} and ξ_f that remain constant in the steady state. An increase of for instance input T_{e*} will result in an instantaneous increase of the slip frequency ω_{slip*}. This will subsequently result in the fact that θ_{slip*} will increase faster than before. This increase of the slip frequency will not immediately be followed in the motor in the case of detuning. There will be a transient response on this sudden increase of one of the input ports. This can be noticed by an increase or decrease of the magnetizing current magnitude, which is caused by a rotation over some angle ϵ from one steady state to an other. Eventually, ω_{slip*} will be equal to ω_{slip} in the steady state which can be proved by differentiating equation 3.1 and substitution of $\omega_{slip} = \dot{\theta}_{slip}$ and $\dot{\xi}_f = 0$.

Another equality that always holds is

$$I_{s*}^2 = I_s^2 \tag{3.2}$$

$$I_{ds*}^2 + I_{qs*}^2 = I_{ds}^2 + I_{qs}^2 \tag{3.3}$$

The stator current that is impressed by the indirect field controller equals the stator current in the stator windings when we assume that we have an ideal current converter at our disposal.

A question that has not been answered sofar is: How are ξ_f and θ_{slip} distributed internally in the machine? To answer this question we will use the following equations that have been derived in section 2.4.2

$$\omega_{slip} = \frac{I_{qs}}{\tau_r I_m} \tag{3.4}$$

$$\frac{d\rho}{dt} = \omega_m + \omega_{slip} \tag{3.5}$$

$$\tau_r \frac{dI_m}{dt} + I_m = I_{ds} \tag{3.6}$$

$$T_e = L_m I_m I_{qs} \tag{3.7}$$

These equations have been used to construct the block scheme of figure 3.1. The transient behaviour can be described by the linear and nonlinear equations 3.3 to 3.7 and can be analysed by simulating the block scheme of figure 3.1. An elaboration on this will be made in section 3.4. The steady state properties are much simpler to describe than the dynamic properties.

The steady state equality $\omega_{slip*} = \omega_{slip}$ will hold during steady state and substitution of equation 3.4 yields

$$\frac{I_{qs*}}{\tau_r^* I_{m*}} = \frac{I_{qs}}{\tau_r I_m} \tag{3.8}$$

Equation 3.6 learns us that $I_m = I_{ds}$ in the steady state. Furthermore, the equality $I_{m*} = I_{ds*}$ holds always as can be seen in figure 2.14. Thus the torque angle in the motor

$$\xi_f = \arctan\left(\frac{I_{qs}}{I_{ds}}\right) \tag{3.9}$$

goes over to

$$\xi_f = \arctan\left(\frac{I_{qs}}{I_m}\right) \tag{3.10}$$

in steady state. The same goes for the torque angle ξ_{f*} in the field oriented controller. Thus

$$\xi_{f*} = \arctan\left(\frac{I_{qs*}}{I_{m*}}\right) \tag{3.11}$$

Equation 3.8 relates the internal angle ξ_f with the impressed torque angle ξ_{f*} by means of

$$\tan(\xi_f) = \frac{\tau_r}{\tau_r^*} \tan(\xi_{f*}) \tag{3.12}$$

This last expression gives us a clue about the influence of the rotor time constant on the torque angle ratio between ξ_f and ξ_{f*}. Equation 3.3 determines with equation 3.8 the steady state values of I_m and I_{qs}. Equation 3.8 can be rewritten as

$$I_{qs} = \frac{\tau_r I_{qs*}}{\tau_r I_{m*}} I_m \tag{3.13}$$

and describes a line in the (I_m, I_{qs}) plane with a derivative that depends on the values of the parameters τ_r^*, τ_r and the desired values I_{m*} and I_{qs*}. This line intersects with a circle described by the steady state version of equation 3.3

$$I_m^2 + I_{qs}^2 = I_{m*}^2 + I_{qs*}^2 \tag{3.14}$$

This can be seen in figure 3.4. The continuous vector represents the stator current vector in the

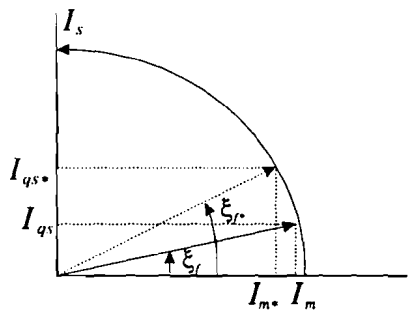

Figure 3.4: Relationship between I_m and I_{qs} when $\tau_r^* < \tau_r$ in the steady state

induction machine and the dashed vector represents the impressed stator current I_{s*} generated by the field oriented controller. It can be seen that both I_s and I_{s*} have the same magnitude which is consistent with equation 3.3. A closer look at figure 3.4 learns us that I_m in the machine will be bigger than I_{m*} when $\xi_{f*} > \xi_f$.

The dependence of the electromagnetic torque T_e on I_m and I_{qs} in the steady state can also be obtained from figure 3.4 by recalling equation 3.7. Substitution learns us that T_e increases as torque angle ξ_f increases.

It is possible to compute the torque deviation with respect to T_{e*} due to the parameter detuning in steady state by combining equation 3.3 and equation 3.8. This yields the following expressions for I_m and I_{qs} as a function of the known signals I_{m*} and I_{qs*}.

$$I_m = \sqrt{\frac{I_{qs*}^2 + I_{m*}^2}{1 + \left(\frac{\tau_r I_{qs*}}{\tau_r^* I_{m*}}\right)^2}} \tag{3.15}$$

$$I_{qs} = \sqrt{\frac{\left(\frac{\tau_r I_{qs*}}{\tau_r^* I_{m*}}\right)(I_{qs*}^2 + I_{m*}^2)}{1 + \left(\frac{\tau_r I_{qs*}}{\tau_r^* I_{m*}}\right)^2}} \tag{3.16}$$

The steady state error between the actual electromagnetic torque and the desired electromagnetic torque can be computed by expanding

$$\begin{aligned} \delta T_e &= T_e - T_{e*} \\ &= L_m I_m I_{qs} - L_m^* I_{m*} I_{qs*} \end{aligned} \tag{3.17}$$

Substitution of equation 3.15 and 3.16 yields an expression which relates δT_e with T_{e*}. This yields

$$\delta T_e = T_{e*} \frac{\delta_{L_m} + \delta_{\tau_r}(1+\delta_{L_m}) + (\delta_{L_m} - \delta_{\tau_r})(1+\delta_{\tau_r}) \left(\frac{T_{e*}}{L_m^* I_{m*}^2}\right)^2}{1 + (1+\delta_{\tau_r})^2 \left(\frac{T_{e*}}{L_m^* I_{m*}^2}\right)^2} \tag{3.18}$$

This relation is characterized by means of $\delta\tau_r$ and δL_m which are described by

$$\tau_r = \tau_r^*(1+\delta_{\tau_r}) \tag{3.19}$$

$$L_m = L_m^*(1+\delta_{L_m}) \tag{3.20}$$

The derivation of equation 3.18 is given in appendix B.1 Equation 3.18 can now be plotted in several plots which gives us an impression about the error between the actual torque and the desired torque in steady state when there exists a parameter mismatch between the indirect controller and the motor.

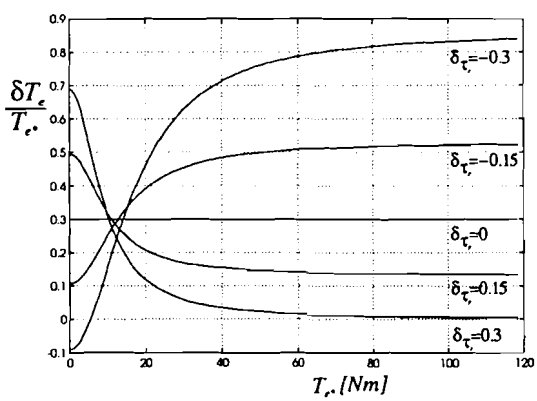

Figure 3.5: Relation between $\frac{\delta T_e}{T_{e*}}$ and T_{e*} when $\delta_{L_m} = 0.3$ and δ_{τ_r} varies between -0.3 and 0.3.

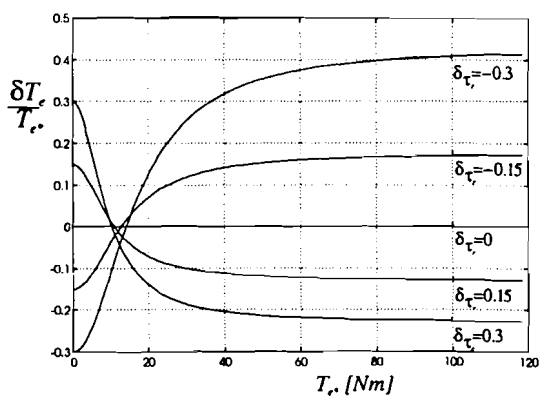

Figure 3.6: Relation between $\frac{\delta T_e}{T_{e*}}$ and T_{e*} when $\delta_{L_m} = 0$ and δ_{τ_r} varies between -0.3 and 0.3.

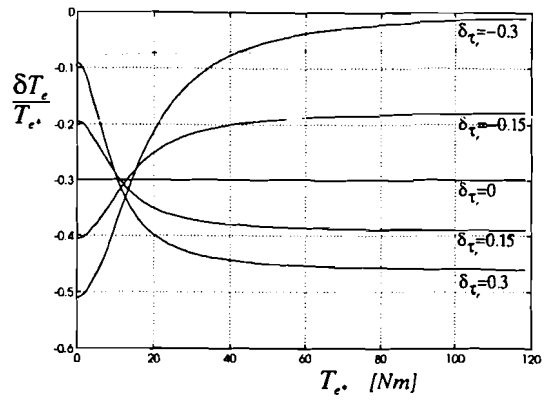

Figure 3.7: Relation between $\frac{\delta T_e}{T_{e*}}$ and T_{e*} when $\delta_{L_m} = -0.3$ and δ_{τ_r} varies between -0.3 and 0.3.

Figure 3.5, 3.6 and 3.7 depict the ratio $\frac{\delta T_e}{T_{e*}} = \frac{T_e - \delta T_e}{T_{e*}}$ as a function from T_{e*} when δ_{τ_r} and δ_{L_m} vary between -0.3 and 0.3. This plot reveals that the nonlinear relationship between T_{e*} and δT_{e*} is solely caused by δ_{τ_r}. Parameter δ_{L_m} causes also an error between δT_e and T_{e*}, but this results in a linear relation between T_{e*} and δT_e. This can be seen by the straight lines in figure 3.5, 3.6 and 3.7 when $\delta_{\tau_r} = 0$.

It can be seen that the ratio $\frac{T_e}{T_{e*}}$ can amount to 0.83 when $\delta_{L_m} = 0.3$ and $\delta_{\tau_r} = 0.3$. Another remarkable conclusion is the fact that the nonlinear behaviour manifests itself especially when $T_{e*} \in [0, 0.4T_{e,max}]$.

3.3 A nonlinear error model

Until sofar we only focussed on the steady state behaviour of the indirect controlled induction machine. A derivation of a model that describes the dynamical behaviour will be made in this section. We will first derive a nonlinear model that describes the behaviour of the output variables (T_e, I_m) as a function from the input variables (T_{e*}, I_{m*}). The dynamical relation between the input and output set is characterized by means of the parameters L_m, R_r, L_m^* and R_r^*. Use will also be made of the time constant in the motor $\tau_r = \frac{L_m}{R_r}$ and the time constant in the controller $\tau_r^* = \frac{L_m^*}{R_r^*}$. It also became apparent in the previous section that the error between the actual torque and the desired torque is determined by δ_{τ_r} and δ_{L_m}. Note that rotor resistance R_r only has an indirect influence on the static behaviour via τ_r.

We can model the magnetizing current in the motor by means of a vector I_m and the magnetizing current in the indirect controller by means of I_{m*}. The angle between both currents is denoted by ϵ. This means that we can distinguish two rotating frames with respect to the stator frame. The indirect controller frame denoted by means of an $()^C$ super script and the second frame is the motor frame, denoted by super script $()^M$. These vectors have been depicted in figure 3.8. It can be seen that the motor frame rotates synchronously with the magnetizing current I_m^S and that the controller frame rotates synchronously with the desired magnetizing current I_{m*}^S. Angle ϵ is the angle between the controller frame and the motor frame due to parameter errors and is defined as

$$\epsilon = \arctan\left(\frac{I_{mb}}{I_{ma}}\right) \tag{3.21}$$

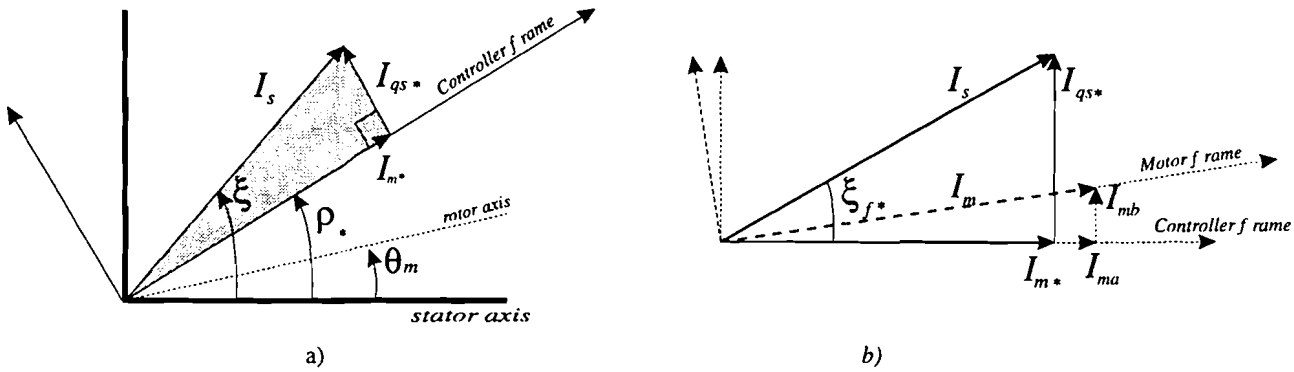

Figure 3.8: Phasor diagram.

The dynamical behaviour of the magnetizing current in the induction machine can be characterized by means of the equation for the rotor circuit in motor coordinates

$$\tau_r \frac{dI_m^M}{dt} + j\tau_r(\dot{\rho} - \dot{\theta}_m)I_m^M + I_m^M = I_s^M \tag{3.22}$$

This equation has already been derived in section 2.3.1. A transformation from motor coordinates $()^M$ to controller coordinates $()^C$ is necessary in order to relate the motor variables with the indirect controller variables. Both frames are related by means of angle ϵ. Thus

$$I_m^M = I_m^C e^{-j\epsilon} \tag{3.23}$$
$$I_{m*}^M = I_{m*}^C e^{-j\epsilon} \tag{3.24}$$
$$I_s^M = I_s^C e^{-j\epsilon} \tag{3.25}$$
$$\rho_* = \rho - \epsilon \tag{3.26}$$

with the following decompositions of I_m^C, I_{m*}^C and I_s^C

$$I_m^C = I_{ma} + jI_{mb} \tag{3.27}$$
$$I_{m*}^C = I_{m*} \tag{3.28}$$
$$I_s^C = I_{m*} + jI_{qs*} \tag{3.29}$$

where I_{ma} is related with the desired magnetizing current I_{m*} by means of the following expression

$$I_{m*} = I_{ma} + \Delta I_{ma} \tag{3.30}$$

The magnetizing current is represented in the motor frame by means of

$$I_m^M = I_m^C e^{-j\epsilon} = (I_{ma} + jI_{mb})e^{-j\epsilon} \tag{3.31}$$

Furthermore, we can relate τ_r with τ_r^* by means of

$$\tau_r = \tau_r^*(1 + \delta_{\tau_r}) \tag{3.32}$$

Substitution of equation 3.25, 3.26, 3.27, 3.30 and 3.32 in 3.22 yields

$$\tau_r^*(1+\delta_{\tau_r})\frac{d}{dt}[(I_{ma}+jI_{mb})e^{-j\epsilon}] + j\tau_r^*(1+\delta_{\tau_r})(\dot{\rho}_* + \dot{\epsilon} - \dot{\theta}_m)(I_{ma}+jI_{mb})e^{-j\epsilon} + \\ +(I_{ma}+jI_{mb})e^{-j\epsilon} = I_s^C e^{-j\epsilon} \tag{3.33}$$

Rearranging this equation and inserting equation 3.30 yields

$$\tau_r^* \frac{d}{dt}[I_{m*}^C - \Delta I_{ma} + jI_{mb}] - j\tau_r^* \dot{\epsilon}(I_{m*}^C - \Delta I_{ma} + jI_{mb})$$
$$+j\tau_r^*(\dot{\rho}_* + \dot{\epsilon} - \dot{\theta}_m)(I_{m*}^C - \Delta I_{ma} + jI_{mb}) + \frac{I_{m*}^C - \Delta I_{ma} + jI_{mb}}{1+\delta_{\tau_r}} = \frac{1}{1+\delta_{\tau_r}} I_s^C \quad (3.34)$$

The nominal model from equation 3.34 which is defined as

$$\tau_r^* \frac{dI_{m*}^C}{dt} + j\tau_r^*(\dot{\rho}_* - \dot{\theta_m})I_{m*}^C + I_{m*}^C = I_s^C \quad (3.35)$$

can be subtracted from 3.34. This yields the following result

$$-\tau_r^* \frac{d\Delta I_{ma}}{dt} + j\tau_r^* \frac{dI_{mb}}{dt} - j\dot{\epsilon}\tau_r^*(I_{m*}^C - \Delta I_{ma} + jI_{mb}) + j\tau_r^*(\dot{\rho}_* - \dot{\theta}_m + \dot{\epsilon})(jI_{mb} - \Delta I_{ma})$$
$$+j\tau_r^*\dot{\epsilon}I_{m*}^C - I_{m*}^C \frac{\delta_{\tau_r}}{1+\delta_{\tau_r}} + \frac{jI_{mb} - \Delta I_{ma}}{1+\delta_{\tau_r}} = -I_s^C \frac{\delta_{\tau_r}}{1+\delta_{\tau_r}} \quad (3.36)$$

This equation can be split in a real part and an imaginary part this yields

$$\tau_r \frac{d\Delta I_{ma}}{dt} + \Delta I_{ma} = -\tau_r(\dot{\rho}_* - \dot{\theta}_m)I_{mb} - \delta_{\tau_r}\tau_r^* \frac{dI_{m*}}{dt} \quad (3.37)$$

$$\tau_r \frac{dI_{mb}}{dt} + I_{mb} = \tau_r(\dot{\rho}_* - \dot{\theta}_m)\Delta I_{ma} - I_{qs*}\delta_{\tau_r} \quad (3.38)$$

This can be expanded to equation 3.39 and 3.40 by inserting the equality $\dot{\rho}_* - \dot{\theta}_m = \frac{I_{qs*}}{\tau_r^* I_{m*}}$

$$\tau_r \frac{d\Delta I_{ma}}{dt} + \Delta I_{ma} = -\tau_r \frac{I_{qs*}}{\tau_r^* I_{m*}} I_{mb} - \delta_{\tau_r}\tau_r^* \frac{dI_{m*}}{dt} \quad (3.39)$$

$$\tau_r \frac{dI_{mb}}{dt} + I_{mb} = \tau_r \frac{I_{qs*}}{\tau_r^* I_{m*}} \Delta I_{ma} - I_{qs*}\delta_{\tau_r} \quad (3.40)$$

The electromagnetic torque can now be computed by expanding

$$T_e = L_m \mathrm{Im}[I_s^M \overline{I}_m^M] = L_m \mathrm{Im}[I_s^C \overline{I}_m^C] \quad (3.41)$$

where the overline indicates that a complex conjugation operation should be performed. This leads to

$$\begin{aligned} T_e &= L_m \mathrm{Im}[(I_{m*} + jI_{qs*})(I_{ma} - jI_{mb})] \\ &= L_m(-I_{m*}I_{mb} + I_{ma}I_{qs*}) \\ &= L_m(-I_{m*}I_{mb} + (I_{m*} - \Delta I_{ma})I_{qs*}) \end{aligned} \quad (3.42)$$

The deviation between the actual torque T_e and the desired torque T_{e*} is expressed by

$$\delta T_e = T_e - T_{e*} \quad (3.43)$$

$$= L_m(-I_{m*}I_{mb} + (I_{m*} - \Delta I_{ma})I_{qs*}) - L_m^* I_{m*} I_{qs*} \quad (3.44)$$

$$= (L_m - L_m^*)I_{m*}I_{qs*} + L_m(-I_{m*}I_{mb} - \Delta I_{ma}I_{qs*}) \quad (3.45)$$

The linear model and its nonlinear error model are depicted in figure 3.9. The *NL*-blocks inhabit the following nonlinear algebraic functions

$$\mathrm{NL}_1: \quad I_{qs*} = \frac{T_{e*}}{L_m^* I_{m*}} \quad (3.46)$$

$$\mathrm{NL}_2: \quad \delta I_m = \sqrt{(I_{m*} - \Delta I_{ma})^2 + I_{mb}^2} - I_{m*} \quad (3.47)$$

$$\mathrm{NL}_3: \quad \delta T_e = (L_m - L_m^*)I_{m*}I_{qs*} + L_m(-I_{m*}I_{mb} - \Delta I_{ma}I_{qs*}) \quad (3.48)$$

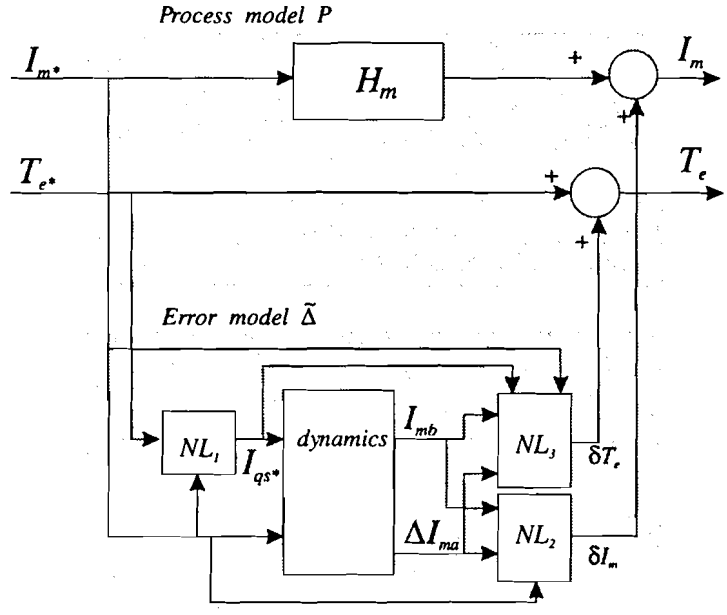

Figure 3.9: Linear model and nonlinear error model.

We now have an ideal linear process model that describes the dynamical behaviour when the parameters have been identified perfectly and a nonlinear error model that describes the additive terms that appear when there exists a deviation between the controller parameters and the motor parameters.

Analysis of equation 3.45 learns us that the magnetizing inductance is solely responsible for the static gain in the error model and that the rotor time constant τ_r determines the dynamics in the error model. This also means that the transient behaviour in the error model only occurs when $\delta_{\tau_r} \neq 0$. Substitution of $\delta_{\tau_r} = 0$ and δ_{L_m} yields that δT_e follows its reference instantaneous. It can also be seen that the presented nonlinear error model is consistent with the results from section 3.2. We can prove this by checking the steady state version from equation 3.39 and 3.40

$$\Delta I_{ma} = -\tau_r \frac{I_{qs*}}{\tau_r^* I_{m*}} I_{mb} \tag{3.49}$$

$$I_{mb} = \tau_r \frac{I_{qs*}}{\tau_r^* I_{m*}} \Delta I_{ma} - I_{qs*} \delta_{\tau_r} \tag{3.50}$$

Substitution of equation 3.50 in 3.49 yields the following expression

$$\Delta I_{ma} = -\left(\tau_r \frac{I_{qs*}}{\tau_r^* I_{m*}}\right)^2 \Delta I_{ma} - \tau_r \frac{I_{qs*}}{\tau_r^* I_{m*}} \delta_{\tau_r} I_{qs*} \tag{3.51}$$

or

$$\Delta I_{ma} = \frac{\delta_{\tau_r} \tau_r \frac{I_{qs*}^2}{\tau_r^* I_{m*}}}{1 + \left(\frac{\tau_r I_{qs*}}{\tau_r^* I_{m*}}\right)^2} \tag{3.52}$$

Substitution from equation 3.49 in 3.50 yields the following expression for I_{mb}

$$I_{mb} = -\frac{\delta_{\tau_r} I_{qs*}}{1 + \left(\frac{\tau_r I_{qs*}}{\tau_r^* I_{m*}}\right)^2} \tag{3.53}$$

These two components can now be inserted in equation 3.45.

This has been done in appendix B.2. The steady state expression for δT_e, computed by focussing on the steady state behaviour of the nonlinear differential equations has the same result as equation 3.18 in section 3.2 where we only considered static behaviour. It can be seen that both ΔI_{ma} and I_{mb} will equal zero when $\delta_{\tau_r} = 0$. Furthermore I_{mb} will become negative when $\delta_{\tau_r} > 0$ which means, as can be seen in figure 3.8 that torque angle ξ_f will increase. This is consistent with equation 3.12.

3.4 Transient behaviour of the induction machine

The scheme that has been depicted in figure 3.1 inhabits the nonlinear equations which characterize the behaviour of the induction motor. This model can only be used to analyse the transient behaviour of the induction machine if we assume that the stator current can be impressed without any delay and that the angular velocity of rotor axis can be measured without an error.

We will subsequently present the internal variables such as the magnetizing current in motor field coordinates I_m^M, slip frequency ω_{slip} and torque angle ξ_f in the motor. These variables result eventually in an electromagnetic torque T_e that is generated in the induction machine. The transient behaviour of T_e will be presented in section 3.4.2

3.4.1 Simulation of the internal variables

The concatenation of an indirect FOC and an IM is supplied with a pulsating input signal T_{e*} with a period time of 4 seconds and a constant magnetizing current $I_{m*} = 20$ A. T_{e*} has been depicted in figure 3.10 when the amplitude of T_{e*} varies between $0.15T_{e,max}$ and $0.78T_{e,max}$. The internal variables ω_{slip}, I_m and ξ_f have been simulated. Each simulation is carried out for different values of δ_{τ_r} i.e. $\delta_{\tau_r} = -0.3, 0, 0.3$ and $\delta_{L_m} = 0$.

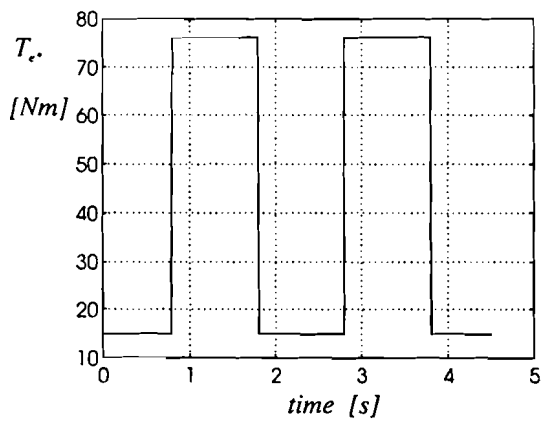

Figure 3.10: Input signal T_{e*}.

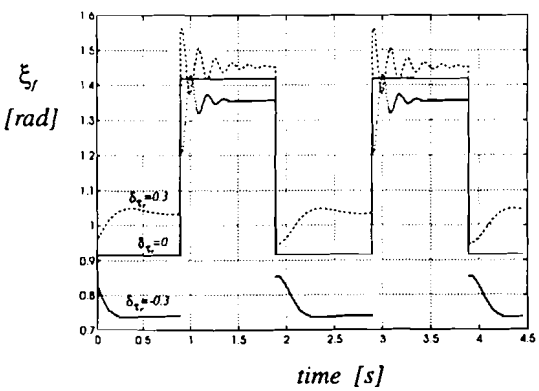

Figure 3.11: ξ_f when δ_{τ_r} varies between -0.3 and 0.3 and $\delta_{L_m} = 0$.

Magnetizing current The magnetizing current can ideally be described by the first order process depicted by block H_m in figure 1.4 on page 6 and will remain constant when the rotor time constant has been identified perfectly. Thus when the angle ξ_f in figure 3.4 does not change. As opposed to the situation when the rotor time constant in the indirect controller deviates from the actual value in the motor. This will result in a magnitude and phase change of vector I_m. This vector will rotate to an other position in figure 3.4. Torque angle ξ_f will increase when $\tau_r^* < \tau_r$ in conformance with equation 3.12. A bigger torque angle ξ_f will also result in a smaller I_m magnitude. It is clear that in case of a parameter mismatch an undesired coupling between T_{e*} and I_m occurs. This can be seen in figure 3.14 where a change of input T_{e*} affects the magnitude of the magnetizing current.

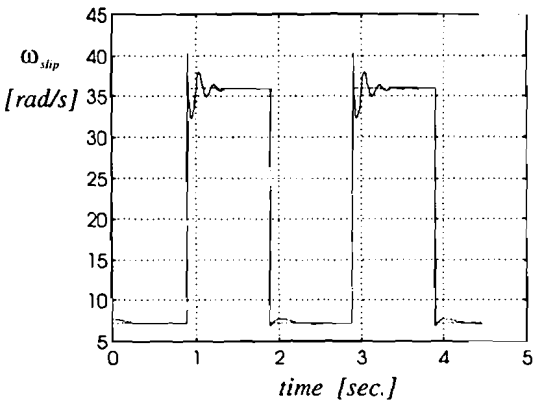

Figure 3.12: ω_{slip} when $\delta_{\tau_r} = 0$, $\delta_{L_m} = 0$ (dashed line) and $\delta_{\tau_r} = -0.3, \delta_{L_m} = 0$ (cont. line)

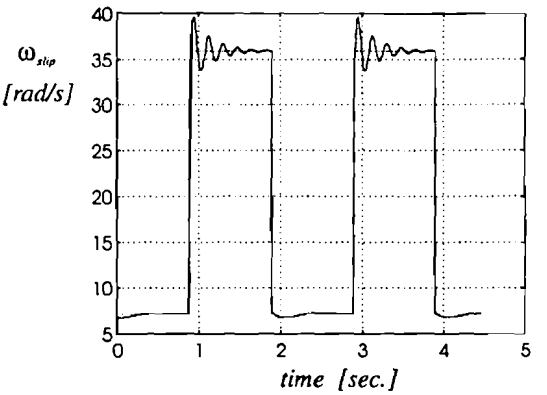

Figure 3.13: ω_{slip} when $\delta_{\tau_r} = 0$, $\delta_{L_m} = 0$ (dashed line) and $\delta_{\tau_r} = 0.3$, $\delta_{L_m} = 0$ (cont. line)

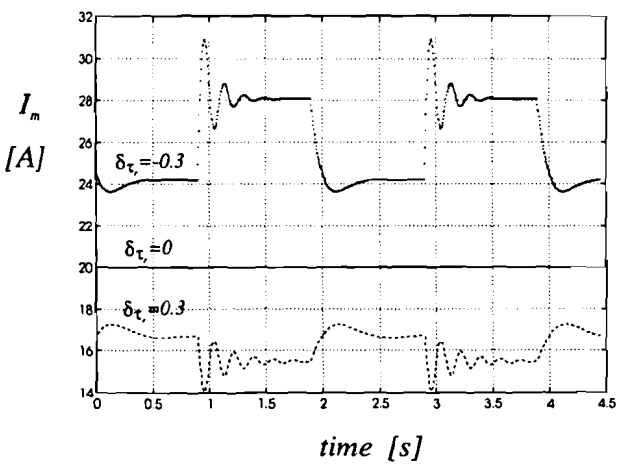

Figure 3.14: I_m when δ_{τ_r} varies between -0.3 and 0.3.

Slip frequency The transient behaviour of the electromagnetic torque and magnetizing current is caused by a changing distribution between the angles $\theta_{slip}(t)$ and ξ_f. The slip frequency $\omega_{slip}(t)$ in the motor will change during a change over from one angle distribution to an other. This difference in slip frequency between the indirect controller and the motor will only be present when $\tau_r^* \neq \tau_r$. The steady state values from ω_{slip*} and ω_{slip} will be equal, independent from the error in the rotor time constant. The results can be found in figure 3.12 and 3.13. Figure 3.11 shows that torque angle ξ_f becomes smaller than angle ξ_{f*} in the indirect FOC (cont. line in figure 3.11) when $\delta_{\tau_r} = -0.3$ and bigger than ξ_{f*} when $\delta_{\tau_r} = 0.3$.

The slip frequency will not reach its desired value immediately when the rotor time constant in the indirect field oriented controller is not correct. This transient of ω_{slip} causes also a transient behaviour of the torque angle ξ_f which has been depicted in figure 3.12. This transient behaviour is caused by the magnetizing current, which magnitude changes due to the new angle distribution in the induction motor.

3.4.2 The electromagnetic torque

The electromagnetic torque T_e follows its reference T_{e*} immediately when $\delta_{\tau_r} = 0$ and $\delta_{L_m} = 0$. T_e follows its reference value without any delay, due to the fact that I_m remains at the same magnitude which can be seen by the continuous line in figure 3.14. The electromagnetic torque T_e, produced by the motor will be smaller than the desired torque T_{e*} when $\tau_r^* < \tau_r$ and the electromagnetic torque will be bigger than T_{e*} when $\tau_r^* > \tau_r$. This can be explained by means of equation 3.12 which tells us that torque angle ξ_f in the motor will be smaller than the desired angle ξ_f when $\tau_r^* > \tau_r$. The undesirable transient behaviour of T_e when $\tau_r^* \neq \tau_r$ is caused by the fact that the magnetizing current I_m has to change its magnitude which is described by a first order transfer function with time constant τ_r.

Three situations have been simulated

- The torque variation for various values of δ_{L_m} have been depicted in figure 3.15 when $\delta_{\tau_r} = 0$. We stated in section 3.3 that there is only a static deviation between T_{e*} and T_e when $\delta_{L_m} \neq 0$ and $\delta_{\tau_r} = 0$. The simulations have been carried out when I_{m*} remains on a constant value ($I_{m*} = 20A$) and T_{e*} changes as has been plotted in figure 3.10. It can be seen that there is no transient behaviour due to the fact that I_m remains constant during a changeover from one steady state to another as can be seen in figure 3.14.

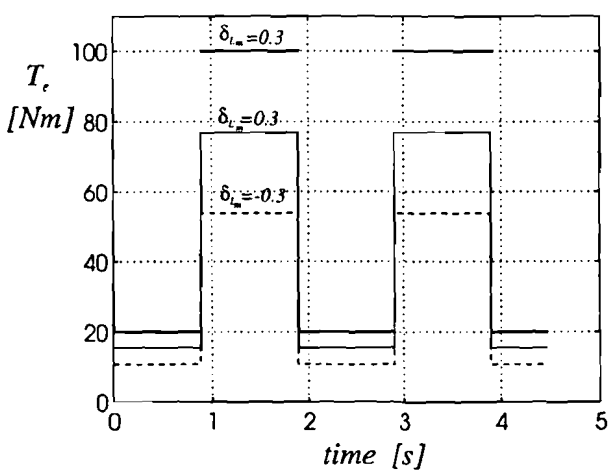

Figure 3.15: T_e when $\delta_{\tau_r} = 0$, $\delta_{L_m} = 0.3$, $\delta_{L_m} = 0$ and $\delta_{L_m} = -0.3$.

- Simulations have been carried out when we consider the parameter deviations that have been listed in table 3.2.

δ_{L_m}	δ_{τ_r}	appendix
0.3	0.3	C.1
0.3	-0.3	C.2
0	0.3	C.3
0	-0.3	C.4
-0.3	0.3	C.5
-0.3	-0.3	C.6

table 3.2

The plots show that all step response plots in appendix C contain a harmonic oscillation with a frequency of approximately 5 Hz which is equal to $\approx \frac{1}{\tau_r}$.

It can also be seen that δ_{L_m} results in a feed through component. For example comparison of figure C.1 and C.2 shows that there is a feed through component. δT_e follows T_{e*} instantaneous until $\delta T_e = 30$Nm. The harmonic oscillation starts from this feed through level. The same can be said for the cases when $\delta_{L_m} = 0$ and $\delta_{L_m} = -0.3$. The plot when $\delta_{L_m} = 0$ does not show a feed through component and the feed through component is $\delta T_e = -30$Nm when $\delta_{L_m} = -0.3$.

Another aspect that becomes apparent is the steady state value of δT_e after a step signal has been supplied to the nonlinear error model. The steady state value has a different value for every perturbation. These values have graphically been depicted in figure 3.5, 3.6 and 3.7. The oscillation is positive going if the final value, which depends on figure 3.5, 3.6 and 3.7 is bigger than the starting value, which depends on the feed through value. The opposite can be said for a negative going oscillation.

- Besides a dependence of $\delta T_e = T_e - T_{e*}$ on the parameters mismatches δ_{L_m} and δ_{τ_r} is there also a dependency of δT_e on input signal T_{e*}. This can be seen in appendix D when we take $\delta_{L_m} = -0.3$ and $\delta_{\tau_r} = 0.3$. Increment of the step size of T_{e*} leads to a more oscillatory signal with an also increasing relative error between the steady state value of T_e and T_{e*}. The final value of δT_e can be described by figure 3.7.

In practice will there of course be a combination of these three degrees of freedom (δ_{L_m}, δ_{τ_r} and T_{e*})

Chapter 4

Robust control of an induction machine

The dependence of the induction machine behaviour on parameter deviations has been simulated in chapter 3 and has resulted in a linear nominal model with a nonlinear error model. This nonlinear error model inhabits both the static and dynamic properties of a detuned indirect field oriented controlled induction machine and depends on the difference between the parameters in the indirect field oriented controller and the induction machine. Absence of parameter mismatches and other model deviations would result in an ideal linear model.

In this chapter we will introduce a control loop which can be used to control the angular velocity of the rotor axis. The objective will be to minimize the influence of the load torque on the angular velocity of the rotor axis, despite the presence of a badly tuned indirect field oriented controller. The controller will be developed by applying H_∞ theory on the linear nominal system and the nonlinear error model. This error model is described by two coupled nonlinear differential equations. The approach which eventually lead to a robust controller will be commented in section 4.2 and 4.3. We will start with a description of the control scheme.

4.1 The control scheme

4.1.1 Model description

A nonlinear model has been derived in section 3.3 which consists of an ideal model and a nonlinear error model $\tilde{\Delta}$ which has schematically been depicted in figure 4.1 and can be described by

$$T_e = \tilde{P}_{T_e}(T_{e*}, I_{m*}, \delta_{L_m}, \delta_{\tau_r}) = T_{e*} + \tilde{\Delta}_{T_e}(T_{e*}, I_{m*}, \delta_{L_m}, \delta_{\tau_r}) \tag{4.1}$$

$$I_m = \tilde{P}_{I_m}(T_{e*}, I_{m*}, \delta_{\tau_r}, \delta_{L_m}) = H_m I_{m*} + \tilde{\Delta}_{I_m}(T_{e*}, I_{m*}, \delta_{L_m}, \delta_{\tau_r}) \tag{4.2}$$

The tilde ($\tilde{\cdot}$) denotes the fact that we are considering a nonlinear function. The outputs T_e and I_m are linear dependent on respectively T_{e*} and I_{m*} when there are no parameter mismatches, which are denoted by δ_{L_m} and δ_{τ_r}. They represent the relative deviation between the indirect FOC parameters and the induction machine parameters and are described by

$$L_m = L_m^*(1 + \delta_{L_m}) \tag{4.3}$$

$$\tau_r = \tau_r^*(1 + \delta_{\tau_r}) \tag{4.4}$$

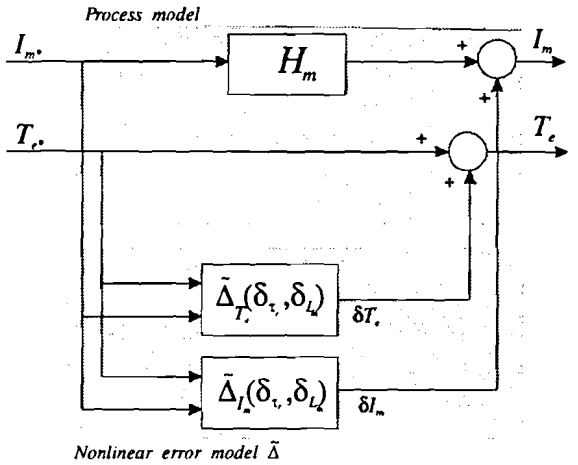

Figure 4.1: Block scheme of nominal model with the nonlinear error model.

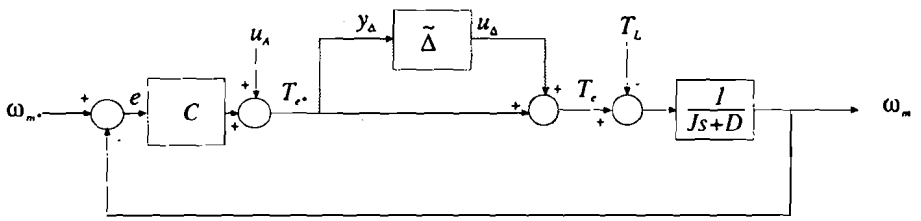

Figure 4.2: Complete feedback system.

T_{e*} and I_{m*} are respectively the desired electromagnetic torque and the desired magnetizing current.

The nonlinear function $\tilde{P}_{T_e}$ between T_{e*} and T_e is determined by a feed through line and a nonlinear error part which is represented by $\tilde{\Delta}_{T_e}$. This dynamical nonlinear function describes the coupling terms that have been derived in section 3.3. Furthermore, the nonlinear function $\tilde{P}_{I_m}$ between I_{m*} and I_m is determined by the linear first order transfer function H_m and the nonlinear error function $\tilde{\Delta}_{I_m}$.

The error model $\tilde{\Delta}$, that has been depicted in figure 4.1, can now be narrowed down to $\tilde{\Delta}_{T_e}$ by stating that the desired magnetizing current I_{m*} remains at a constant level and plays as such no important role in rotor speed control of the induction machine. We will therefore only focus on error model $\tilde{\Delta}_{T_e}$.

4.1.2 The control loop

The complete scheme has been depicted in figure 4.2 and the ranges for both the input nodes and the output nodes of the control scheme have been summarized in table 4.1.

input/output	name	variable	range	bandwidth
input	Set point angular velocity rotor axis	ω_{m*}	$0-100\frac{rad}{s}$	small
	Load torque	T_L	0 – 70 Nm	0-20 $\frac{rad}{s}$
output	Electromagnetic torque	T_e	0 – 100 Nm	
	angular velocity rotor axis	ω_m	$0-100\ \frac{rad}{s}$	

table 4.1

The bandwidth of ω_{m*} is small and will be specified when we design the controller in section 4.3. It can be seen that the actual angular velocity of the rotor axis ω_m is fed back and the error signal between the desired angular velocity ω_{m*} and the actual angular velocity is supplied to the controller C. The angular velocity of the rotor axis is measured by a tacho generator.

The output of controller C is the command signal T_{e*}. This is the electromagnetic torque we wish to excite in the induction machine and is disturbed by the nonlinear error model. This error model can also be regarded as a multiplicative error model of $\frac{1}{Js+D}$. This approach will be used in section 4.2.

The electromagnetic torque T_e is a quantity that can not be measured but determines the angular velocity of the rotor axis with disturbance input T_L, inertia J and damping factor D. Both J and D have been chosen as a constant in this set up, but might change in practice due to the fact that they are dependent on the load that is driven by the induction machine.

It will not be possible to compute a controller that is applicable in the complete setpoint range due to the fact that the tracking bandwidth is limited by the electromagnetic torque that can be generated in the induction machine. This means that the maximimum amplification factor between ω_{m*} and T_{e*} is limited by $\frac{T_{e*}}{\omega_{m*}} = \frac{100}{100} = 1$ if we want to prevent converter overflow. This constraint would reduce the tracking bandwidth significantly. This constraint can however be weakened by supplying input u_A with a feed forward controller that adjusts reference T_{e*} in such a fashion that the rotor axis accelerates until the desired angular velocity of the rotor axis is reached. This means in practice that u_A is set on the maximal allowable T_{e*} value until the desired angular velocity is reached. Input u_A bypasses the controller C until the desired ω_{m*} is reached. The controller C takes over from there. This has been depicted in figure 4.3.

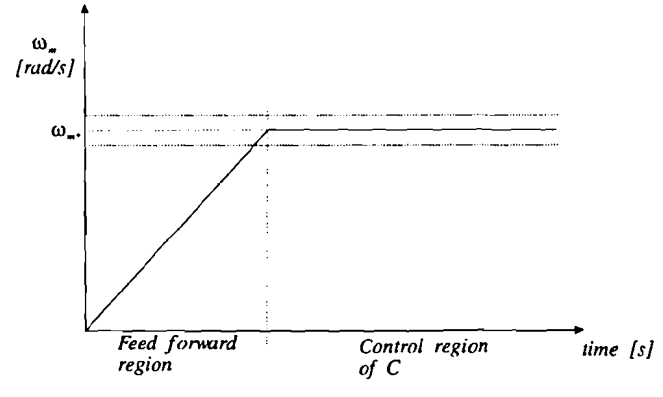

Figure 4.3: Angular velocity of the induction machine.

This approach tells us that a fast tracking system will not be possible. The design objectives will be commented in the next section.

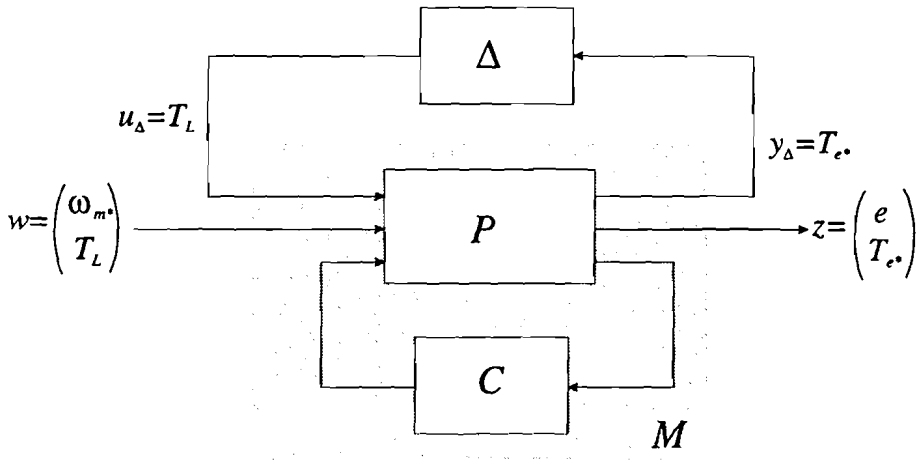

Figure 4.4: Linear fractional transformation.

4.1.3 The design objectives

The controller C is not designed to guarantee a fast tracking of reference input ω_{m*} but to attenuate the influence of disturbance input T_L on error signal $e = \omega_m - \omega_{m*}$. It is necessary to define the control objectives before we start designing the controller. The following design objectives can now be formulated with decreasing priority.

- Stability of the control loop for every possible perturbation.
- The influence of disturbance T_L on the error between ω_m and ω_{m*} is supposed to be as small as possible.
- A small steady state error between ω_m and ω_{m*}.
- Preservation of performance in the presence of plant uncertainties.
- Prevention of actuator overflow. The induction machine can only generate an electromagnetic torque in a range that depends on the machine characteristics.

Actuator overflow is not a major criterion in the design of the controller. Because reference value ω_{m*} is kept on a constant value.

4.2 Structuring the control loop in an H_∞ setting

The control scheme of figure 4.2 can now be reconstructed as a Linear Fractional Transformation (LFT) which has been depicted in figure 4.4. Block M has a total of two input vectors (w and u_Δ) and two output vectors (z and y_Δ). The exogenous input vector w and output vector z in our set up are defined as

$$w = \begin{pmatrix} \omega_{m*} \\ T_L \end{pmatrix} \qquad z = \begin{pmatrix} e \\ T_{e*} \end{pmatrix} \tag{4.5}$$

Block M has therefore a total of three inputs and three outputs. However, a closer look at the closed loop system in figure 4.2 learns us that the transfer function between u_Δ and y_Δ is

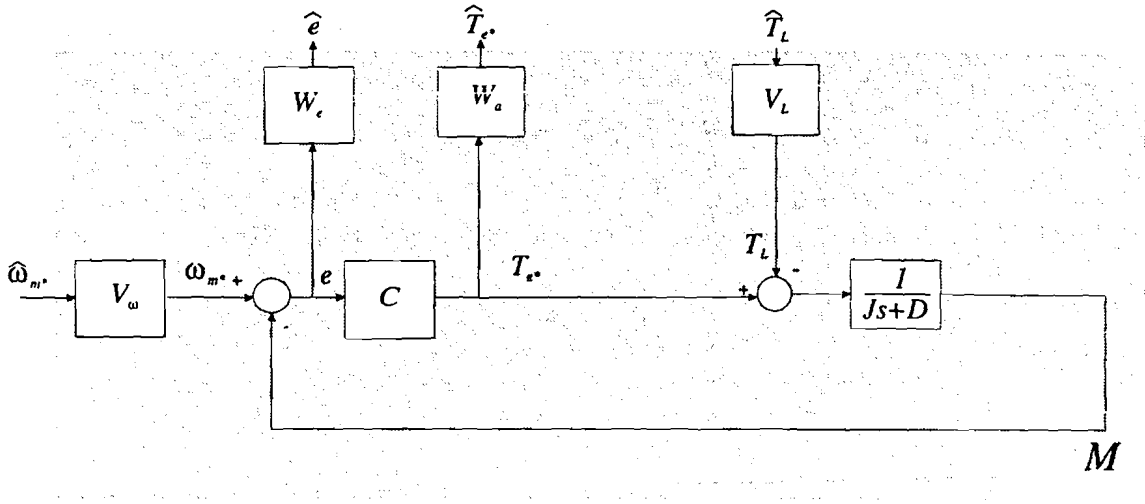

Figure 4.5: Complete feedback system with the weighting filters.

equivalent to the transfer function between T_L and T_{e*}. This has consequences for the size of matrix M, which had an initial size of 3×3, but can be reduced to a 2×2 matrix.

The control objectives can be translated in shaping functions and weighting functions that are augmented to M. These filters have been augmented to the control loop in figure 4.5. This changes the exogenous input vector w and output vector z to

$$w = \begin{pmatrix} \hat{\omega}_{m*} \\ \hat{T}_L \end{pmatrix} \qquad z = \begin{pmatrix} \hat{e} \\ \hat{T}_{e*} \end{pmatrix} \tag{4.6}$$

The shaping functions are used to scale the input signals as

$$T_L = V_L \hat{T}_L \tag{4.7}$$

$$\omega_{m*} = V_\omega \hat{\omega}_{m*} \tag{4.8}$$

with $\|\hat{T}_L\|_2 \leq 1$ and $\|\hat{\omega}_{m*}\|_2 \leq 1$. Note that $\hat{\omega}_{m*}$ and $\hat{T}_L$ are not input signals that can be manipulated, but they are necessary to scale the input signals in such a fashion that the following expression holds for a class of input signals. Thus

$$\|\hat{T}_L\|_2 = \left(\int_{-\infty}^{\infty} \left| \hat{T}_L \right|^2 dt \right)^{\frac{1}{2}} \leq 1 \tag{4.9}$$

and

$$\|\hat{\omega}_{m*}\|_2 = \left(\int_{-\infty}^{\infty} |\hat{\omega}_{m*}|^2 dt \right)^{\frac{1}{2}} \leq 1 \tag{4.10}$$

The filters V_L can be used to shape the power spectra of the expected class of input signals. This can be seen by applying Parsevals theorem on equation 4.9 and 4.10

$$\left(\frac{1}{2\pi} \int_{-\infty}^{\infty} \left| \frac{T_L}{V_L} \right|^2 d\omega \right)^{\frac{1}{2}} \leq 1 \tag{4.11}$$

and

$$\left(\frac{1}{2\pi}\int_{-\infty}^{\infty}\left|\frac{\omega_{m*}}{V_\omega}\right|^2 d\omega\right)^{\frac{1}{2}} \leq 1 \tag{4.12}$$

which shows us that when for example V_ω is a low pass filter, the power spectrum of ω_{m*} would be confined to the profile of V_ω. The objective is to compute the controller C in such a fashion that

$$\|\hat{e}\|_2 < 1 \quad \text{and} \quad \|\hat{T}_{e*}\|_2 < 1 \tag{4.13}$$

This is obtained when $\|M\|_\infty < 1$. LFT matrix M with the augmented shaping filters and weightfilters V_L, V_ω, W_e and W_a is defined as

$$\begin{pmatrix} \hat{e} \\ \hat{T}_{e*} \end{pmatrix} = \begin{pmatrix} W_e \frac{1}{1+\frac{C}{Js+D}} V_\omega & W_e \frac{\frac{1}{Js+D}}{1+\frac{C}{Js+D}} V_L \\ W_a \frac{C}{1+\frac{C}{Js+D}} V_\omega & W_a \frac{\frac{C}{Js+D}}{1+\frac{C}{Js+D}} V_L \end{pmatrix} \begin{pmatrix} \hat{\omega}_{m*} \\ \hat{T}_L \end{pmatrix} \tag{4.14}$$

The four transfer functions that can be distinguished have been listed in table 4.2.

criterion	description	bound	transfer function
M_{11}	tracking	$\frac{\gamma}{W_e V_\omega}$	$\frac{1}{1+\frac{C}{Js+D}}$
M_{12}	disturbance attenuation	$\frac{\gamma}{W_e V_L}$	$\frac{\frac{1}{Js+D}}{1+\frac{C}{Js+D}}$
M_{21}	converter overflow prevention	$\frac{\gamma}{W_a V_\omega}$	$\frac{C}{1+\frac{C}{Js+D}}$
M_{22}	model robustness	$\frac{\gamma}{W_a V_L}$	$\frac{\frac{C}{Js+D}}{1+\frac{C}{Js+D}}$

table 4.2

The main goals of the control design procedure are to guarantee stability in the face of plant uncertainties and to attenuate the influence of the load torque on the angular velocity of the rotor axis. Therefore the 'model robustness' bound and the 'disturbance attenuation' bound prevail over the 'tracking' bound and the 'converter overflow' bound. A system with a large tracking bandwidth is not our aim. The only control property that we require with respect to tracking is a small steady state error.

4.2.1 Nominal performance

The criteria M_{11} (tracking), M_{21} (actuator overflow) and M_{12} (disturbance attenuation) have been mentioned in table 4.2 and are the criteria that are to be optimized. These goals can be formulated in weighting filters and shaping filters which have been augmented to M. Those goals are achieved when $\|W_e M_{11} V_\omega\|_\infty < 1$, $\|W_a M_{21} V_\omega\|_\infty < 1$ and $\|W_e M_{12} V_L\|_\infty < 1$.

We already stated that a small steady state error and 'disturbance attenuation' are more important objectives than a large tracking bandwidth.

4.2.2 Robust stability

In this section we will compare the situation when the error model is described by a linear function Δ and when it is described by a nonlinear function $\tilde{\Delta}$. Lets first focus on the situation when the error model is described by a linear function. The control loop remains stable if

$\|M_{22}\Delta\|_\infty < 1$. This can be analysed by means of the Bode diagrams of both M_{22} and Δ. The H_∞ norm of the closed loop system $M_{22}\Delta$ in the magnitude plot of the Bode diagram is supposed to be smaller than one in order to obtain robust stability. This is a sufficient condition, which means that even if it is violated it can still be stable. We can say that the profile ofM_{22} is bounded by

$$\forall\omega: \ |M_{22}| < \frac{1}{|\Delta|} \tag{4.15}$$

$|\Delta|$ bounds the profile of M_{22} in the Bode diagram. We can say that the maximum value in the magnitude plot of the Bode diagram is the supreme for all bounded signals in L_2. Each input signal can be described as a summation of various Fourier components. Each component is amplified by the corresponding value in the magnitude plot and delayed by the corresponding phase lag in the phase plot. The output signal is composed by adding each resulting frequency component.

This can be generalized for every signal in L_2, due to the fact that the superposition theorem can only be applied on linear systems. This means that if we consider two linear systems $f_1 : u_1 \rightarrow y_1$ and $f_2 : u_2 \rightarrow y_2$ the following expression holds

$$\alpha u_1 + \beta u_2 \rightarrow \alpha y_1 + \beta y_2 \qquad \alpha, \beta \in IR \tag{4.16}$$

This property enables us to use Bode diagrams because there are no cross dependencies between the individual frequency components. For example, supplying a linear system with a sinusoidal input signal with a constant amplitude and constant angular velocity will result in a sinusoidal output signal which has a certain amplitude and a phase angle with respect to the input signal and the same angular frequency as the driving frequency. As opposed to nonlinear systems which can produce components at multiples of the driving angular frequency.

The bound for M_{22} with the nonlinear error model $\tilde{\Delta}$ can now be obtained by applying the small gain theorem to M_{22} and $\tilde{\Delta}$. The product of the H_∞-norm of the nonlinear function $\tilde{\Delta}$ and the linear function M_{22} should be smaller than one. This means that the transfer function M_{22} has a magnitude which is supposed to be smaller than the reciprocal of $|\tilde{\Delta}|$. Thus

$$\forall\omega: \ |M_{22}| < \frac{1}{|\tilde{\Delta}|} \tag{4.17}$$

The question that still has to be answered is: How do we compute the H_∞ norm of the nonlinear error model? This can be done by selecting an input signal which satisfies $\|T_{e*}\|_2 < 1$ and selecting a controller which satisfies $\|\delta T_e\|_2 < 1$. The obtained controller will not satisfy this last condition for every input signal due to the fact that we are dealing with a nonlinear system. We therefore ignored the described dynamics for a while and regarded the input/output set $(T_{e*}, \delta T_e)$ as if the relationship between both signals was described by a linear description. This enables us to describe the relation ship between both input and output signals by a filter $W_{\Delta,i}$. Thus

$$\delta T_e(t) = \int_{-\infty}^{\infty} w_{\Delta,i}(t-\tau) T_{e*}(\tau) d\tau \tag{4.18}$$

with

$$w_{\Delta,i}(t) = \mathcal{L}^{-1}\{W_{\Delta,i}(s)\} \tag{4.19}$$

The obtained filter $W_{\Delta,i}$, $i \in IN$ only holds for that particular data set and will differ from an other filter $W_{\Delta,i}$, $i \in IN$. The filters $W_{\Delta,i}$, $i \in IN$ will be computed for different parameter

perturbations ($\delta_{\tau_r}, \delta_{L_m}$). The input signal that is suplied to the nonlinear error model is a step signal. It appeared in the simulations that the oscillations of output signal δT_e was the biggest when T_{e*} was a step signal. We now have for every data set a filter $W_{\Delta,i}$. Thus, the following holds for a particulary dataset.

$$\|W_{\Delta,i}\Delta_0\|_\infty = \sup_{T_{e*}\in L_2} \frac{\|\delta T_e\|_2}{\|T_{e*}\|_2} \quad i \in IN \tag{4.20}$$

with $\|\Delta_0\|_\infty \leq 1$. Application of the small gain theorem yields

$$\forall\omega: \ |W_{\Delta,i}\Delta_0 M_{22}| < 1 \tag{4.21}$$

Every $W_{\Delta,i}$ that is obtained from the computations is supposed to be bounded by W_Δ. Thus

$$\forall\omega: \ |M_{22}\Delta_0 W_\Delta| < 1 \tag{4.22}$$

The uncertainty filters $W_{\Delta,i}$, $i \in IN$ can be computed by means of the power spectral density functions of T_{e*} and δ_{T_e}, which are respectively denoted by $\Phi_{T_{e*}}$ and $\Phi_{\delta T_e}$. The relationship between input $\Phi_{T_{e*}}$ and output $\Phi_{\delta T_e}$ is described by

$$\Phi_{\delta T_e} = |W_\Delta|^2 \Phi_{T_{e*}} \tag{4.23}$$

Thus,

$$|W_\Delta| = \sqrt{\frac{\Phi_{\delta T_e}}{\Phi_{T_{e*}}}} \tag{4.24}$$

The power density spectra of $\Phi_{T_{e*}}$ and $\Phi_{\delta T_e}$ for several perturbations of δ_{L_m} and δ_{τ_r} have been computed. The corresponding uncertainty filters $W_{\Delta,i}$ are listed in table 4.3 and have been included in appendix E.

δ_{τ_r}	δ_{L_m}	T_{e*} [Nm]	Uncertainty filter	appendix
0.3	0.3	85	$W_{\Delta,1}$	E.1
-0.3	0.3	46	$W_{\Delta,2}$	E.2
0.3	0	109	$W_{\Delta,3}$	E.3
-0.3	0	60	$W_{\Delta,4}$	E.4
0.3	-0.3	155	$W_{\Delta,5}$	E.5
-0.3	-0.3	89	$W_{\Delta,6}$	E.6

table 4.3

The computation of $W_{\Delta,i}(i = 1,\ldots,6)$ has been conducted for different input signals for each perturbation in table 4.3. This is necessary because each perturbation results in a different steady state value for T_{e*}. We can however compute the weighting filters for several perturbations and determine a worst case filter W_Δ that bounds all other uncertainty filters $W_{\Delta,i}(i = 1,\ldots,6)$.

The steady state value of torque command signal T_{e*} depends on δ_{L_m} and δ_{τ_r}. This has already been concluded in section 3.2. Supplying the disturbance input T_L with its maximum value results in a certain value of T_{e*}, which depends on δ_{L_m} and δ_{τ_r} and can be described by

$$J\frac{d\omega_m}{dt} + D\omega_m = T_e - T_L \tag{4.25}$$

The steady state value of ω_m is described by

$$\omega_m = \frac{T_e - T_L}{D} \tag{4.26}$$

And T_e can be expressed as

$$T_e = D\omega_m + T_L \tag{4.27}$$

This value of T_e can be obtained when a certain value of T_{e*} is supplied and depends on δ_{L_m} and δ_{τ_r}, which can be computed with the use of figure 3.5, 3.6 and 3.7 on page 27. Uncertainty filter W_Δ is designed when $\omega_m = 100\frac{rad}{s}$ and $T_L = 70$. These are the maximum values that are supposed to be supplied. Inserting these values in equation 4.26 yields a certain value of T_{e*} which depends on δ_{L_m} and δ_{τ_r}. For example T_{e*} in the second row of table 4.3 can be found as follows. T_e is computed first

$$T_e = D\omega_m + T_L \tag{4.28}$$
$$= 0.1.100 + 70 = 80 \tag{4.29}$$

and T_e is related with T_{e*} via the following expression

$$T_e = T_{e*} + \delta T_e \tag{4.30}$$
$$= T_{e*}\left(1 + \frac{\delta T_e}{T_{e*}}\right) \tag{4.31}$$

The values T_{e*} and $\frac{\delta T_e}{T_{e*}}$ for which this equality holds is $T_{e*} = 46\text{Nm}$. This value is found with the aid of figure 3.5 on page 27.

The power density spectra of the input signal T_{e*} and output signal δT_e are computed in Matlab and application of equation 4.24 yields a plot of $W_{\Delta,i}(i = 1, \ldots, 6)$ for every perturbation. The total uncertainty W_Δ is supposed to bound all the uncertainty filters that have been found in appendix E.1 to E.6. This gives us the rather messy magnitude plot of figure 4.6. Every uncertainty filter $W_{\Delta,i}(i = 1, \ldots, 6)$ for every perturbation that is listed in table 4.3 has been depicted in figure 4.6. Every possible perturbation is bounded by uncertainty filter W_Δ. It can be seen that the filter is to conservative for higher frequencies. The optimal W_Δ filter bounds the maximum values of $W_{\Delta,i}(i = 1, \ldots, 6)$ exactly. This requires the application of a higher order filter. Implementation of a higher order filter in *mhc.m* [4] meets numerical problems. A choice has therefore been made for a second order filter that bounds especially the lower frequencies as good as possible. The following filter has been plotted

$$W_\Delta = 0.8\frac{(\frac{s}{40}+1)(\frac{s}{30}+1)}{(\frac{s}{200}+1)(\frac{s}{250}+1)} \tag{4.32}$$

This filter determines the robust stability constraint which is expressed by

$$\forall\omega : \ |M_{22}|_\infty < \frac{1}{|W_\Delta|} \tag{4.33}$$

This bound can be imposed on the controller design process by demanding that the following bound is satisfied for every frequency.

$$|W_a V_L| \geq |W_\Delta| \tag{4.34}$$

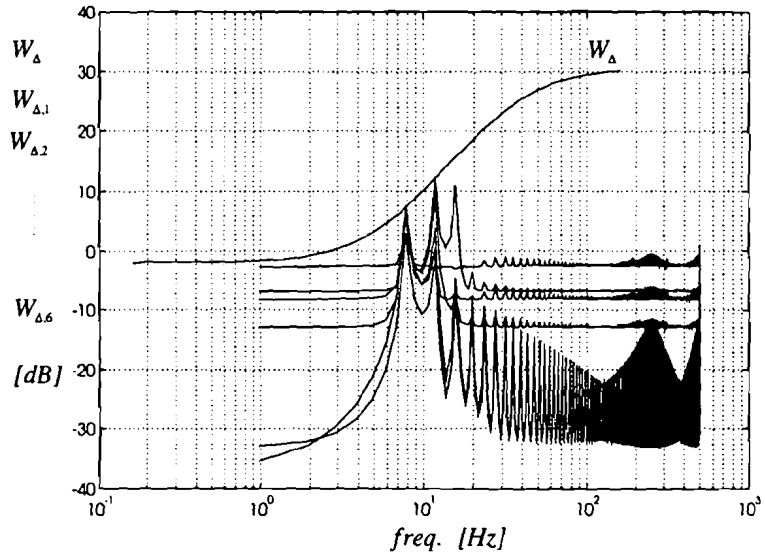

Figure 4.6: Design of uncertainty filter W_Δ.

4.2.3 Robust performance

We would like to maintain the performance bounds that we stated in section 4.2.1 by means of the weighting filters in the presence of the perturbations in $\tilde{\Delta}$. This can be realized when the following condition is satisfied

$$\left\| \begin{array}{cc} W_e \frac{1}{1+\frac{C}{Js+D}} V_\omega & W_e \frac{\frac{1}{Js+D}}{1+\frac{C}{Js+D}} V_L \\ W_a \frac{C}{1+\frac{C}{Js+D}} V_\omega & W_a \frac{\frac{C}{Js+D}}{1+\frac{C}{Js+D}} V_L \end{array} \right\|_\infty < 1 \tag{4.35}$$

4.3 Design procedure

In this section we will develop a robust controller which is stable in the face of the nonlinear error model and has optimal performance and robustness properties. We will first define the design steps that will be followed to obtain controller C. These design steps will be commented in section 4.3.2. The controller will eventually be incorporated in a control loop with the nonlinear error model and simulations will be carried out. This will be done in section 4.3.3

4.3.1 Design steps

The design procedure contains two design phases which are outlined in the following two steps.

Design step 1 'Model robustness' and 'Disturbance attenuation' are more important than the criteria 'tracking' and 'actuator overflow'. We will develop the controllers in such a fashion that M_{22} and M_{21} are the limiting transfer functions which means that there is little space between the actual transfer function and their bounds which are respectively $\frac{\gamma}{W_e V_L}$ and $\frac{\gamma}{W_a V_L}$. γ is defined as the upper bound of the H_∞ norm. If we scale the H_∞ norm of M to one, then γ becomes a scaling factor for the weighting functions.

The input shaping filter V_L and V_ω are respectively set on

$$V_L = 70\frac{\frac{s}{10000}+1}{\frac{s}{20}+1} \tag{4.36}$$

and

$$V_\omega = 1.10^{-9} \tag{4.37}$$

Shaping filter V_L is designed in such a fashion that all possible input signals T_L are confined in V_L. We assume that T_L has a bandwidth of $20\frac{rad}{s}$ and a maximum amplitude of 70Nm. The zero in $s = -10000$ is necessary to keep V_L proper. The other shaping filter V_ω is set on a small value for the time being in order to optimize M_{12} (disturbance attenuation) and M_{22} (model robustness) but will be altered in the second design step. The small value of shaping filter V_ω practically eliminates the influence of the input $\hat{\omega}_{m*}$ on the computation of the controller.

The functions M_{12} (disturbance attenuation) and M_{22} (model robustness) are supposed to be the limiting functions, which means they match the inverse of the corresponding inverse weighting functions in a certain frequency range. The profile of these functions can be imposed by means of W_e, W_a and V_L.

The weighting filter W_e is designed in such a manner that a high penalty is set on low frequencies and a low penalty on high frequencies. This will reduce the influence of the disturbance input on the error node e. Weighting filter W_a puts a high penalty on high frequencies and a low penalty on the low frequencies. The filters are adjusted so that the scaling factor $\gamma < 1$.

design step 2 Until sofar we disregarded input ω_{m*} by fixing V_ω to a very small value. In the second phase we will compose V_ω in such a fashion that V_ω has a passband-level of 100 which is consistent with values that have been listed in table 4.1. The scaling factor γ will become bigger than one when we weigh all frequencies equally. The scaling factor γ can be lowered by changing the profile of V_ω to a low pass filter. This also means that the total set of input signals that can be supplied to the control system becomes smaller. Which still meets our design objectives because we stated that fast tracking is not our objective. The only property that we require with respect to tracking is a small steady state error.

4.3.2 Execution of the design steps

First step A few remarks can be made with respect to the first step. A trade off is made between the criteria 'disturbance attenuation' (M_{12}) and 'model robustness' (M_{22}) which are described by

$$M_{12} = \frac{1}{Js+D}S \tag{4.38}$$

$$M_{22} = C\frac{1}{Js+D}S \tag{4.39}$$

when

$$S = \frac{1}{1+\frac{C}{Js+D}} \tag{4.40}$$

Filter W_a is designed in such a fashion that the robust stability constraint

$$\forall\omega: \ |M_{22}| < \frac{1}{|W_\Delta \Delta_0|} \tag{4.41}$$

is satisfied. The H_∞ norm of error model $\tilde{\Delta}$ bounds the tracking of the closed loop system, because the bandwidth of complementary sensitivity function M_{22} is limited by the profile of W_Δ. This profile of W_Δ can only be imposed on M_{22} by means of W_a and V_L. W_a and V_L bound the 'model robustness' criterion M_{22} according to table 4.1.

Robust stability for all possible perturbation has to be paid for by a poorer disturbance attenuation. This is the trade off that has to be made.

Robust stability can be accomplished when the following inequality holds

$$|W_a V_L| \geq |W_\Delta| \tag{4.42}$$

or

$$|W_a| \geq |W_\Delta V_L^{-1}| \tag{4.43}$$

Thus

$$W_a = \frac{238.1s^3 + 2.143.10^4 s^2 + 6.19.10^5 s + 5.714.10^6}{s^3 + 1.045.10^4 s^2 + 4.55.10^6 s + 5.10^8} \tag{4.44}$$

This filter has been depicted in figure 4.14. The filter W_e is now updated in such a fashion that scaling factor $\gamma < 1$ or in other words

$$\left\| \begin{array}{cc} W_e \frac{1}{1+\frac{C}{Js+D}} V_\omega & W_e \frac{\frac{1}{Js+D}}{1+\frac{C}{Js+D}} V_L \\ W_a \frac{C}{1+\frac{C}{Js+D}} V_\omega & W_a \frac{\frac{Js+D}{C}}{1+\frac{C}{Js+D}} V_L \end{array} \right\|_\infty < 1 \tag{4.45}$$

Filter W_e puts a high penalty on the low frequencies and a low penalty on the high frequencies and has therefore a low pass profile. Application of shaping filter $V_L = 1.10^{-9}$ that we initially defined in section 4.3.1 resulted in numerical problems. V_ω was therefore altered to

$$V_\omega = 0.001 \tag{4.46}$$

The following third order filter of W_e has been found

$$W_e = \frac{2.5}{s^3 + 0.09s^2 + 0.0023s + 0.000015} \tag{4.47}$$

This results in the magnitude plots of figure 4.7 and 4.8. The magnitude plot of M_{11} and M_{12} have been omitted, because they do not produce extra information since V_ω was set on a small value.

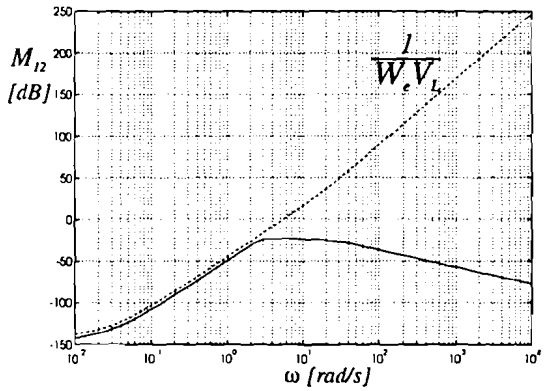

Figure 4.7: Disturbance attenuation M_{12}

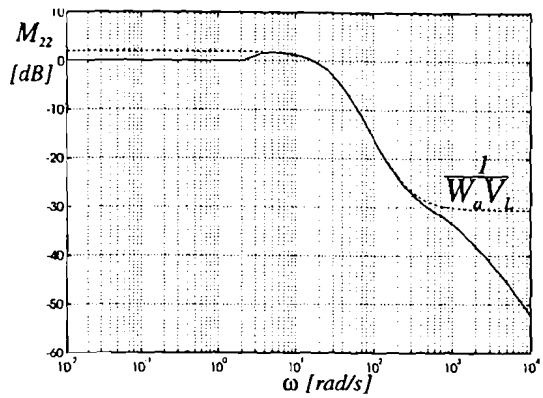

Figure 4.8: Model robustness M_{22}

Second design step The weighting filters W_e and W_a have been designed in the first design step but can be altered in the second design step. This is the case when the design objectives that are to be optimized in the second design step are not met. The following two criteria are optimized

$$M_{11} = S \tag{4.48}$$
$$M_{21} = CS \tag{4.49}$$

which are respectively the functions that determine the 'tracking' criterion and the 'actuator overflow' criterion.

The shaping filter V_ω that has been designed in the first design step is to small. It can be altered by designing V_ω in such a way that all possible input signals are confined in V_ω. A large bandwidth of V_ω will not be necessary because reference ω_{m*} will remain on the same value during operation and has a maximum value of $100\frac{rad}{s}$. The pass band of V_ω will therefore have a value of 100. A small steady state error is the main goal of this design step. This also means that actuator overflow criterion is not an important criterion.

It appears that scaling factor $\gamma = 1.0$ when the following filter is chosen

$$V_\omega = 100\frac{\frac{s}{10000}+1}{\frac{s}{0.01}+1} \tag{4.50}$$

This shaping filter has a small bandwidth but meets our objective to have a small steady state error. This filter has also been depicted in figure 4.14. This results eventually in the following four transfer functions that have been depicted in figure 4.9 to 4.12

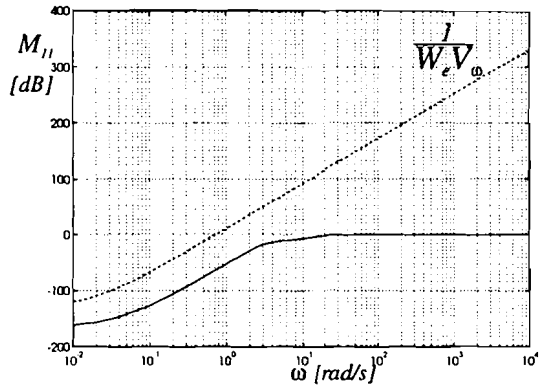

Figure 4.9: Tracking M_{11}

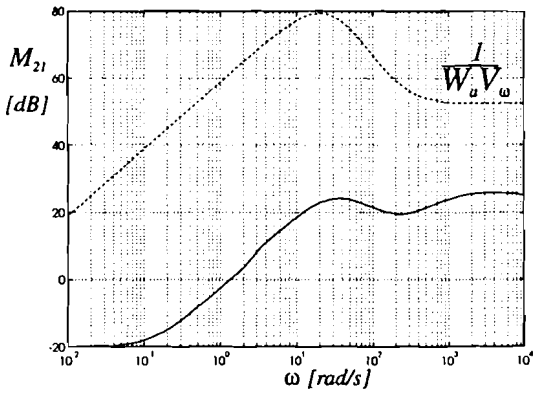

Figure 4.10: Actuator overflow M_{21}

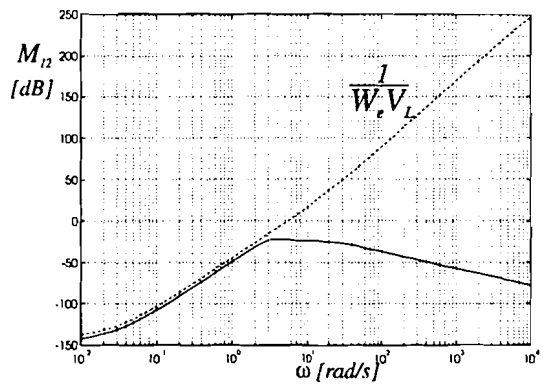

Figure 4.11: Disturbance attenuation M_{12}

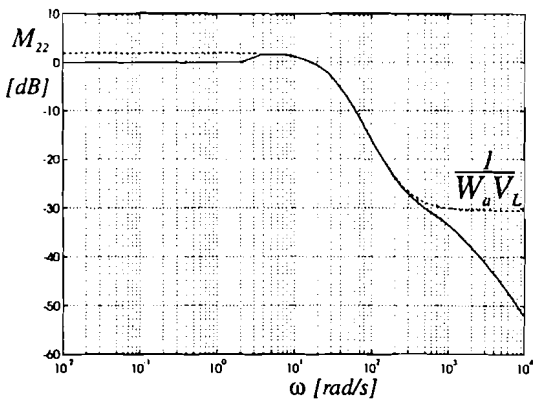

Figure 4.12: Model Robustness M_{22}

It can be seen that the 'model robustness' plot M_{22} in figure 4.12 and the disturbance attenuation plot M_{12} in figure 4.11 are the functions which are closer to their bound than the remaining functions M_{11} and M_{21}. The 'model robustness' plot is bounded by the weights in the angular frequency range over 3 $\frac{rad}{s}$ as the disturbance attenuation plot is bounded for angular frequencies up to 2 $\frac{rad}{s}$.

The controller C that lead to these transfer functions has been depicted in figure 4.13.

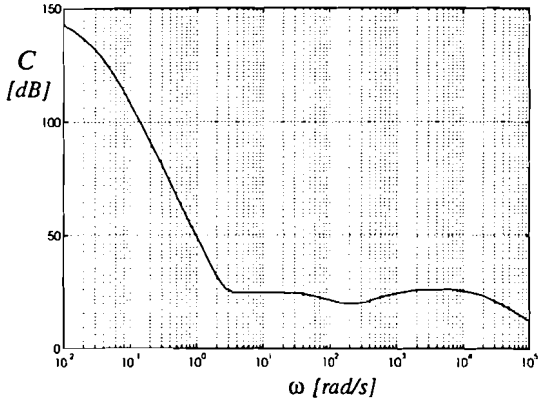

Figure 4.13: Controller magnitude plot

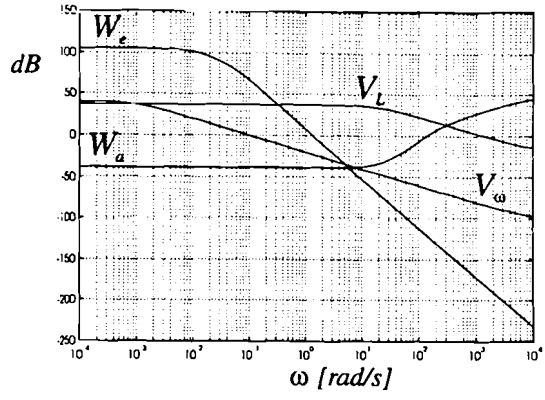

Figure 4.14: Shaping filters and weighting filters

The controller that was originally computed was described by a ninth order transfer function but could be reduced to a sixth order controller by eliminating compensating poles and zeros. The following poles and zeros have been obtained (Static gain=$3.88.10^5$). An asterix denotes a pole zero cancellation.

zeros	poles
-1.10^4*	$-1.89.10^4$
-250	-1.10^4*
-200	-904.31
-20*	-64
$-1.14 \pm 2.39i$	-20*
-0.001*	-0.0484
-2.36	-0.0329
	-0.0087
	$-9.98.10^{-4}$*

Table 4.4

The sixth order controller has been plotted in figure 4.13 with the original eleventh order controller. It can be seen that the magnitude plot of the sixth order controller completely overlaps the original controller in the frequency range that we consider.

4.3.3 Simulation of the controller

Simulations have been carried out when the reduced controller is incorporated in the control scheme with the nonlinear error model that has been depicted in figure 4.2. The simulation lead to the following responses when the rotor rotates with a constant angular velocity of $100\frac{rad}{s}$ and a load torque is switched on. The reference value of T_L changes stepwise to 70Nm and is filtered by a first order filter with different bandwidths which have been listed in table 4.5.

Magnitude of T_L	Bandwidth of T_L	δ_{L_m}	δ_{τ_r}	Appendix
70	20 $\frac{rad}{s}$	-0.3	0.3	F.1
70	20 $\frac{rad}{s}$	-0.3	-0.3	F.2
70	1 $\frac{rad}{s}$	-0.3	0.3	F.3
70	1 $\frac{rad}{s}$	-0.3	-0.3	F.4
70	20 $\frac{rad}{s}$	0	0	F.5
70	1 $\frac{rad}{s}$	0	0	F.6

table 4.5

The behaviour of error signal $e = \omega_m - \omega_{m*}$, torque command signal T_{e*} and the output of the uncertainty model have been depicted. It appears that there is, in the case we consider, a maximum speed change of $4\frac{rad}{s}$ when the maximum allowable load torque is supplied to the control loop with a bandwidth of 20 $\frac{rad}{s}$ and a speed change of $1\frac{rad}{s}$ when the load torque is switched on via a first order filter with a bandwidth of $1\frac{rad}{s}$. This higher amplitude of e when a fast increasing T_L is supplied, can be understand by looking at the disturbance attenuation plot of figure 4.11 where can be seen that signals with an angular frequency higher than $3\frac{rad}{s}$ are amplified with -20dB (=0.1). As opposed to low frequent signals which are amplified by a factor which is smaller than -20dB.

4.4 Comparison of the H_∞ controller with a PI controller

In the previous section we saw that the disturbance input T_L had a big influence on the angular velocity of the rotor axis. This is mainly caused by the fact that the 'model robustness' criterion bounds the complementary sensitivity function of the closed loop and determines therefore the disturbance attenuation criterion in an indirect way.

The magnitude plot of the H_∞ controller in figure 4.13 resembles the magnitude plot of a PI controller, described by

$$H_{pi} = k_p + \frac{1}{\tau_i s} \tag{4.51}$$

Approximation of the H_∞ controller by a PI controller lead to a closed loop system that remained stable for the perturbations that have been listed in table 4.3. Increasing the proportional part k_p to a higher level than the controller in figure 4.13 will result in a better disturbance attenuation but destabilized the loop when k_p becomes too big. It appeared in the simulation that the closed loop system remained stable when $k_p < 55$dB. τ_i is meanwhile kept on such a value that the zero of H_{pi} remains between $10^{-1}\frac{rad}{s}$ and $2\frac{rad}{s}$.

The fact that the control loop remains stable when we implement a PI controller in the control loop does not mean that stability is guaranteed for every possible perturbation due to the fact that the error model is described by nonlinear equations and we only analyzed a finite number of perturbations. But, the cases that have been listed in table 4.3, remained stable when the robust stability constraint of equation 4.33 was violated. We therefore conclude that the small gain theorem that was utilized to guarantee stability is probably a too conservative constraint. Application of a method that makes use of the structure in the error model, such as μ-synthesis, will probably give better results.

Chapter 5

Robust control of a current converter

The study sofar has been based upon the assumption that the stator current could be impressed by an instantaneous responding current converter. If the delay is not negligible, undesirable coupling terms will arise which will confuse indirect field oriented control. Measures can be taken to compensate for these coupling terms by adding decoupling terms in field coordinates prior to the transformation into stator coordinates. The reader is referred to [7] for a detailed explanation of this method.

In this chapter a method is outlined that controls the stator current by manipulating the voltage at the stator windings of the IM, when we assume that we are dealing with an ideal voltage converter. A linear model will be derived in section 5.1 which will be incorporated into an H_∞ setting in section 5.3.

5.1 A linear model of the current converter

The induction machine model that has been depicted in figure 2.6 on page 12 will be used to derive a linear model of the current converter. The stator current control scheme of the asynchronous machine has been depicted in figure 5.1. The actual stator current I_s^S is fed back

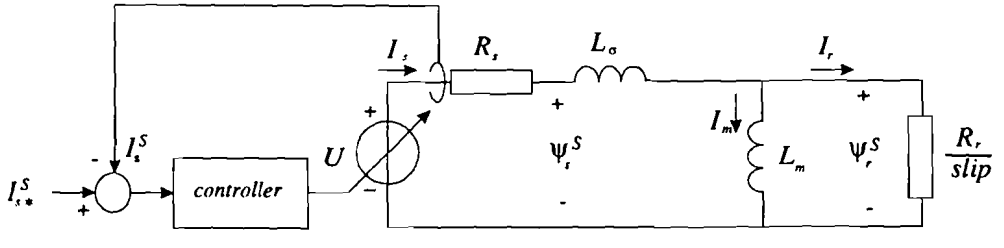

Figure 5.1: Stator current control scheme.

and the error between the desired stator current I_{s*}^S and the actual stator current I_s^S is supplied to the controller. One important consideration is the maximum value of the voltage at the input of the stator windings, which is set on a value of $\sqrt{\frac{2}{3}}\,380$ V.

The controller has to be designed in such a fashion that:

- Only a small phase deviation exists between the desired stator current and the actual stator current.
- There is absence of converter overflow when we know that the converter provides a maximum voltage of $\sqrt{\frac{2}{3}}\ 380\ V = 320\ V$. The $\sqrt{\frac{2}{3}}$ is added as a result of the three phase to two phase transformation that has been made [13].

The objective of the to be designed controller will be to reduce the settling time from the stator current by manipulating the voltage source. We can do this by first analysing the dynamic properties from the stator circuit. A complication in the development of a linear model is the presence of $\frac{R_r}{slip}$ in figure 5.1. The *slip*, defined as $\frac{\omega_0-\omega_m}{\omega}$, is dependent on the load that is driven by the induction machine. The stator current control scheme from figure 5.1 can however be simplified as has been done in figure 5.2. It follows that the stator current can be expressed in

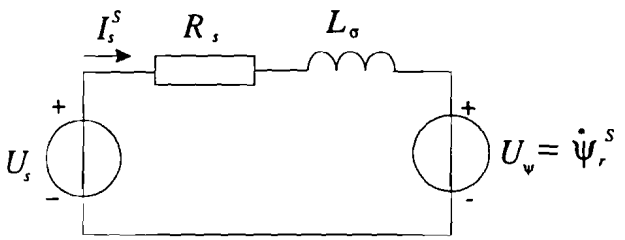

Figure 5.2: Simplified stator current control scheme.

the s-plane as

$$I_s^S(s) = \frac{1}{R_s + sL_\sigma}U_s(s) + \frac{-s}{R_s + sL_\sigma}\Psi_r^S(s) \tag{5.1}$$

Substitution of $\Psi_r^S(s) = L_m I_m^S(s)$ yields

$$I_s^S(s) = \frac{1}{R_s + sL_\sigma}U_s(s) + \frac{-sL_m}{R_s + sL_\sigma}I_m^S(s) \tag{5.2}$$

Introducing

$$H(s) = \frac{-sL_m}{R_s + sL_\sigma} \tag{5.3}$$

and

$$G(s) = \frac{1}{R_s + sL_\sigma} \tag{5.4}$$

yields the following expression for I_s^S

$$I_s^S(s) = G(s)U(s) + H(s)I_m^S(s) \tag{5.5}$$

which has been depicted in figure 5.3. Describing the stator current in this fashion gives us the opportunity to interpret I_m^S as a disturbance input with H representing the 'noise filter' and G the 'process model'. The spectrum of I_m^S will be given in section 5.4. The magnitude plots of G and H have been depicted in figure 5.4. Until sofar we did not use the relation between I_m^S and

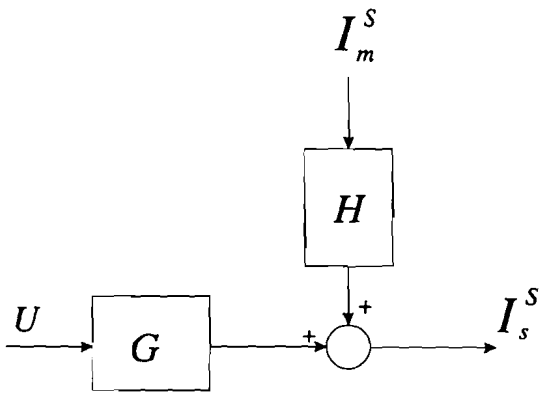

Figure 5.3: Block scheme of a voltage controlled induction machine

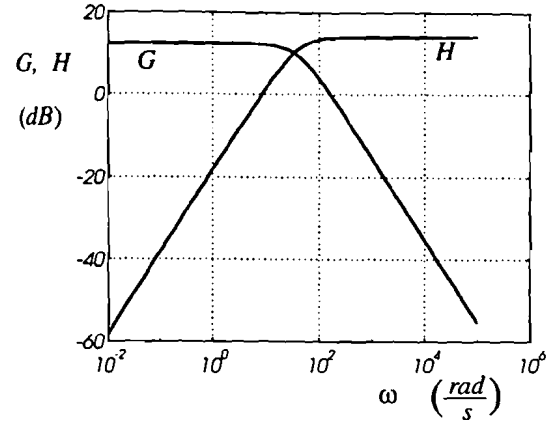

Figure 5.4: Magnitude plot of G and H

I_s^S. Which can be expressed as

$$I_s^S = I_r^S + I_m^S \tag{5.6}$$

with the knowledge that I_r^S is determined by $\frac{R_r}{slip}$ which can be seen in figure 5.1. Therefore, the block scheme of figure 5.3 can be expanded to the scheme that is depicted in figure 5.5.

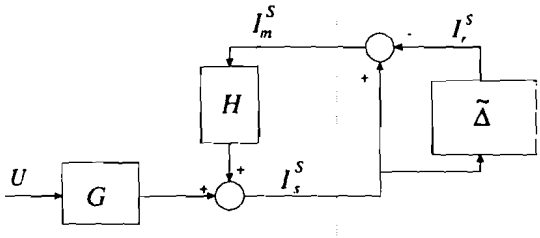

Figure 5.5: Block scheme of a voltage controlled induction machine

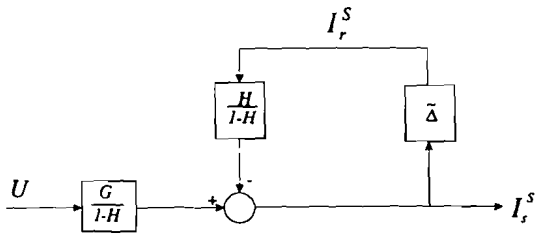

Figure 5.6: Simplified block scheme.

Figure 5.5 can be simplified as 5.7. I_r^S is presented as a disturbance input, but is in fact related with I_s^S in a nonlinear fashion via the *slip* denoted by block $\tilde{\Delta}$ in figure 5.5. Two different approaches can be followed to obtain a linear model.

1. Include block $\tilde{\Delta}$ in the model as a nonlinear uncertainty description.

2. Use magnetizing current I_m^S as disturbance input and disregard everything to the right of the dotted line in figure 5.5.

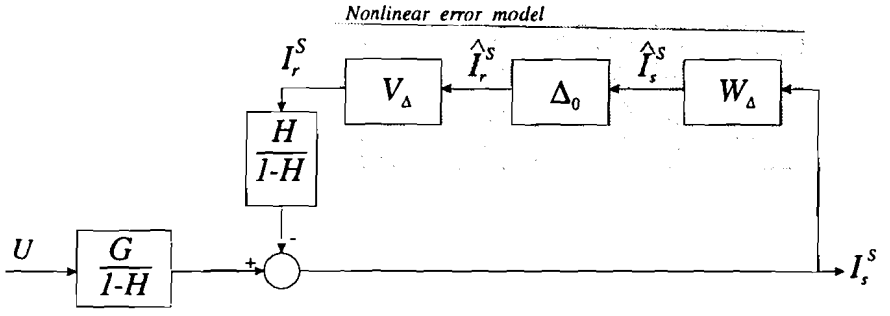

Figure 5.7: Model with expansion of $\tilde{\Delta}$.

Approach 1 Uncertainty block $\tilde{\Delta}$ is described by a nonlinear expression and the H_∞ norm is defined by

$$\|\tilde{\Delta}\|_\infty = \sup_{I_s^S \in L_2} \frac{\|I_r^S\|_2}{\|I_s^S\|_2} \tag{5.7}$$

We can however also look upon $|\tilde{\Delta}|$ as if it was described by

$$|\tilde{\Delta}| = |V_\delta \Delta_0 W_\delta| \tag{5.8}$$

with $\|\Delta_0\|_\infty \leq 1$. This has been depicted in figure 5.7 when both $\hat{I}_r^S$ and $\hat{I}_s^S$ are in the unit ball of bounded power. This tells us that there is no fundamental difference between modelling the relation between I_r^S and I_s^S as an unstructured uncertainty or modelling I_r^S as an independent input with a shaping filter that is described by V_δ.

Approach 2 There is no difference between choosing either I_m^S or I_r^S as a disturbance input. This can be understand by looking at figure 5.1. The voltage U_ψ is determined by I_r^S or I_m^S ($I_m^S = \frac{1}{L_m}\int U_\psi dt$ and $I_r^S = \frac{U_\psi}{R_r}$). Both currents are related with U_ψ and determine therefore both voltage U_ψ.

A choice is made by using a priori information we have about the character of I_m^S and I_r^S. I_m^S is a signal with a constant amplitude when the parameters in the indirect FOC are correct and there is only a relatively small amplitude deviation of $\pm 10\%$ when there is a parameter mismatch. As opposed to I_r^S which does not have a constant amplitude because it is dependent on the torque that is generated in the induction machine. This can also be seen in figure 5.5 where two signals with a varying amplitude (I_r^S and I_s^S) yield a signal with a more or less constant amplitude. It is therefore more appropriate to choose I_m^S as disturbance input.

5.2 The control loop

In the previous section did we make a choice for the model that has been depicted in figure 5.3 where we regard I_m^S as a disturbance input. The objective of the controller design process will be to minimize the influence of the disturbance input I_m^S in the output signal. Another objective is robust performance: the actual stator current I_s^S is supposed to track the desired stator current in the face of perturbations in G. The parameters L_σ, L_m and R_s have a multiplicative error with a relative deviation from their nominal value of $\pm 30\%$.

The complete control scheme with feed forward controller C_{ff}, feed back controller C_{fb} and uncertainty Δ has been depicted in figure 5.8.

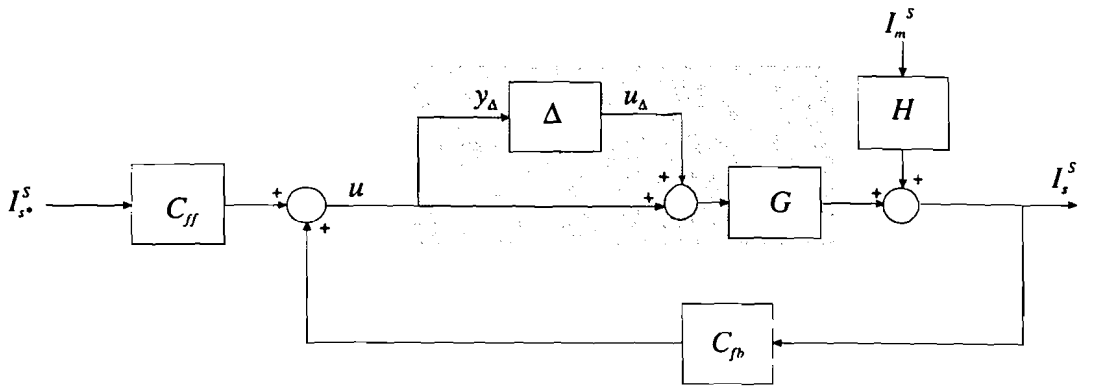

Figure 5.8: Control set up.

Uncertainty Δ can either be modelled as a structured or an unstructured uncertainty. Modelling Δ as a structured uncertainty is possible in this case, due to the fact that the parameters in G can be extracted from G [10] and a controller can be developed that makes use of the structure in the uncertainty description by applying μ-synthesis.

In our case we did not make use of this structure. We can extract the unstructured uncertainty from G by rewriting G as a multiplicative uncertainty description

$$P_G = \{G(1 + W_G\Delta_0) | \|\Delta_0\|_\infty \leq 1\} \tag{5.9}$$

in which uncertainty weight W_G describes the uncertainty profile of the uncertainty as a function of the frequency. The parmeters R_s and L_σ can be described as follows

$$R_s = R_s^*(1 + \delta_{R_s}) \tag{5.10}$$

$$L_\sigma = L_\sigma^*(1 + \delta_{L_\sigma}) \tag{5.11}$$

The transfer function P_G can now be described as follows

$$P_G = \frac{1}{sL_\sigma^*(1 + \delta_{L_\sigma}) + R_s^*(1 + \delta_{R_s})} = \frac{1}{sL_\sigma^* + R_s^*}\left(\frac{sL_\sigma^* + R_s^*}{sL_\sigma^*(1 + \delta_{L_\sigma}) + R_s^*(1 + \delta_{R_s})}\right) \tag{5.12}$$

$$= \frac{1}{sL_\sigma^* + R_s^*}\left(1 + \frac{-s\delta_{L_\sigma}L_\sigma^* - \delta_{R_s}R_s^*}{sL_\sigma^*(1 + \delta_{L_\sigma}) + R_s^*(1 + \delta_{R_s})}\right) \tag{5.13}$$

$$= G(1 + W_G\Delta_0) \tag{5.14}$$

The objective is now to find error filter W_G which bounds the multiplicative errors that can occur. Filter W_G has been in depicted in figure 5.9 and 5.10 when $\delta_{L_\sigma} \in [-0.3, 0.3]$ and when $\delta_{R_s} \in [-0.3, 0.3]$. It appears from the plots that the upper bound of the uncertainties can be described by

$$W_G = 0.42 = -7.5\text{dB} \tag{5.15}$$

The computation of the controller set (C_{fb}, C_{ff}) can be performed by application of H_∞ theory which will be done in the next section. Topics like disturbance rejection, tracking, converter overflow and robust performance will be elaborated on.

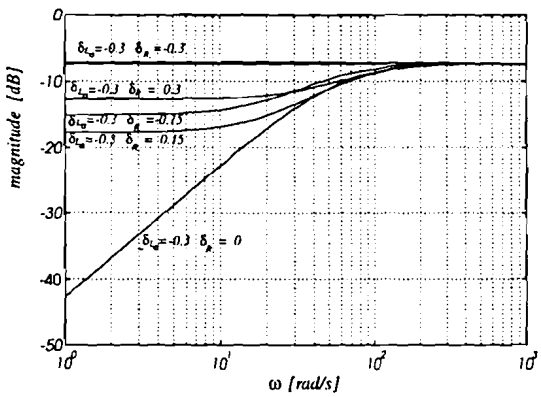

Figure 5.9: W_G when $\delta_{L_a} = -0.3$ and δ_{R_r} varies between -0.3 and 0.3

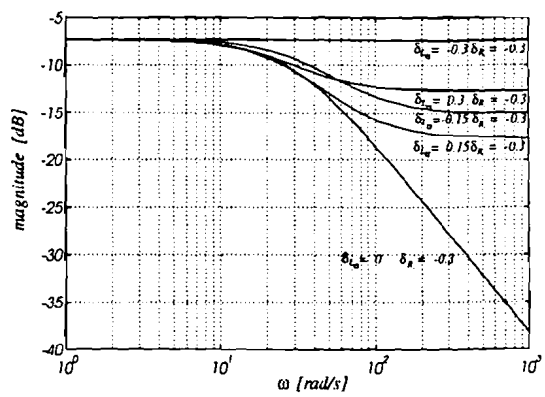

Figure 5.10: W_G when $\delta_{R_a} = -0.3$ and δ_{L_a} varies between -0.3 and 0.3

5.3 H_∞ control of a voltage controlled current converter

In H_∞ control [3] we compare transfer functions by their ∞-norm which is defined as

$$\|H\|_\infty = \sup_\omega(\overline{\sigma}(H)) \tag{5.16}$$

where $\overline{\sigma}(H)$ is the largest singular value of H.

A control scheme can be represented as a Linear Fractional Transformation (LFT) in which the controller C (in our case the controller set C_{fb}, C_{ff}) and uncertainty Δ_0 are extracted from the control scheme. The LFT is depicted in figure 5.11.

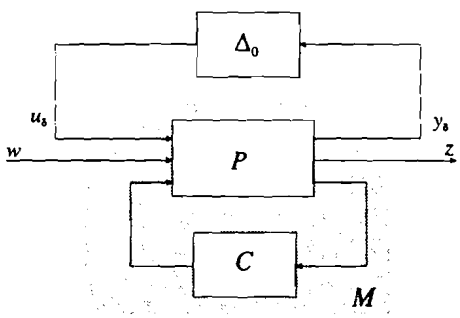

Figure 5.11: Linear fractional transformation

Block P denotes the generalized system and block C represents the generalized controller. The generalized system has three inputs (u_δ, w and u) and three outputs (y_δ, z and y). The exogenous input vector w contains all primary input signals of interest such as disturbances, measurement noise and command signals which are characterized by means of shaping filters. Vector w belongs to the unit ball of bounded power.

The output vector z contains all the outputs we wish to regulate such as the error signal and the actuator command signal. The control objectives can be described by means of weighting

filters which should be designed in such a fashion that w also belongs to the unit ball of bounded power. The exogenous input vector w and output vector z are defined as

$$w = \begin{pmatrix} \hat{I}_{m*} \\ \hat{I}_{s*} \end{pmatrix} \qquad z = \begin{pmatrix} \hat{e} \\ \hat{u} \end{pmatrix} \tag{5.17}$$

We can abbreviate the contents of M as

$$\begin{pmatrix} \hat{e} \\ \hat{u} \\ \hat{y}_\delta \end{pmatrix} = \begin{pmatrix} M_{11} & M_{12} & M_{13} \\ M_{21} & M_{22} & M_{23} \\ M_{31} & M_{32} & M_{33} \end{pmatrix} \begin{pmatrix} \hat{I}_{m*} \\ \hat{I}_{s*} \\ \hat{u}_\delta \end{pmatrix} \tag{5.18}$$

In which $\hat{e}$ is the tracking error and $\hat{u}$ is the stator voltage that is supplied to the stator windings. This matrix contains however some redundant information due to the fact that the nodes $\hat{y}_\Delta$ and $\hat{u}$ are the same as can be seen in figure 5.8. The size of M therefore reduces to a 2×3 matrix. The objective will be to minimize the power of output vector $z(t)$ when input vector $w(t)$ contains time signals that exist in the unit ball of bounded power. We can achieve this by computing an appropriate controller set (C_{fb}, C_{ff}) that satisfies

$$\gamma_0 = \inf_{C_{fb},C_{ff}} \|M(C_{fb}, C_{ff})\|_\infty \quad = \quad \inf_{C_{fb},C_{ff}} \left\{ \sup_{w \in L_2} \frac{\|z\|_2}{\|w\|_2} \right\} \tag{5.19}$$

in which γ_0 is the minimal norm that can be achieved. This is a hard to solve problem and is therefore relaxed to the suboptimal problem which is defined as

$$\|M(C_{fb}, C_{ff})\|_\infty < \gamma \quad \text{with} \quad 0 < \gamma_0 < \gamma \tag{5.20}$$

Our aim is to construct a controller set in such a fashion that the control loop has maximum tracking properties and that there exist no overflow of the voltage converter.

The desired control properties can be translated in a set of shaping and weighting filters which are augmented to M and are depicted in figure 5.12. This can also be expressed as

$$\begin{pmatrix} \hat{e} \\ \hat{u} \end{pmatrix} = \begin{pmatrix} -\frac{W_e H V_m}{1-GC_{fb}} & W_e\left(1 - \frac{GC_{ff}}{1-GC_{fb}}\right) V_s & -\frac{W_e G V_\delta}{1-GC_{fb}} \\ \frac{W_u H C_{fb} V_m}{1-GC_{fb}} & \frac{W_u C_{ff} V_s}{1-GC_{fb}} & -\frac{W_u G C_{fb} V_\delta}{1-GC_{fb}} \end{pmatrix} \begin{pmatrix} \hat{I}_{m*} \\ \hat{I}_{s*} \\ \hat{u}_\delta \end{pmatrix} \tag{5.21}$$

The criteria have been summarized in table 5.1.

criterion	description	Bound	transfer function
M_{11}	disturbance attenuation	$\frac{\gamma}{W_e V_m}$	$-\frac{H}{1-GC_{fb}}$
M_{12}	tracking	$\frac{\gamma}{W_e V_s}$	$1 - \frac{C_{ff}G}{1-GC_{fb}}$
M_{13}	uncertainty attenuation	$\frac{\gamma}{W_e V_\delta}$	$-\frac{W_e G V_\delta}{1-GC_{fb}}$
M_{21}	converter overflow due to I_{m*}	$\frac{\gamma}{W_u V_m}$	$\frac{HC_{fb}}{1-C_{fb}G}$
M_{22}	converter overflow due to I_{s*}	$\frac{\gamma}{W_u V_s}$	$\frac{C_{ff}}{1-GC_{fb}}$
M_{23}	model robustness	$\frac{\gamma}{W_u V_\delta}$	$\frac{GC_{fb}}{1-GC_{fb}}$

table 5.1

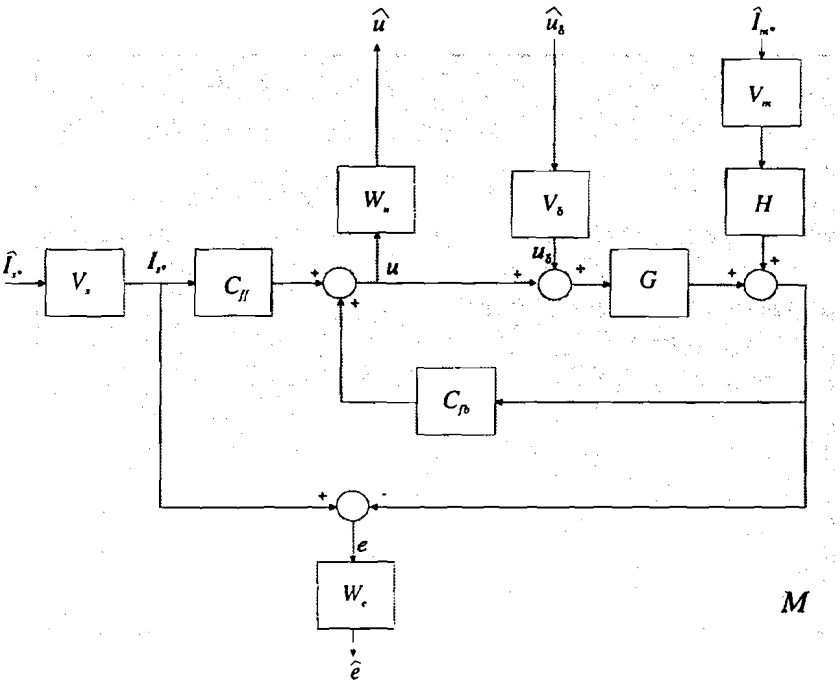

Figure 5.12: Control set up with weighting filters.

The factor γ represents the H_∞ bound and is supposed to satisfy $\gamma \leq 1$. A certain choice of the weighting filters will not always obtain a result that satisfies this demand. The scaling factor γ is therefore appended to matrix M.

A design procedure can be formulated which will result eventually in a set of weighting filters that guarantees robust stability and optimizes nominal performance. A trade off has to be made between the tracking bandwidth of the converter and the amplitude of the stator current that is to be supplied to the converter. The limiting factor is the output range of the voltage converter. On the one hand will a large tracking frequency range have to be paid for by a large voltage command signal which might violate the output range of the voltage converter. On the other hand will a large tracking bandwidth be possible when a small input signal is supplied to the converter.

5.3.1 Nominal performance

The transfer functions M_{11} (disturbance attenuation), M_{12} (tracking), M_{21} (converter overflow due to I_m^S) and M_{22} (converter overflow due to I_{s*}^S) determine the nominal performance. Our objective is to minimize the power of the output signals $z(t)$ by selecting a controller set (C_{fb}, C_{ff}) that meets this objective.

5.3.2 Robust stability

To this point we have discussed performance specifications for a stable feedback system. However, this feedback can be destabilized by means of the parameter deviations in G. The uncertainties form a loop with the dynamics of the nominal process which can destabilize the control

loop. Transfer function G describes actually only one transfer function from a set of possible transfer functions which can be described by

$$P_G = \{G(1 + W_G\Delta_0) | \|\Delta_0\|_\infty \leq 1\} \tag{5.22}$$

in which uncertainty weight W_G describes the uncertainty profile of the uncertainty as a function of the frequency and has been derived in section 5.1.

Robust stability can now be guaranteed when the following condition is satisfied

$$\left\| W_G \frac{GC_{fb}}{1 - C_{fb}G} \Delta_0 \right\|_\infty < 1 \tag{5.23}$$

Substitution of $\|\Delta_0\|_\infty \leq 1$ yields

$$\left\| W_G \frac{C_{fb}G}{1 - C_{fb}G} \right\|_\infty < 1 \tag{5.24}$$

or

$$\left\| \frac{C_{fb}G}{1 - C_{fb}G} \right\|_\infty < \frac{1}{|W_G|} \tag{5.25}$$

The uncertainty weight W_G is described by

$$W_G = -7.5\text{dB} = 0.42 \tag{5.26}$$

The uncertainty $W_G\Delta_0$ is connected with M via node u_Δ and y_Δ which means that the robust stability constraint from equation 5.24 can be incorporated as entry M_{23} in LFT matrix M which has been defined by equation 5.21. The bound that is expressed in equation 5.25 also puts a constraint on W_u and V_δ. Robust stability is guaranteed when

$$|W_u V_\delta| \geq |W_G| \tag{5.27}$$

This can be seen by combining equation 5.25 and 5.27.

5.3.3 Robust performance

Until sofar we only looked at nominal performance and robust stability individually. But what we are really looking for is that performance, imposed by the weights, and robust stability is guaranteed for a certain set of perturbations in process model G.

Robust performance can be guaranteed by

$$\left\| \begin{matrix} -\frac{W_e H V_m}{1-GC_{fb}} & W_e\left(1 - \frac{GC_{ff}}{1-GC_{fb}}\right)V_s & -\frac{W_e G V_\delta}{1-GC_{fb}} \\ \frac{W_u H C_{fb} V_m}{1-GC_{fb}} & \frac{W_u C_{ff} V_s}{1-GC_{fb}} & -\frac{W_u G C_{fb} V_\delta}{1-GC_{fb}} \end{matrix} \right\|_\infty < 1 \tag{5.28}$$

5.4 Design procedure

5.4.1 Design procedure

First of all we have to specify the type of input signals that will be used. Disturbance input I_m^S will have a constant amplitude and a bandwidth that is determined by the design procedure as will be shown later when we discuss the design steps. Input I_{s*}^S does not have a constant amplitude, but depends on the torque that is generated in the induction machine. The minimal stator current that is supplied to the induction machine equals I_m^S when no torque is generated and the maximum value of I_{s*}^S is determined by the converter and the induction machine that are used. The following limits have been defined.

input/output	description	symbol	range	bandwidth
input	desired stator current	I_{s*}^S	20-60 A	600 $\frac{\text{rad}}{\text{s}}$
	magnetizing current	I_m^S	20 A	determined in 'design step 2'
output	actual stator current	I_s^S	20-60 A	
	stator voltage	u	0-320 V	

table 5.2

The following design objectives are defined before we continue discussing the design steps.

- guaranteed stability in the presence of plant perturbations
- maximal tracking bandwidth ($M_{12} < -40$ dB).
- prevention of overflow ($M_{22} < 30$dB)
- disturbance attenuation
- robust performance

Design step 1 First, we will optimize the criteria M_{12} (tracking) and M_{22} (Converter overflow due to I_{s*}). We will show that both M_{12} and M_{22} are the limiting functions which means that these functions match the inverse weighting functions in a certain frequency range. This is done by ignoring the other inputs I_{m*} and u_δ for a moment by fixing V_m and V_δ to a very small value. The weighting filters W_e and W_u are to be designed in such a fashion that the maximum amplification factor of M_{22} is not violated and that scaling factor $\gamma \leq 1$.

Design step 2 Until sofar we ignored inputs I_{s*} and u_δ by fixing V_δ and V_m to a small value, which also means that M_{11}, M_{21}, M_{13} and M_{23} have been disregarded. This situation is altered in the second design step by defining shaping filter V_m as a low pass filter with a bandwidth that corresponds with the actual magnetizing current in the induction machine. V_m has to be scaled in such fashion that the following expression holds: $I_m = V_m \hat{I}_m$ with $\|\hat{I}_m\|_2 < 1$. We stated in section 5.1. that I_m^S remains more or less on the same magnitude. The other shaping filter V_δ is determined by the constraint in equation 5.27. Thus

$$|V_\delta| \geq |V_G||W_u|^{-1} \tag{5.29}$$

The smallest penalty is set on M_{23} when

$$|V_\delta| = |V_G||W_u|^{-1} \tag{5.30}$$

Addition of the filters V_δ and V_m to M will not likely lead to a solution with a scaling factor that satisfies $\gamma \leq 1$. There are two degrees of freedom at our disposal to lower scaling factor γ which are

- Reduce the bandwidth of V_m.
- Alter the weighting functions W_a or W_e. The passband of W_e can be reduced or the passband of W_a can be shifted to a higher frequency range.

5.4.2 Execution of the design steps

Design step 1 In this design step we will make focus on M_{12} and M_{22} which are described by

$$M_{12} = 1 - \frac{C_{ff}G}{1 - C_{fb}G} \tag{5.31}$$

and

$$M_{22} = \frac{C_{ff}}{1 - GC_{fb}} \tag{5.32}$$

both criteria are bounded by respectively $\frac{\gamma}{W_e V_e}$ and $\frac{\gamma}{W_u V_e}$. Shaping filter V_m and V_δ are defined as follows

$$V_m = 1.10^{-9} \tag{5.33}$$

and

$$V_\delta = 1.10^{-9} \tag{5.34}$$

Shaping filter V_s has the following transfer function

$$V_s = 60\frac{\frac{s}{10000} + 1}{\frac{s}{600} + 1} \tag{5.35}$$

This limits all allowable I_{s*} to a set of signals that are smaller than 60A with a bandwidth of 600 $\frac{rad}{s}$. This means that reference input $\hat{I}_{s*}^S$ (depicted in figure 5.12) remains in the unit ball of bounded power. The desired tracking properties can be translated in weighting filter W_e by putting a high penalty on the small frequencies and a low penalty on the high frequencies. Converter overflow is difficult to prevent, due to the fact that actuator overflow is a time phenomena, but is not likely to occur when we put a high penalty on the high frequencies and a low penalty on the small frequencies. A trade off is now made between M_{12} and M_{22} when the design objectives with respect to these two criteria are

- The maximum allowable value of M_{22} is set on 30 dB.
- The tracking bandwidth determined by M_{12} is to be maximized.

The slope of high pass filter W_u has been chosen in such a way that the maximum amplification factor of M_{22}, set on 30dB, has not been violated. W_u is expressed as

$$W_u = \frac{2.528s^2 + 3666s + 1.327.10^6}{s^2 + 1.45.10^5 s + 5.29.10^9} \tag{5.36}$$

and depicted in figure 5.13 The maximum value of M_{22} is also dependent on filter W_e. This filter is now chosen in such a way that the tracking bandwidth of M_{12} is maximized, the maximum value of M_{22} does not exceed 30dB and scaling factor $\gamma < 1$. This lead to the low pass filter W_e that has been depicted in figure 5.13 and can be described by

$$W_e = \frac{2.931.10^{10}}{s^4 + 535s^3 + 1.071.10^5 s^2 + 9.521.10^6 s + 3.167.10^8} \tag{5.37}$$

Shifting the positive slope of W_u and the negative slope of W_e to the left would result in a smaller maximum value of M_{22} and a detoriating disturbance attenuation plot, since u is weighted more and e is weighted less. The magnitude plots of all criteria with the inverse weighting functions

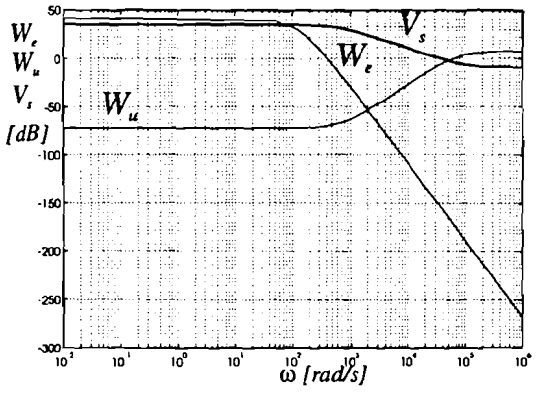

Figure 5.13: Shaping filters and weighting filters after the first design step.

(dashed) have been plotted in figure 5.14 and 5.15. It can be seen that M_{12} is the limiting function up to 1000 $\frac{rad}{s}$ and M_{12} from $10.10^3 \frac{rad}{s}$ to $40.10^3 \frac{rad}{s}$

The other criteria M_{11}, M_{21}, M_{13} and M_{23} which are partially bounded by V_δ and V_m have not been depicted because they do not give any additional information since V_δ and V_m were set on a small value.

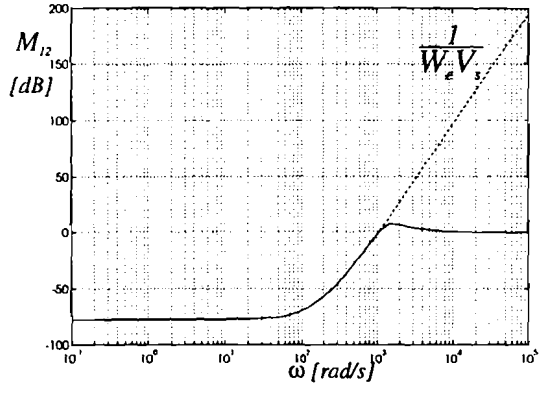

Figure 5.14: Tracking M_{12}

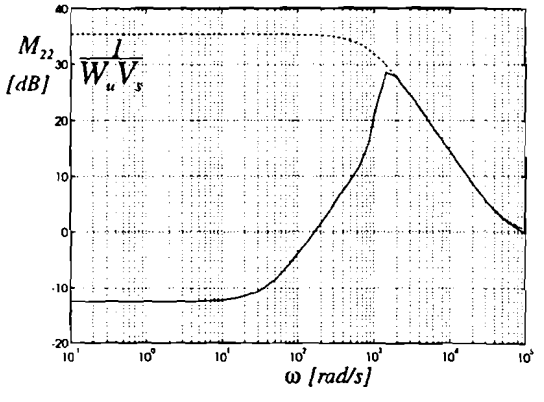

Figure 5.15: Converter overflow due to I^S_{s*} M_{22}

The second design step The control loop is supposed to be stable in the face of plant perturbations in G. Robust stability is therefore a constraint that should not be violated and can be adjusted, according to 5.29, by means of shaping filter V_δ and weighting filter W_u and is determined by

$$|V_\delta| = |W_G||W_u|^{-1} \tag{5.38}$$

where W_u has already been designed during the first step and W_G is the uncertainty profile that is describe by equation 5.26. Thus V_δ has the following transfer function

$$V_\delta = \frac{0.1662s^2 + 2.409s + 8.72.10^8}{s^2 + 1450s + 5.25.10^5} \tag{5.39}$$

and is depicted in figure 5.16. The remaining shaping filter V_m is a low pass filter with a break off frequency that is to be chosen so that the scaling factor γ does not exceed one. Another method that could be applied is adjustment of weighting filters W_e and W_u. This would however have to be payed for by a γ that is higher than one or violation of the design objectives that we stated.

We can see by looking at the magnitude plots in figure 5.14 that an acceptable tracking can be achieved when $\omega \leq 350\frac{rad}{s}$. We will first check if γ remains smaller than one when V_m has a bandwidth that is higher than 350 $\frac{rad}{s}$. V_m is defined as

$$V_m = \frac{0.0025.10^2s^2 + 162.5s + 2.625.10^6}{s^2 + 650s + 1.05.10^5} \tag{5.40}$$

and has been depicted in figure 5.16. The break off angular frequency of V_m is supposed to be higher than 350 $\frac{rad}{s}$ because this is also the angular frequency at which the tracking properties are satisfactory. Implementation of a shaping filter with a bandwidth of 350 $\frac{rad}{s}$ resulted however in a scaling factor γ that is higher than one. We now have two degrees of freedom at our disposal, as has been stated in section 5.4.1, to lower scaling factor γ. We could either shift the break off frequency of V_m to a smaller value or alter weighting filter W_e or W_a. A choice has been made to alter W_e to

$$W_e = \frac{3.664.10^{10}}{s^4 + 535s^3 + 1.071.10^5s^2 + 9.521.10^6s + 3.167.10^8} \tag{5.41}$$

which has been depicted in figure 5.17. The amplification factor of W_e that was found in design step 1 is changed from $2.931.10^{10}$ to $3.664.10^{10}$. This choice of W_e results in a scaling factor γ that equals one.

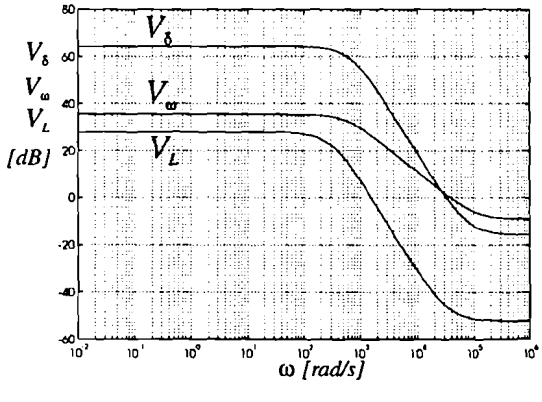

Figure 5.16: Shaping filters V_s, V_m and V_δ

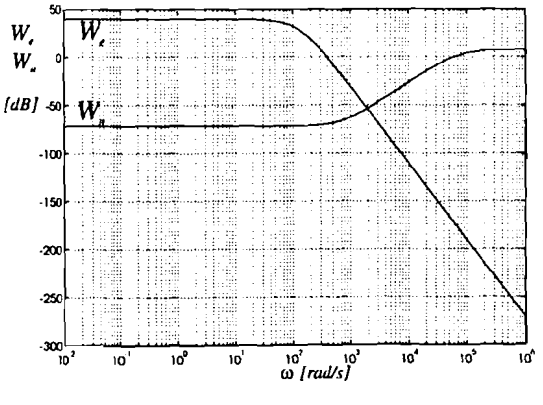

Figure 5.17: Weighting filters W_e and W_u

The magnitude plots of all entries in matrix M i.e. M_{11} to M_{23} have been depicted in figure 5.18 to 5.23. It can be seen that M_{12} and M_{22} did not change when we compare them to the results from the first design step. The tracking bandwidth remains therefore on $350\frac{\text{rad}}{\text{s}}$. The disturbance attenuation plot shows that the influence from I_m on e is acceptable in the bandwidth that we consider.

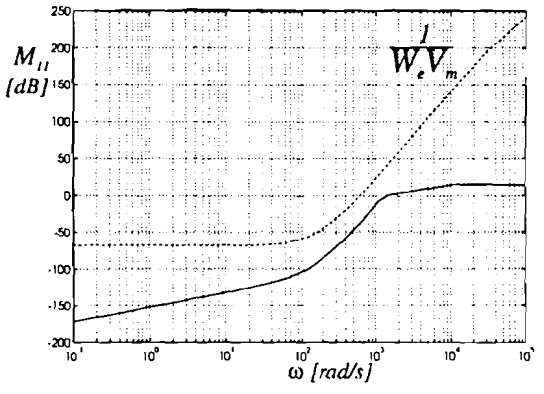

Figure 5.18: Disturbance attenuation M_{11}

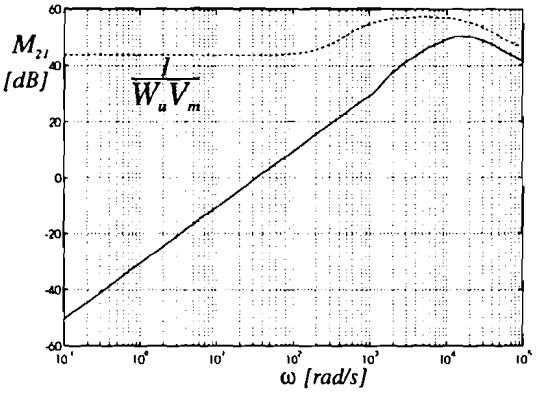

Figure 5.19: Converter overflow due to I_{m*} M_{21}

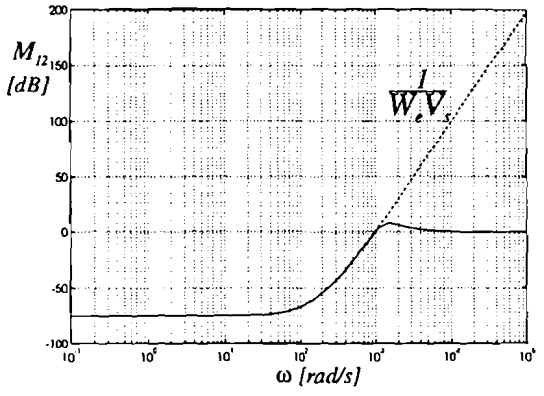

Figure 5.20: Tracking M_{12}

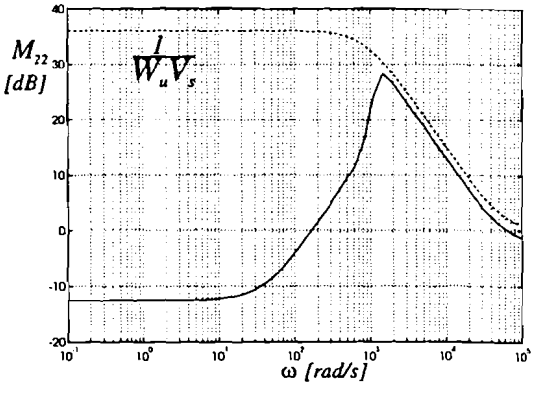

Figure 5.21: Converter overflow due to I_{s*} M_{22}

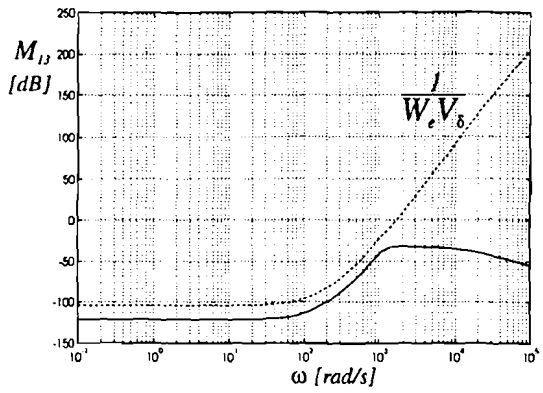

Figure 5.22: Uncertainty attenuation M_{13}

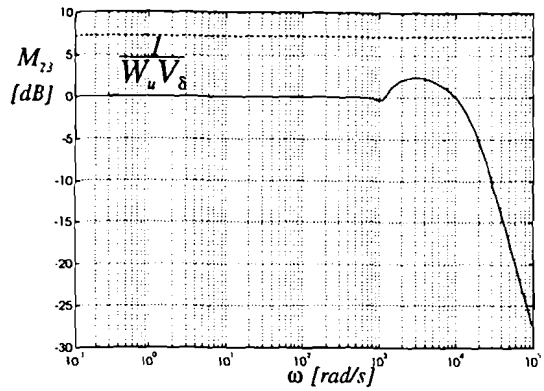

Figure 5.23: Model robustness M_{23}

The feed forward controller C_{ff} and C_{fb} have been depicted in figure 5.24 and 5.25. C_{ff} and C_{fb} were both initially a thirteenth order controller but could be reduced to an eleventh order controller.

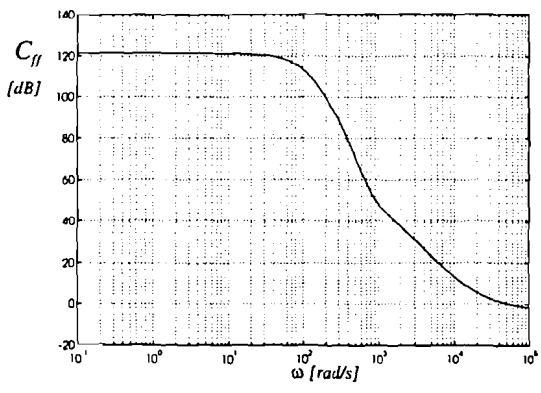

Figure 5.24: Controller C_{ff}

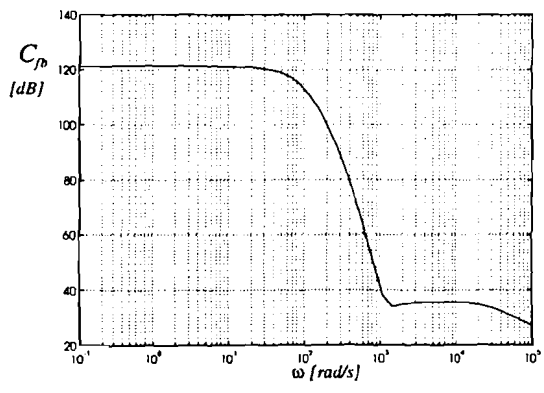

Figure 5.25: Controller C_{fb}

The following poles and zeros have been found for C_{ff}. Asterix * denotes the fact a pole zero cancellation takes place. (Static gain $C_{ff} = 2.228.10^5$)

zeros	poles
$-7.5.10^4$	$-2.44.10^5$
-7.10^4	-1.10^5
$-2.91.10^4$	$-3.09.10^4 \pm 1.36.10^4 i$
$-1.55.10^4 \pm 1.26.10^4 i$	-748.35
$-3.42.10^2 \pm 8.22.10^2 i$	-701.48
$-8.52.10^2 \pm 2.97.10^2 i$	-249.2
-252.07	-200.64
-198.19	169.52
-41*	$-1.30.10^2 \pm 2.89.10^1 i$
	-104.93
	-41*

Table 5.4

The same has been done for the feedback controller C_{fb} (Static gain $C_{fb} = -4.2116.10^6$).

zeros	poles
-1.10^5*	$-2.44.10^5$
$-7.5.10^4$	-1.10^5*
-7.10^4	$-3.09.10^4 \pm 1.36.10^4 i$
$-3.06.10^2 \pm 1.24.10^3 i$	-748.35
$-1.25.10^3 \pm 3.00.10^2 i$	-701.48
$-8.96.10^2 \pm 8.50.10^2 i$	-249.2
-252.07	-200.64
-198.19	169.52
-41*	$-1.30.10^2 \pm 2.89.10^1 i$
	-104.93
	-41*

Table 5.5

5.5 Simulations

Simulations have been carried out for the frequency range to $350\frac{rad}{s}$. The results have been depicted in figure G.1 to G.6. Two cases have been simulated

- There are no perturbations in R_s, L_σ and L_m. The output signals e and u have been plotted in figure G.3 and G.4 in appendix G.
- There are perturbations in R_s and L_σ ($\delta_{R_s} = 0.3$ and $\delta_{L_\sigma} = 0.3$). Error signal e and converter command signal u are depicted in figure G.5 and G.6 in appendix G.

Comparison of the responses shows that the maximum value of the error signal is in both cases 0.23. Only the actuator signal is bigger when the perturbations are $\delta_{R_s} = 0.3$ and $\delta_{L_\sigma} = 0.3$. Other perturbation ($\delta_{R_s} = -0.3$ and $\delta_{L_\sigma} = -0.3$), which have not been depicted, showed an even lower actuator signal. The error signal had also in this case a maximum value of 0.23. The relative error between I_{s*} and e is 0.38%. This is still smaller than the -40dB(=1%) we demanded.

Chapter 6

Conclusion and recommendation

6.1 Conclusion

- It is possible to describe a concatenated indirect field oriented controller and an induction machine by means of a linear equation with a nonlinear error model. This nonlinear error model inhabits the cross dependencies between the input signals I_{m*} and T_{e*} on the one hand and output signals I_m and T_e on the other hand. The nonlinear equations are characterized by means of a parameter deviation between the indirect field oriented controller and the induction machine.

- The steady state error between the actual torque and the desired torque has a nonlinear relation with the desired torque. An equation has been derived which describes this relation.

- A distinction has to be made between the rotor time constant τ_r and the magnetizing inductance L_m. A deviation between the actual rotor time constant and the identified rotor time constant results in a transient behaviour of the internal variables such as the slip frequency, the torque angle and the magnetizing current. An error between the actual magnetizing inductance in the machine and the identified magnetizing inductance in the indirect field oriented controller only results in a static error between the actual torque and the desired torque.

- A controller has been designed that attenuates the influence from the load torque on the angular velocity of the rotor axis and remains stable in the face of perturbations. It is not possible to develop a fast tracking system, since this would require a much larger actuator input range.

- The controller that has been designed is probably too conservative. This is caused by the fact that no use is made of the structure of the nonlinear error model. It appeared that a PI controller which violated the stability constraint resulted in a stable closed loop system. The disturbance attenuation properties from this PI controller are much better than disturbance attenuation properties from the H_∞ controller.

- The nonlinear error model has been incorporated in a H_∞ setting by bounding the harmonics that occur by means of an overall uncertainty filter. This overall uncertainty filter has

been obtained by computing an uncertainty filter for several perturbations. All uncertainty filters that have been obtained are bounded by this overall uncertainty filter.

- The controller is designed in two design steps. The model robustness criterion and the disturbance attenuation criterion have been optimized first by selecting appropriate shaping filters and weighting filters. The shaping filters that do not influence the model robustness criterion and the disturbance attenuation criterion directly are set on a small value in this first design step. The remaining shaping filters are composed in the second design step in such a fashion that robust performance is obtained which means that the H_∞-norm of the generalized system is smaller than one.

- The input circuit of an induction machine can be modelled by a first order transfer function with an additive disturbance input. The magnetizing current is the disturbance input.

- A controller has been designed that enables us to manipulate the reference nodes of the voltage converter in such a fashion that the current in the stator windings follows a reference stator current instantaneously. Use is made of a first order model with an additive noise filter. The objective of the control design process is to attenuate the influence of the magnetizing current on the stator current. The tracking bandwidth of the control loop is limited by the output range of the voltage converter. A small error between the actual stator current and the desired stator current has to be paid for by a large actuator signal.

6.2 Recommendations

- The developed controller for the outer loop should be implemented in a practical set up.

- The developed controllers that convert a voltage converter to a current converter should be applied on an actual converter.

- The controllers that are used to manipulate the reference side of a voltage converter can be improved by applying μ-synthesis because then use is made of the structure of the nonlinear error model.

Appendix A

Machine parameters

Heemaf EM 3008; SKA-machine nr. 552047; Type NK 58-6

ΔY 220/380 V	41.5/24 A
11 kW/15 pk	$\cos\xi_f$=0.83
rated speed	950 rpm
rated slip	5 %
rated frequency	50 Hz
number of pole pairs	3
$T_{e,max}$	100 Nm

parameter	value
L_m	29.6 mH
L_σ	5.8 mH
R_r	0.1637 Ω
R_s	0.238 Ω

Appendix B

Derivation of steady state equation

B.1 Derivation of the steady state equation by using the results from section 3.2

Substitution of

$$I_m = \sqrt{\frac{I_{qs*}^2 + I_{m*}^2}{1 + \left(\frac{\tau_r I_{qs*}}{\tau_r^* I_{m*}}\right)^2}} \tag{B.1}$$

and

$$I_{qs} = \sqrt{\frac{\left(\frac{\tau_r I_{qs*}}{\tau_r^* I_{m*}}\right)(I_{qs*}^2 + I_{m*}^2)}{1 + \left(\frac{\tau_r I_{qs*}}{\tau_r^* I_{m*}}\right)^2}} \tag{B.2}$$

in

$$\delta T_e = L_m I_m I_{qs} - L_m^* I_{m*} I_{qs*} \tag{B.3}$$

yields with $\tau_r = \tau_r^*(1 + \delta_{\tau_r})$

$$\delta T_e = L_m \frac{(I_{qs*}^2 + I_{m*}^2)\left(\frac{\tau_r I_{qs*}}{\tau_r^* I_{m*}}\right)}{1 + \left(\frac{\tau_r I_{qs*}}{\tau_r^* I_{m*}}\right)^2} - L_m^* I_{m*} I_{qs*} \tag{B.4}$$

$$= \frac{L_m(1 + \delta_{\tau_r})\left(I_{m*} I_{qs*} + \frac{I_{qs*}^3}{I_{m*}}\right) - L_m^* I_{m*} I_{qs*}\left(1 + \left((1 + \delta_{\tau_r})\frac{I_{qs*}}{I_{m*}}\right)^2\right)}{1 + \left((1 + \delta_{\tau_r})\frac{I_{qs*}}{I_{m*}}\right)^2} \tag{B.5}$$

$$= \frac{I_{m*} I_{qs*}(L_m - L_m^*) + L_m \delta_{\tau_r} I_{m*} I_{qs*} + L_m I_{qs*} I_{m*}\left((1 + \delta_{\tau_r})\left(\frac{I_{qs*}}{I_{m*}}\right)^2\right)}{1 + \left((1 + \delta_{\tau_r})\frac{I_{qs*}}{I_{m*}}\right)^2} + \tag{B.6}$$

$$- \frac{L_m^* I_{m*} I_{qs*}\left((1 + \delta_{\tau_r})^2\left(\frac{I_{qs*}}{I_{m*}}\right)^2\right)}{1 + \left((1 + \delta_{\tau_r})\frac{I_{qs*}}{I_{m*}}\right)^2} \tag{B.7}$$

$$= L_m^* I_{m*} I_{qs*} \frac{\delta_{L_m} + \delta_{\tau_r}(1+\delta_{L_m}) + ((1+\delta_{L_m})(1+\delta_{\tau_r}) - (1+\delta_{\tau_r})^2)\left(\frac{I_{qs*}}{I_{m*}}\right)^2}{1+\left((1+\delta_{\tau_r})\frac{I_{qs*}}{I_{m*}}\right)^2} \tag{B.8}$$

$$= T_{e*} \frac{\delta_{L_m} + \delta_{\tau_r}(1+\delta_{L_m}) + (\delta_{L_m} - \delta_{\tau_r})(1+\delta_{\tau_r})\left(\frac{T_{e*}}{L_m^* I_{m*}^2}\right)^2}{1+(1+\delta_{\tau_r})^2\left(\frac{T_{e*}}{L_m^* I_{m*}^2}\right)^2} \tag{B.9}$$

B.2 Derivation of steady state equation from the nonlinear error model

The following two steady state expression for ΔI_{ma} and I_{mb} have been derived

$$\Delta I_{ma} = \frac{\delta_{\tau_r}\tau_r \frac{I_{qs*}^2}{\tau_r^* I_{m*}}}{1+\frac{\tau_r I_{qs*}}{\tau_r^* I_{m*}}} \tag{B.10}$$

$$I_{mb} = -\frac{\delta_{\tau_r} I_{qs*}}{1+\frac{\tau_r I_{qs*}}{\tau_r^* I_{m*}}} \tag{B.11}$$

These two equations can be substituted in

$$\delta T_e = L_m(-I_{mb} I_{m*} + (I_{m*} - \Delta I_{ma}) I_{qs*}) - L_m^* I_{m*} I_{qs*} \tag{B.12}$$

with

$$I_{m*} - \Delta I_m = I_{m*} - \frac{\delta_{\tau_r}(1+\delta_{\tau_r})\frac{I_{qs*}^2}{I_{m*}}}{1+\frac{\tau_r I_{qs*}}{\tau_r^* I_{m*}}} \tag{B.13}$$

$$= \frac{I_{m*} + \frac{I_{qs*}^2}{I_{m*}}(1+\delta_{\tau_r})}{1+\left((1+\delta_{\tau_r})\frac{I_{qs*}}{I_{m*}}\right)^2} \tag{B.14}$$

yields

$$\delta T_e = L_m\left(\frac{\delta_{\tau_r} I_{qs*} I_{m*} + I_{m*} I_{qs*} + \frac{I_{qs*}^3}{I_{m*}}(1+\delta_{\tau_r})}{1+\left((1+\delta_{\tau_r})\frac{I_{qs*}}{I_{m*}}\right)^2}\right) - L_m^* I_{m*} I_{qs*} \tag{B.15}$$

$$= \frac{L_m(1+\delta_{\tau_r})(I_{m*} I_{qs*} + \frac{I_{qs*}^3}{I_{m*}}) - L_m^* I_{m*} I_{qs*}\left(1+\left((1+\delta_{\tau_r})\frac{I_{qs*}}{I_{m*}}\right)^2\right)}{1+\left((1+\delta_{\tau_r})\frac{I_{qs*}}{I_{m*}}\right)^2} \tag{B.16}$$

$$= \frac{I_{m*} I_{qs*}(L_m - L_m^*) + L_m \delta_{\tau_r} I_{m*} I_{qs*} + L_m I_{qs*} I_{m*}(1+\delta_{\tau_r})\frac{I_{qs*}^2}{I_{m*}^2}}{1+\left((1+\delta_{\tau_r})^2\frac{I_{qs*}}{I_{m*}}\right)^2} +$$

$$-\frac{L_m^* I_{m*} I_{qs*}(1+\delta_{\tau_r})^2\frac{I_{qs*}^2}{I_{m*}^2}}{1+\left((1+\delta_{\tau_r})\frac{I_{qs*}}{I_{m*}}\right)^2} \tag{B.17}$$

and substitution of

$$L_m = L_m^*(1+\delta_{L_m}) \tag{B.18}$$

leads to

$$\delta T_e = I_{m*} I_{qs*} \left(\frac{L_m^* \delta_{L_m} + L_m^*(1+\delta_{L_m})\delta_{\tau_r} + L_m^*(1+\delta_{\tau_r})(1+\delta_{L_m})\frac{I_{qs*}^2}{I_{m*}^2}}{1+\left((1+\delta_{\tau_r})\frac{I_{qs*}}{I_{m*}}\right)^2} + \right.$$

$$\left. - \frac{L_m^* I_{m*} I_{qs*}(1+\delta_{\tau_r})^2 \frac{I_{qs*}^2}{I_{m*}^2}}{1+\left((1+\delta_{\tau_r})\frac{I_{qs*}}{I_{m*}}\right)^2} \right) \tag{B.19}$$

$$= L_m^* I_{m*} I_{qs*} \left(\frac{\delta_{L_m} + (1+\delta_{L_m})\delta_{\tau_r} + ((1+\delta_{\tau_r})(1+\delta_{L_m}) - (1+\delta_{\tau_r})^2)\frac{I_{qs*}^2}{I_{m*}^2}}{1+\left((1+\delta_{\tau_r})\frac{I_{qs*}}{I_{m*}}\right)^2} \right) \tag{B.20}$$

$$= L_m^* I_{m*} I_{qs*} \frac{\delta_{L_m} + (1+\delta_{L_m})\delta_{\tau_r} + (\delta_{L_m} + \delta_{\tau_r} + \delta_{\tau_r}\delta_{L_m} - 2\delta_{\tau_r} - \delta_{\tau_r}^2)\frac{I_{qs*}^2}{I_{m*}^2}}{1+\left((1+\delta_{\tau_r})\frac{I_{qs*}}{I_{m*}}\right)^2} \tag{B.21}$$

$$= L_m^* I_{m*} I_{qs*} \frac{\delta_{L_m} + \delta_{\tau_r}(1+\delta_{L_m}) + (\delta_{L_m} - \delta_{\tau_r})(1+\delta_{\tau_r})\left(\frac{I_{qs*}}{I_{m*}}\right)^2}{1+\left((1+\delta_{\tau_r})\frac{I_{qs*}}{I_{m*}}\right)^2} \tag{B.22}$$

$$= T_{e*} \frac{\delta_{L_m} + \delta_{\tau_r}(1+\delta_{L_m}) + (\delta_{L_m} - \delta_{\tau_r})(1+\delta_{\tau_r})\left(\frac{T_{e*}}{L_m^* I_{m*}^2}\right)^2}{1+(1+\delta_{\tau_r})^2\left(\frac{T_{e*}}{L_m^* I_{m*}^2}\right)^2} \tag{B.23}$$

The steady state description of equation is identical to the results that was obtained in equation B.9.

Appendix C

Simulation results error model

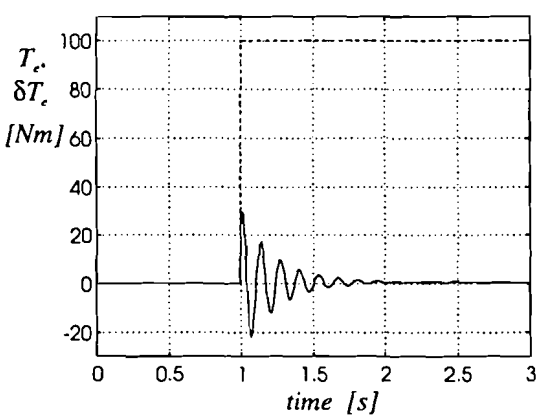

Figure C.1: Stepresponse when $\delta_{L_m} = 0.3$ *and* $\delta_{\tau_r} = 0.3$ *with* T_{e*} *dashed*

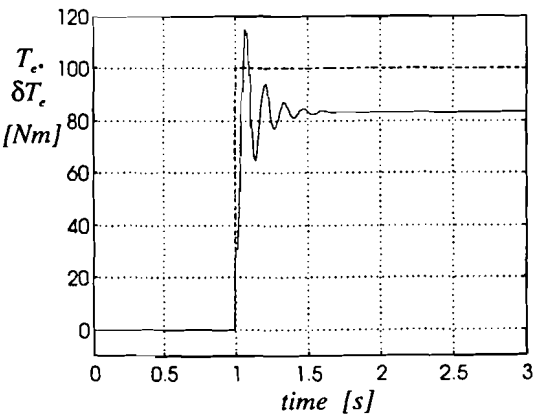

Figure C.2: Stepresponse when $\delta_{L_m} = 0.3$ *and* $\delta_{\tau_r} = -0.3$ *with* T_{e*} *dashed*

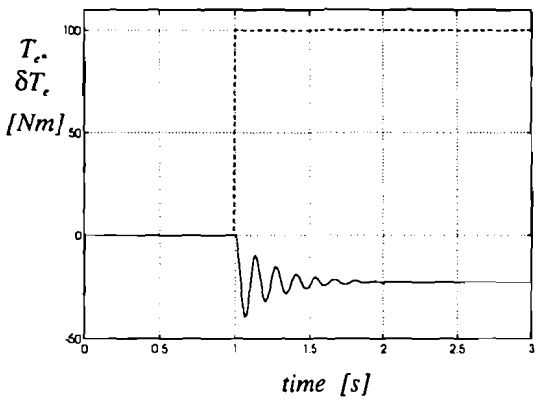

Figure C.3: Stepresponse when $\delta_{L_m} = 0$ *and* $\delta_{\tau_r} = 0.3$ *with* T_{e*} *dashed*

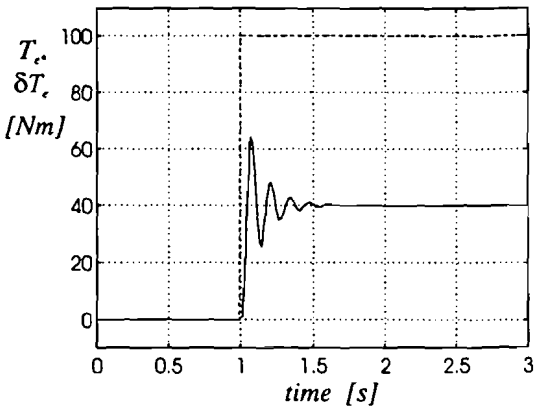

Figure C.4: Stepresponse when $\delta_{L_m} = 0.3$ *and* $\delta_{\tau_r} = 0.3$ *with* T_{e*} *dashed*

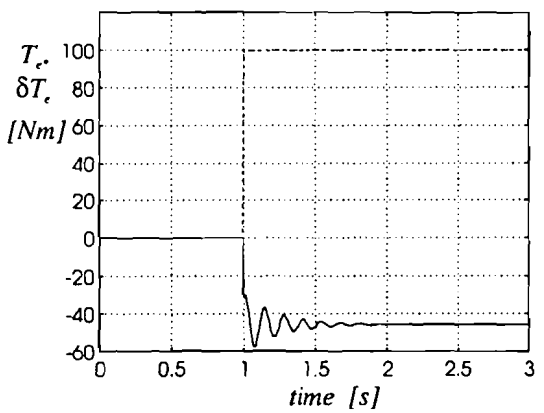

Figure C.5: stepresponse when $\delta_{L_m} = -0.3$ *and* $\delta_{\tau_r} = 0.3$ *with* T_{e*} *dashed*

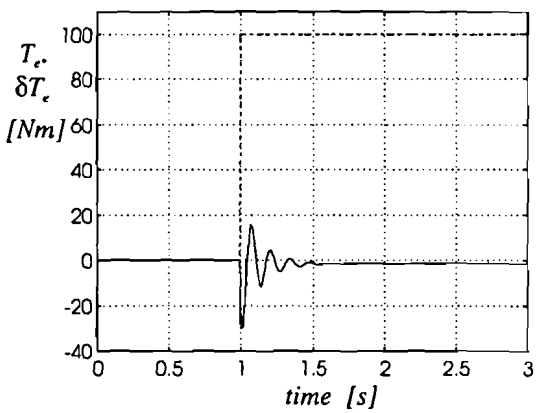

Figure C.6: Stepresponse when $\delta_{L_m} = -0.3$ *and* $\delta_{\tau_r} = -0.3$ *with* T_{e*} *dashed*

Appendix D

Stepresponse plots

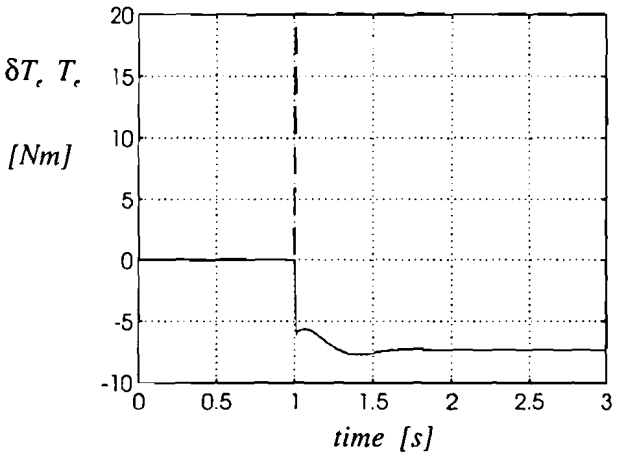

Figure D.1: Stepresponse of error model when $\delta_{\tau_r} = 0.3$ and $\delta_{L_m} = -0.3$. (T_{e*} is dashed line)

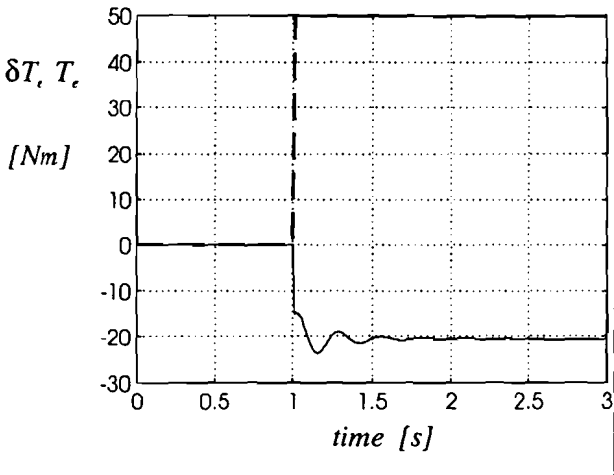

Figure D.2: Stepresponse of error model when $\delta_{\tau_r} = 0.3$ and $\delta_{L_m} = -0.3$. (T_{e*} is dashed line)

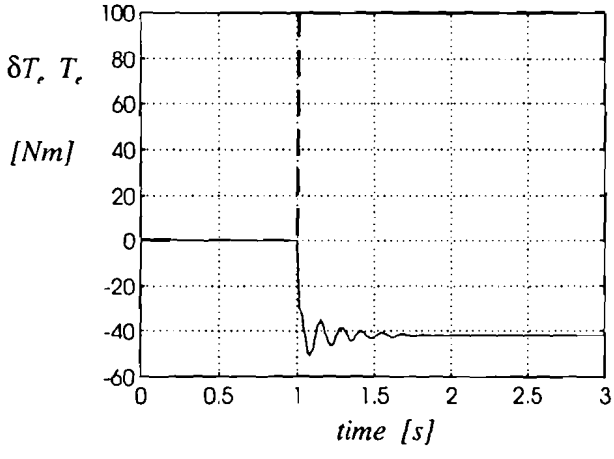

Figure D.3: Stepresponse of error model when $\delta_{\tau_r} = 0.3$ and $\delta_{L_m} = -0.3$. (T_{e*} is dashed line)

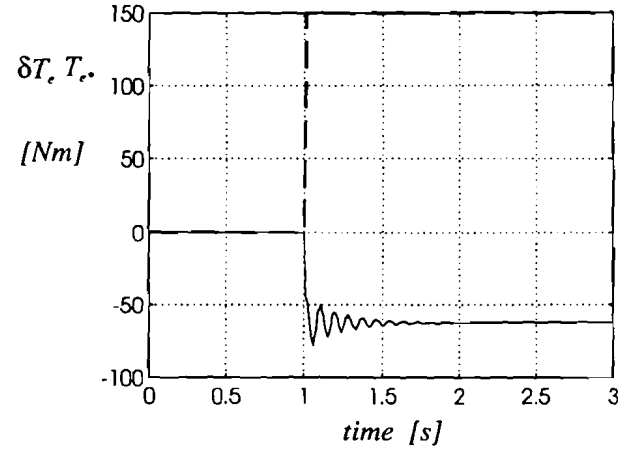

Figure D.4: Stepresponse of error model when $\delta_{\tau_r} = 0.3$ and $\delta_{L_m} = -0.3$. (T_{e*} is dashed line)

Appendix E

Uncertainty filter

E.1 $\delta_{L_m} = 0.3$ and $\delta_{T_r} = 0.3$

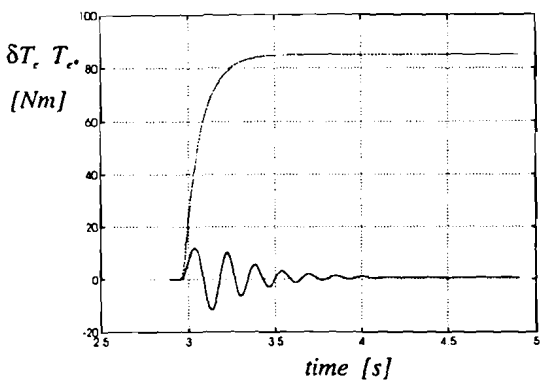

Figure E.1: T_{e*} and δT_e

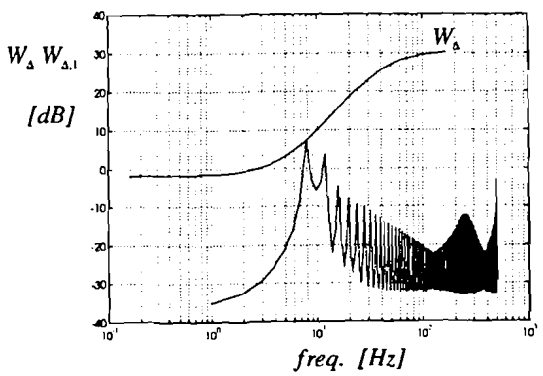

Figure E.2: $W_{\Delta,1}$

E.2 $\delta_{L_m} = 0.3$ and $\delta_{\tau_r} = -0.3$

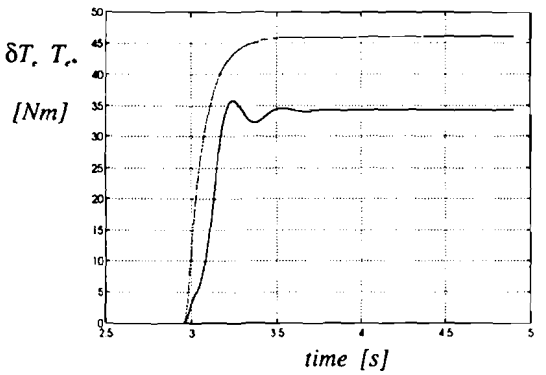

Figure E.3: T_{e*} and δT_e

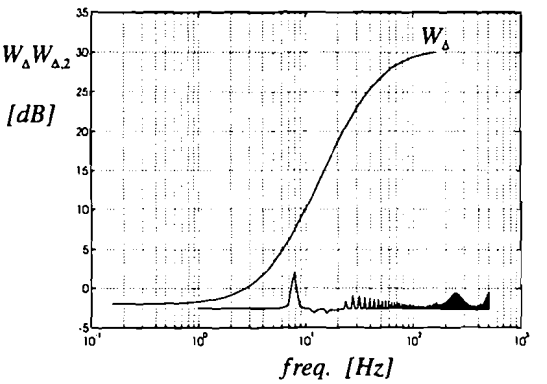

Figure E.4: $W_{\Delta,2}$

E.3 $\delta_{L_m} = 0$ and $\delta_{\tau_r} = 0.3$

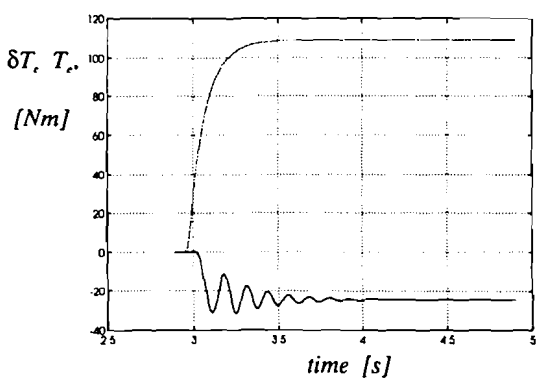

Figure E.5: T_{e*} and δT_e

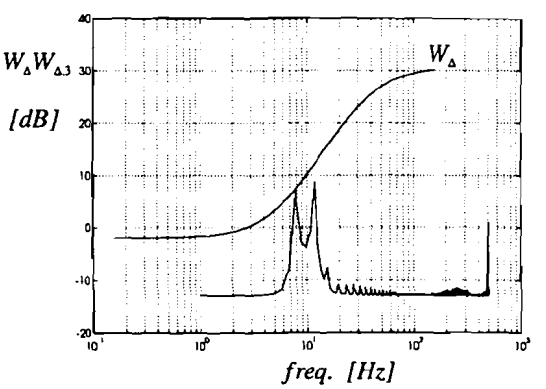

Figure E.6: $W_{\Delta,3}$

E.4 $\delta_{L_m} = 0$ and $\delta_{\tau_r} = -0.3$

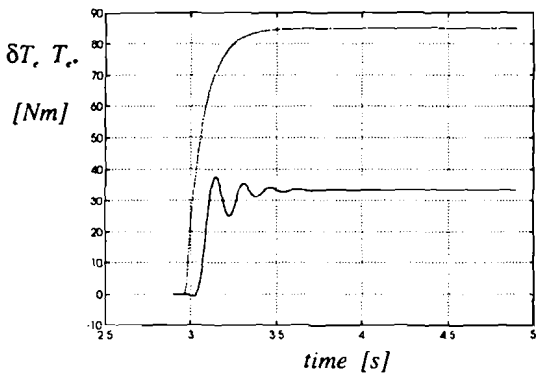

Figure E.7: T_{e*} and δT_e

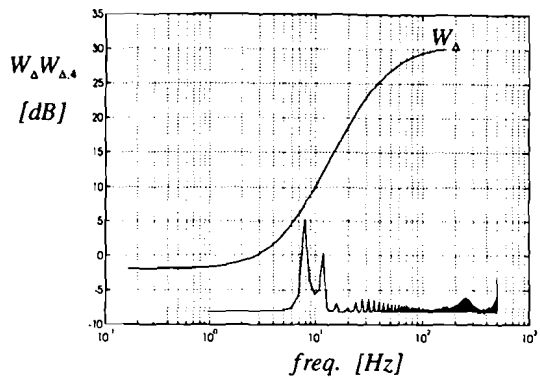

Figure E.8: $W_{\Delta,4}$

E.5 $\delta_{L_m} = -0.3$ and $\delta_{\tau_r} = 0.3$

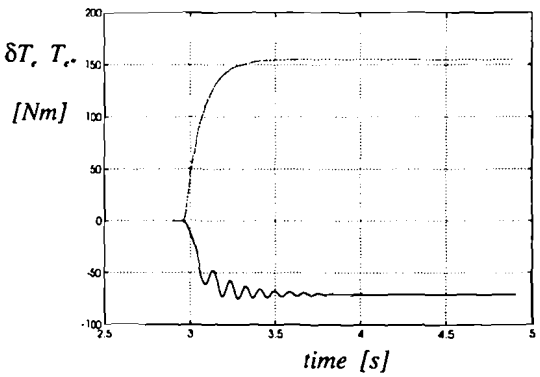

Figure E.9: T_{e*} and δT_e

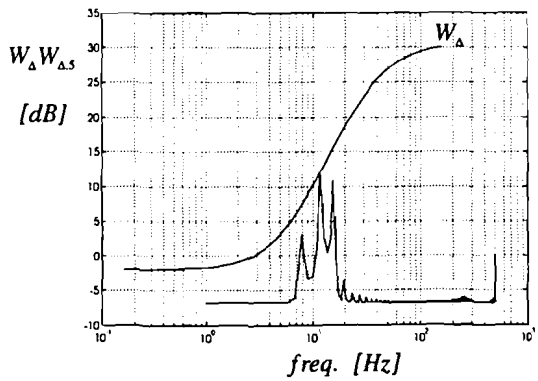

Figure E.10: $W_{\Delta,5}$

E.6 $\delta_{L_m} = -0.3$ and $\delta_{T_r} = -0.3$

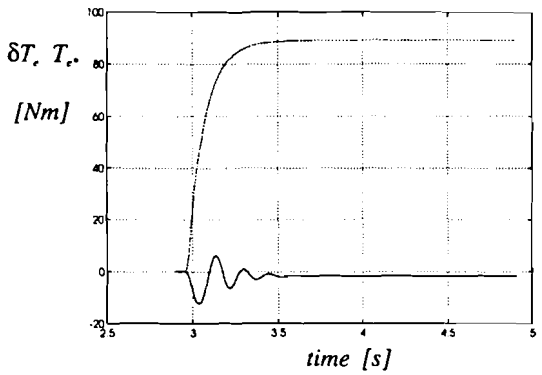

Figure E.11: T_{e*} and δT_e

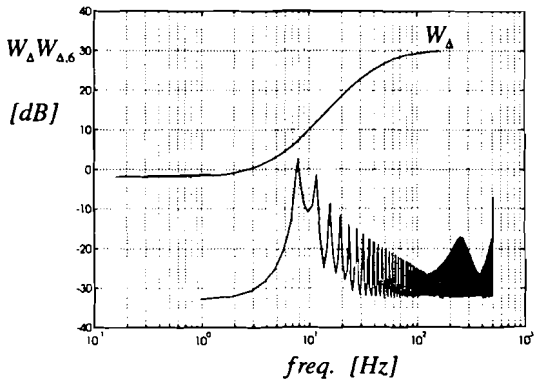

Figure E.12: $W_{\Delta,6}$

Appendix F

Simulation results of the control loop

F.1 Simulation results when $\delta_{T_r} = -0.3$, $\delta_{L_m} = -0.3$ and T_L has a bandwidth of 20 $\frac{rad}{s}$

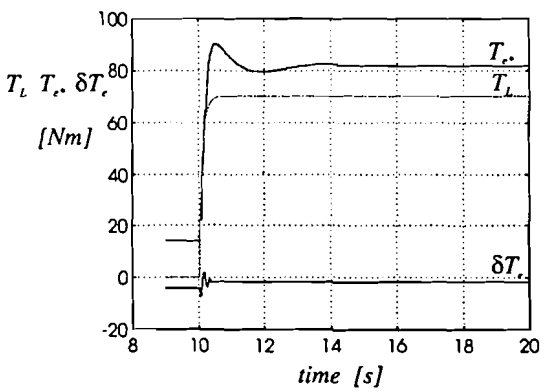

Figure F.1: T_L, δ_{T_e} and T_{e*}

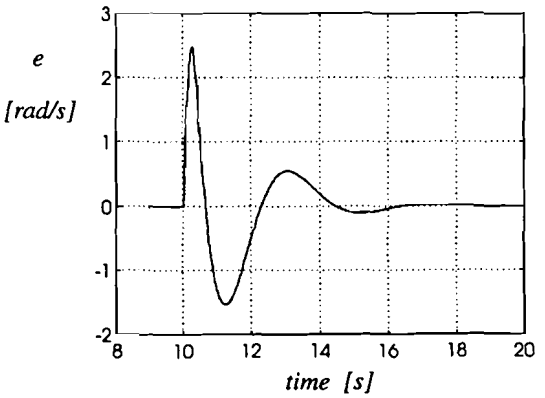

Figure F.2: error between ω_m and ω_{m*}

F.2 Simulation results when $\delta_{\tau_r} = 0.3$, $\delta_{L_m} = -0.3$ and T_L has a bandwidth of 20 $\frac{rad}{s}$

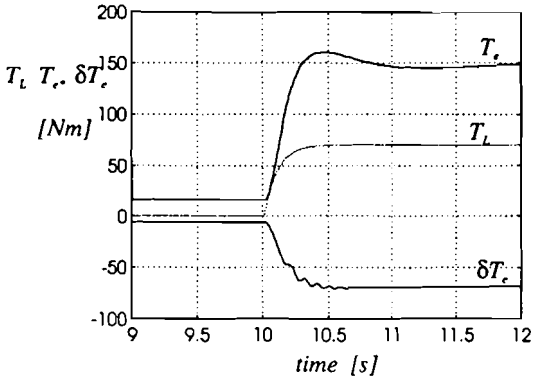

Figure F.3: T_L, δ_{T_e} and T_{e*}

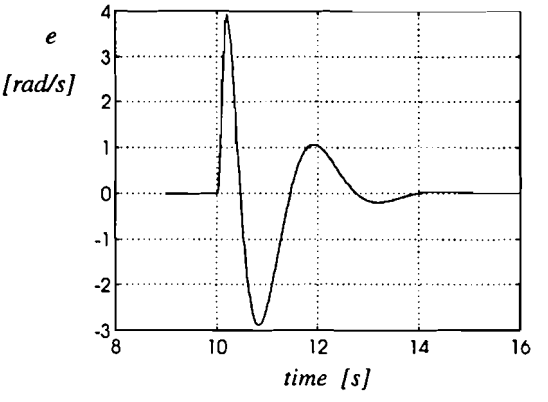

Figure F.4: error between ω_m and ω_{m*}

F.3 Simulation results when $\delta_{\tau_r} = 0.3$, $\delta_{L_m} = -0.3$ and T_L has a bandwidth of 1 $\frac{rad}{s}$

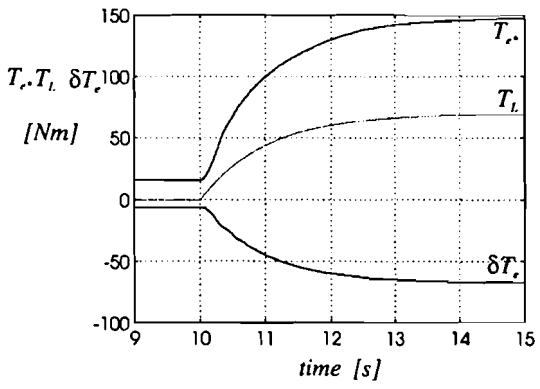

Figure F.5: T_L, δ_{T_e} and T_{e*}

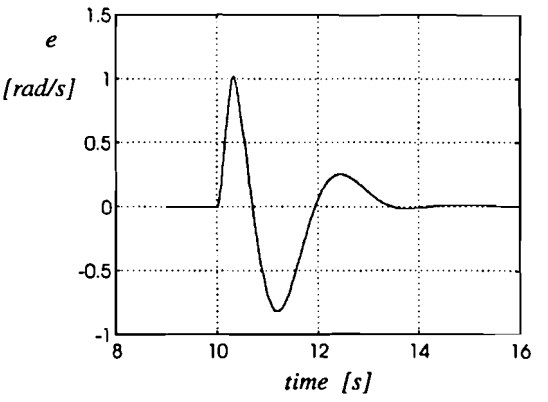

Figure F.6: error between ω_m and ω_{m*}

F.4 Simulation results when $\delta_{\tau_r} = -0.3$, $\delta_{L_m} = -0.3$ and T_L has a bandwidth of $20\frac{rad}{s}$

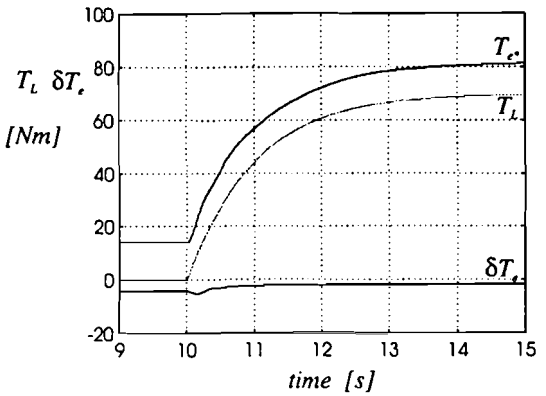

Figure F.7: T_L, δ_{T_e} and T_{e*}

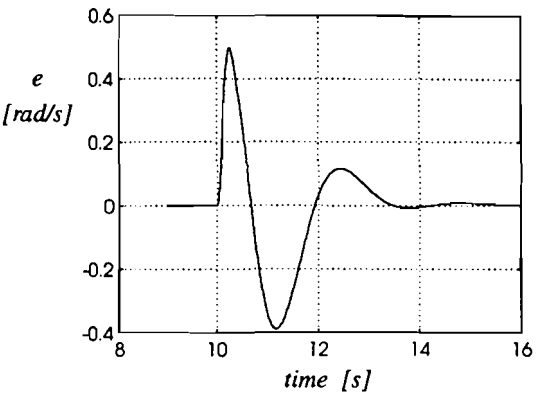

Figure F.8: error between ω_m and ω_{m*}

F.5 Simulation results when $\delta_{\tau_r} = 0$, $\delta_{L_m} = 0$ and T_L has a bandwidth of $20\frac{rad}{s}$

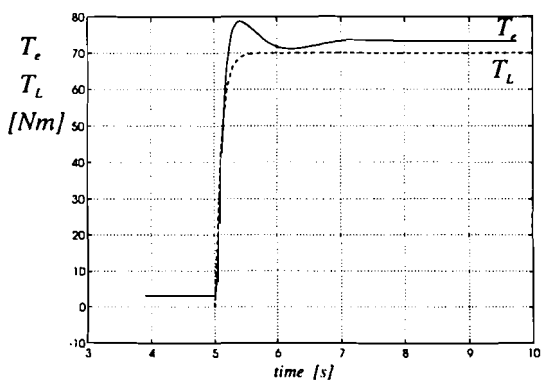

Figure F.9: T_L and T_{e*}

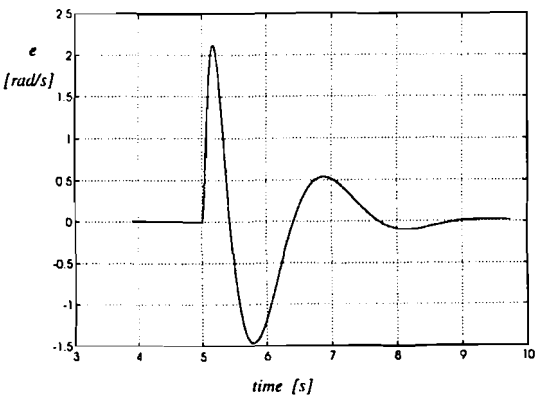

Figure F.10: error between ω_m and ω_{m*}

F.6 Simulation results when $\delta_{\tau_r} = 0$, $\delta_{L_m} = 0$ and T_L has a bandwidth of $1\frac{rad}{s}$

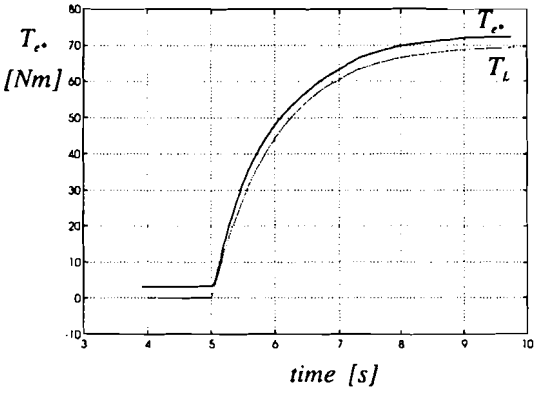

Figure F.11: T_L and T_{e*}

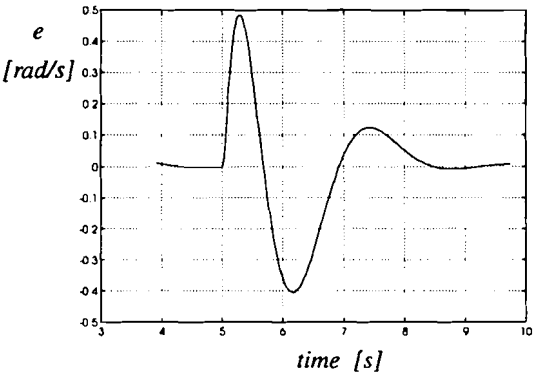

Figure F.12: error between ω_m and ω_{m*}

Appendix G

Current converter simulations

G.1 Input signals

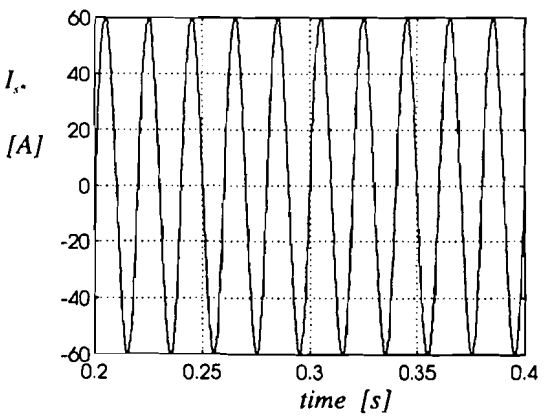

Figure G.1: Stator current I^S_{s*}

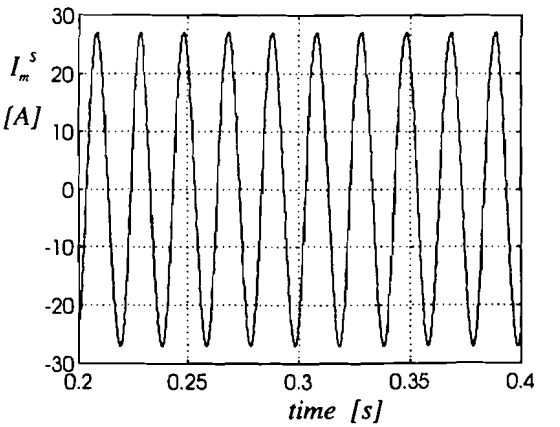

Figure G.2: Magnetizing current I^S_m

G.2 Output signals e and u when $\delta_{R_s} = 0$ and $\delta_{L_\sigma} = 0$

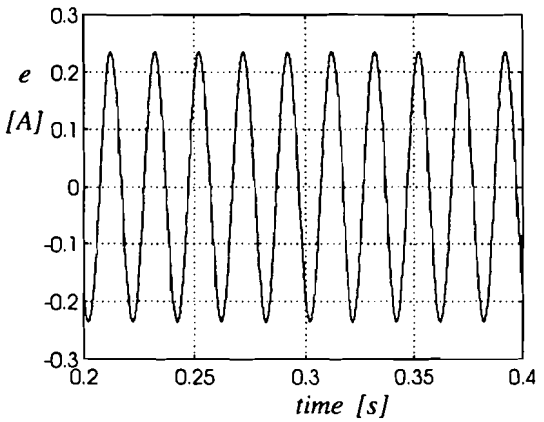

Figure G.3: Error signal e when $\delta_{R_s} = 0$ and $\delta_{L_\sigma} = 0$

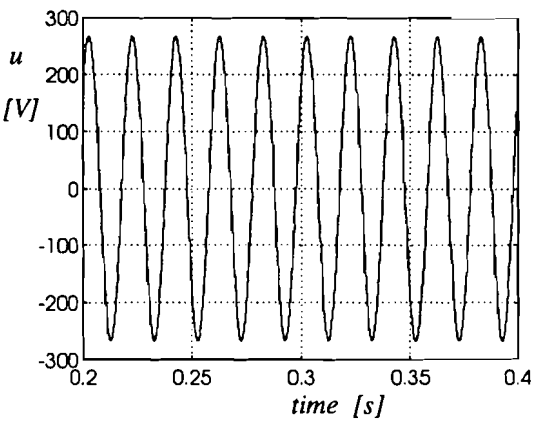

Figure G.4: Converter command signal u when $\delta_{R_s} = 0$ and $\delta_{L_\sigma} = 0$

G.3 Output signals e and u when $\delta_{R_s} = -0.3$ and $\delta_{L_\sigma} = -0.3$

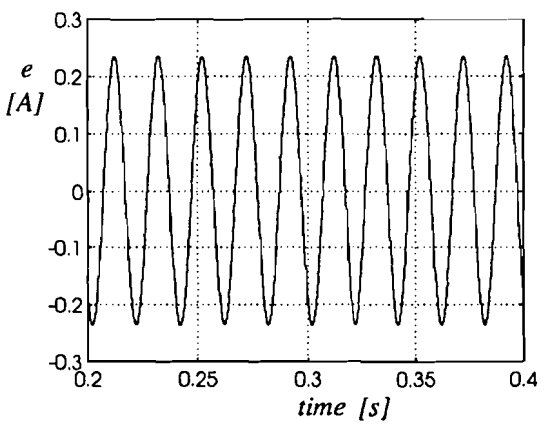

Figure G.5: Error signal e when $\delta_{R_s} = 0.3$ and $\delta_{L_\sigma} = 0.3$

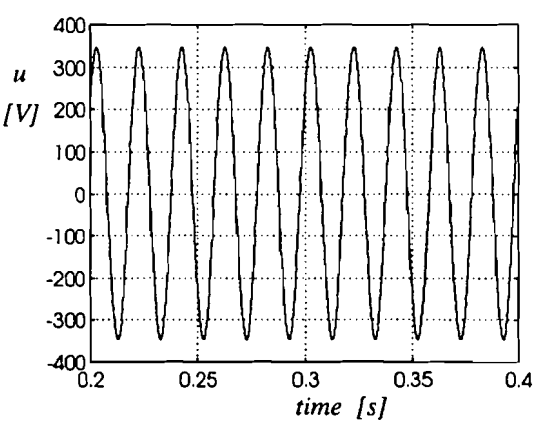

Figure G.6: Converter command signal u when $\delta_{R_s} = 0.3$ and $\delta_{L_\sigma} = 0.3$

Appendix H

List of symbols

α	Constant
β	Constant
C	Transfer function of controller
C_{fb}	Feedback controller
C_{ff}	Feed forward controller
D	Damping coefficient
Δ	Linear error model
$\tilde{\Delta}$	Nonlinear error model
Δ_0	Function with property $\|\Delta_0\|_\infty = 1$
$\tilde{\Delta}_{T_e}$	Nonlinear function that determines δT_e
$\tilde{\Delta}_{I_m}$	Nonlinear function that determines δI_m
ΔI_{ma}	Difference between impressed magnetizing current and the real part of I_m^C
δ_{L_m}	Relative error between L_m and L_m^*
δ_{L_σ}	Relative error between L_σ and L_σ^*
δ_{R_s}	Relative error between R_s and R_s^*
δ_{τ_r}	Relative error between τ_r and τ_r^*
δT_e	Difference between desired torque and actual torque
e	Error signal between actual angular velocity and desired angular velocity
$\hat{e}$	As e, but with property $\|\hat{e}\|_2 < 1$
ϵ	Angle between I_m and I_{m*}
$\Phi_{T_{e*}}$	Power spectrum of T_{e*}
$\Phi_{\delta T_e}$	Power spectrum of δT_e
ϕ^F	Flux expressed in field coordinates
ϕ_m	Mutual flux magnitude
ϕ^R	Flux expressed in rotor coordinates
ϕ_r	Rotor flux magnitude
ϕ_r^R	Rotor flux expressed in rotor coordinates
ϕ_r^S	Rotor flux expressed in stator coordinates
ϕ^S	Flux expressed in stator coordinates
ϕ_s^R	Stator flux expressed in rotor coordinates
ϕ_s^S	Stator flux expressed in stator coordinates

Φ_s	Stator flux magnitude
$\Phi_{s\alpha}$	Real part of stator flux in stator frame
$\Phi_{s\beta}$	Imaginary part of stator flux in stator frame
$\Phi_{\sigma s}$	Flux component which is not linked with the rotor
$\Phi_{\sigma r}$	Flux component which is not linked with the stator
FOC	Field oriented Controller
γ	Scaling factor
G	Process model
H	Noise model
H_m	First order network with time constant τ_r
H_o	First order network with time constant τ_r^*
H_{pi}	Transfer function of a PI controller
$I_{\alpha s}$	Real part of the stator current
$I_{\beta s}$	Imaginary part of the stator current
I_{dm}	Real part of magnetizing current in the field frame
I_{dr}	Real part of rotor current in the field frame
I_{ds}	Real part of stator current in the field frame
I_{ds*}	Desired value of the real part of stator current in the field frame
I^F	Current in field coordinates
IM	Induction Machine
I_m	Magnitude of the magnetizing current
I_{ma}	Real part of I_m expressed in indirect controller frame coordinates
I_{mb}	Imaginary part of I_m expressed in indirect controller frame coordinates
I_m^C	Magnetizing current vector expressed in indirect FOC coordinates
I_m^F	Magnetizing current vector expressed in field coordinates
I_m^M	Magnetizing current vector expressed in machine coordinates
I_m^R	Magnetizing current vector expressed in rotor coordinates
I_m^S	Magnetizing vector expressed in stator coordinates
$I_m^S(s)$	Magnetizing vector expressed in stator coordinates in the s-plane
I_{m*}	Magnitude of the desired magnetizing current
$\hat{I}_{m*}$	As I_{m*}, but with property $\|\hat{e}\|_2 < 1$
I_{m*}^C	Desired magnetizing current vector expressed in indirect FOC coordinates
I_{m*}^F	Desired magnetizing current vector expressed in field coordinates
I_{m*}^R	Desired magnetizing current vector expressed in rotor coordinates
I_{m*}^S	Desired magnetizing vector expressed in stator coordinates
I_{qm}	Imaginary part of magnetizing current in field frame
I_{qr}	Imaginary part of rotor current in field frame
I_{qs}	Imaginary part of stator current in field coordinates
I_{qs*}	Desired imaginary part of stator current in field coordinates
I^R	Current in rotor coordinates
I_r	Magnitude of the rotor current
I_r^F	Rotor current vector expressed in field coordinates
I_r^R	Rotor current vector expressed in rotor coordinates
I_r^S	Rotor current vector expressed in stator coordinates
$IRTF$	Ideal rotating transformer
I_s	Magnitude of the stator current
I_{s*}	Desired stator current

$\hat{I_{s*}}$	As I_{s*}, but with property $\|\hat{I_{s*}}\|_2 < 1$
$I_{s\alpha}$	Real part of stator current in stator frame
$I_{s\beta}$	Imaginary part of stator current in stator frame
I_s^C	Stator current vector expressed in indirect FOC coordinates
I_s^F	Stator current vector expressed in field coordinates
I_s^M	Stator current vector expressed in machine coordinates
I_s^R	Stator current vector expressed in rotor coordinates
I_s^S	Stator current vector expressed in stator coordinates
$I_s^S(s)$	Stator current vector expressed in stator coordinates in s-plane
J	Inertia
K	Controller
k_1	Transformation parameter
k_p	Parameter that determines the proportional part of the PI controller
L_{mag}	Mutual inductance
L_m	Magnetizing inductance in the IM
L_m^*	Magnetizing inductance in the indirect FOC
L_σ	Leakage inductance
M	generalized system
ω_f	Angular velocity of rotor flux
ω_m	Angular velocity of the rotor axis
ω_{m*}	Angular velocity of the rotor axis
$\hat{\omega}_{m*}$	As ω_{m*} but with property $\|\hat{\omega}_{m*}\|_2 < 1$
ω_{slip}	Slip angular velocity
$\omega_{slip,max}$	Maximimum slip angular velocity
ω_{slip*}	Desired slip angular velocity
ω_0	Angular velocity of the stator current
$\tilde{P}_{T_e}$	Nonlinear function that determines the torque
$\tilde{P}_{I_m}$	Nonlinear function that determines the magnetizing current
P_G	Uncertainty description of transfer function G
R_{r0}	Rotor resistance
R_r	Rotor resistance in the IM
R_r^*	Rotor resistance in the indirect FOC
R_{s0}	Stator resistance
R_s	Stator resistance
ρ	Angle between flux and stator frame
ρ_*	Desired angle between flux and stator frame
S	Sensitivity
$slip$	slip
T_e	Actual electromagnetic torque
$T_{e,max}$	Maximal flux that can be generated
T_{e*}	Desired electromagnetic torque
$\hat{T}_{e*}$	As T_{e*}, but with property $\|\hat{T}_{e*}\|_2 < 1$
Θ	Parameter set in the induction machine
Θ^*	Parameter set in the FOC
θ_m	Angle between rotor axis and stator frame
θ_{slip}	Angle between flux vector and rotor axis angle
θ_{slip*}	Desired angle between flux vector and rotor axis angle

τ_i	Parameter of the PI-controller.
τ_r	Rotor time constant in the induction machine
τ_r^*	Rotor time constant in the indirect FOC
T_L	Load torque
$\hat{T}_L$	As T_L, but with property $\|\hat{T}_L\|_2 < 1$
u_Δ	Input signal of uncertainty model
$\hat{u}_\Delta$	As u_Δ, but with property $\|\hat{u}_\Delta\|_2 < 1$
u_k	Output signal of controller
U^R	Voltage expressed in rotor coordinates
U_r^R	Rotor voltage expressed in rotor coordinates
U^S	Voltage expressed in stator coordinates
u	Magnitude of the stator voltage
$\hat{u}$	As u, but with property $\|\hat{u}\|_2 < 1$
U_s	Stator voltage magnitude
$U_{s\alpha}$	Real part of stator voltage
$U_{s\beta}$	Imaginary part of stator voltage
U_s^S	Stator voltage expressed in stator coordinates
V_δ	Shaping filter of u_Δ
V_L	Shaping filter of input T_L
V_ω	Shaping Filter of input ω_{m*}
W_a	Weighting filter of T_{e*}
W_Δ	Uncertainty filter
W_e	Weighting filter of e
W_G	Uncertainty filter
W_u	Weighting filter of stator voltage
w	Exogenous input vector
ξ	Angle between stator current vector and stator frame
ξ_*	Desired angle between stator current vector and stator frame
ξ_f	Torque angle
ξ_{f*}	Desired torque angle
y_Δ	Output signal of uncertainty model
y_k	Measured output signals
z	Output vector with variables that are to be controlled

Bibliography

[1] Bose, B.K.
POWER ELECTRONICS AND AC DRIVES
Englewood Cliffs, New Jersey: Prentice-Hall 1986

[2] Chouitter, Clerc, G., Retif, J.M., Auriol, Ph.
H_∞ CONRTOLLERS DESIGN FOR FIELD ORIENTED ASYNCHRONOUS MACHINE
In: Proceedings of the European Power Electronics Symposium, Vol. 1, 1994, p. 161-166

[3] Doyle, J.C., Francis, A.F., Tannenbaum, A.R.
FEEDBACK CONTROL THEORY
New York: MacMillan Publishing company 1992

[4] Falkus, H.
USER MANUAL MULTIVARIABLE H_∞ CONTROL DESIGN TOOLBOX
Measurement and Control Group, Department of Electrical Engineering, Eindhoven University of Technology, 1992

[5] Fodor, D., Diana, D., Griva, G., Profumo, F.
IFO CONTROL PERFORMANCE CONSIDERING PARAMETER DETUNING AND ROTOR SPEED ERROR
In: Proceedings from Conf. Rec. IAS '94, Denver, USA, 1994, p.719-725.

[6] Gorter, R.J.A.
A PARAMETER ESTIMATOR FOR INDUCTION MACHINES
Eindhoven: Instituut Vervolgopleidingen, Eindhoven University of Technology, 1994.

[7] Leonhard, W.
CONTROL OF ELECTRONIC DRIVES. 3rd ed.
Berlin, Heidelberg, New York, Tokyo: Springer-Verlag 1990

[8] Maciejowski, J.M.
MULTIVARIABLE FEEDBACK DESIGN
Cambridge: Addison-Wesley Publishing Company 1990

[9] Schilperoort S.M.
MODELLING AND IDENTIFICATION OF SINGLE AND DOUBLE-CAGE INDUCTION MACHINES
Eindhoven, section EMV, Faculty of electrical engineering, Eindhoven University of Technology, 1994

[10] Steinbuch, M., Terlouw, J.C., Bosgra, O.H.
ROBUSTNESS ANALYSIS FOR REAL AND COMPLEX PERTURBATIONS APPLIED TO AN ELECTRO-MECHANICAL SYSTEM
In: Proceedings from the American Control Conference, Vol. 1, 1991, p. 556-561

[11] Thomas, J.L.
μ-ANALYSIS APPLIED TO FIELD ORIENTED CONTROL OF INDUCTION MOTOR
In: Proceedings from The European Power Electronics Association, vol I, Vol. 1, p. 73-78, 1993.

[12] Vas, P.
VECTOR CONTROL OF AC MACHINES
Oxford: Clarendon Press 1990.

[13] Veltman, A.
THE FISH METHOD
Delft: Delft University of Technology, 1994.
Doctoral dissertation

[14] Yau-Tze Kao, Tian-Hua Liu and Chang-Huan Liu
DESIGN OF H_2 and H_∞ CONTROLLERS FOR INDUCTION MOTOR DRIVES
In: Proceedings of the 29th Conference on Decision and Control, Honolulu, Hawaii, vol. 6, 1990, p. 3345-3346